FABRICATION OF TYPE-I INDIUM-BASED NEAR-INFRARED EMITTING QUANTUM DOTS FOR BIOLOGICAL IMAGING APPLICATIONS

Dissertation submitted to the Faculty of Natural Sciences, University of the Western Cape in fulfillment of the requirements for the degree of

DOCTOR OF PHILOSOPHY

IN

CHEMISTRY

By

PAUL MUSHONGA
BSc (Hons) Chemistry (University of Zimbabwe)
MSc Chemistry (University of Cape Town)

DECLARATION

"I declare that this thesis, **'FABRICATION OF TYPE I INDIUM-BASED NEAR-INFRARED EMITTING QUANTUM DOTS FOR BIOLOGICAL IMAGING APPLICATIONS'**, is my own work and has not been presented before for any degree or examination in any other university, and that all the information sources I have used and or quoted have been indicated and acknowledged by means of complete references."

PAUL MUSHONGA

Signature **Date**

ABSTRACT

Fabrication of type I indium-based near-infrared emitting quantum dots for biological imaging applications

P. Mushonga

PhD Thesis, Department of Chemistry, University of the Western Cape

Semiconductor nanocrystals or quantum dots (QDs) are fluorescent nanometer-sized particles which have physical dimensions that are smaller than the excitonic Bohr radius, large surface area-to-volume ratios, broad absorption spectra and very large molar extinction coefficients. Biomedical applications of QDs are mainly based on II-VI QDs containing cadmium, such as CdSe/ZnS. These cadmium-based systems are associated with high toxicity due to cadmium. As a result, potential replacements of cadmium-based QDs in biological applications are needed. In this study, InP/ZnSe QDs were synthesized for the first time using a one-pot hot injection method. Furthermore, a growth-doping method was used for silver, cobalt and iron incorporation into the InP core. Water compatibility was achieved through ligand exchange with 3-mercaptopropionic acid. *In vitro* cytotoxicity and imaging/internalization of the as-prepared MPA-InP/ZnSe and MPA-capped CdTe/ZnS QDs were evaluated. InP/ZnSe QDs were successfully synthesized with ZnSe shell causing a 1.4 times reduction in trap-related emission. Lattice fringes and SAED pattern confirmed the good crystallinity and zinc blende structure of the QDs. Secondary injection of precursors and starting with large moles of the precursors resulted in red shift in emission peak. However, a blue shift was observed with increase in initial zinc concentration. A photoluminescence red shift was observed with increasing silver dopant ions, while iron doping caused a blue shift. However, no change in emission peak position was

observed with increase in cobalt dopant levels. All the three dopants caused quenching of photoluminescence attributed to reduced electron-hole recombination. XRD data showed that the crystal structure was not altered by the doping process. A concentration of 125 µg/mL InP/ZnSe QDs, less than 50 % of cell death had occurred while more than 80 % of cell death had occurred for an even lower concentration (62.5 µg/mL) of CdTe/ZnS QDs suggesting, that the indium-based QDs were less toxic than the cadmium-based QDs. Fluorescence imaging of Caco-2 cells treated with TAT-InP/ZnSe bioconjugates showed high fluorescence compared to the unconjugated QDs indicating that the as-prepared QDs retained their fluorescence properties in the biological milieu. In conclusion, less toxic near-infrared InP/ZnSe and transition metal-doped InP/ZnSe QDs were successfully synthesized.

DEDICATION

This work is dedicated to my love Shuvai

and my two lovely daughters Charity and Epiphaniah.

The God and Father of our Lord Jesus Christ,

who hath blessed us with all spiritual blessings in heavenly places,

richly bless you.

ACKNOWLEDGEMENTS

I would like to thank the LORD God for directing my footsteps. He is in total control of all things.

My sincere gratitude and appreciation are extended to Drs Martin Onani and Abram Madiehe for respectively supervising and co-supervising my PhD work with patience, professionalism and steadfastness. I am also very grateful to Dr Mervin Meyer for his valued contributions throughout this work.

I wish to thank Prof Emmanuel Iwuoha and the SensorLab for unlimited access to the Nanolog instrument, Prof Basil Julies and the EMU staff for help with HRTEM as well as training on the instrument and Dr Remy Bucher of iThemba Labs for help with XRD analyses.

I am very grateful to Ntevheleni Thovhogi and Nicole Sibuyi for their cherished assistance in the biology intricacies. Many thanks go to members of the Organometallic Research Group, Diabetes Research Group, Apoptosis Research Group and the NIC Biolabels Unit for their support.

Special thanks go to Messrs. Andile Mantyi, Ben du Wet, Timothy Lesch and Bongani Makhoba for taking care of the technical aspects of research in the Department of Chemistry.

I would also like to thank DST/Mintek for financial support and the Chemistry Department, UWC for the enabling environment.

My wife Shuvai and my two beautiful daughters Charity and Epiphaniah, your love and support are greatly cherished. Many thanks also go to my parents, my young brother Brighton and his family for their support and encouragement.

CONFERENCE CONTRIBUTIONS AND PUBLICATIONS

Conference contributions

1. **Paul Mushonga**, Martin O. Onani, Abram M. Madiehe, Mervin Meyer, 2009. *Fabrication of Type I Indium-based Near-infrared Emitting QDs for Biological Imaging.* DST/MINTEK Annual NIC 'Nanotechnology for Development' Workshop. University of Johannesburg, Johannesburg, South Africa. **Oral Presentation**

2. **Paul Mushonga**, Martin O. Onani, Abram M. Madiehe, Mervin Meyer, 2010. *Fabrication of Type I Indium-based Near-infrared Emitting QDs for Biological Imaging.* DST/MINTEK Annual NIC 'Nanotechnology for Development' Workshop. University of the Western Cape, Cape Town, South Africa. **Oral Presentation**

3. **Paul Mushonga**, Martin O. Onani, Abram M. Madiehe, Mervin Meyer, 2011. *Luminescent Indium Phosphide-based Semiconductor Nanocrystals: Synthesis, Characterization and Biofuntionalization.* DST/MINTEK Annual NIC 'Nanotechnology for Development' Workshop. MINTEK Johannesburg, South Africa. **Oral Presentation**

4. **Paul Mushonga**, Martin O. Onani, Abram M. Madiehe, Mervin Meyer, 2011. *Luminescent Indium Phosphide-based Semiconductor Nanocrystals: Synthesis, Characterization and Biofuntionalization.* The 6th International Conference of the Africa Materials Research Society, Victoria Falls, Zimbabwe. **Oral Presentation**

5. Martin O. Onani, **Paul Mushonga**, Abram M. Madiehe, Mervin Meyer. *Synthesis, Characterization, Surface Modification and Biological application of luminescent InP/ZnSe Semiconductor Nanocrystals.* The 6th International Conference of the Africa Materials Research Society, Victoria Falls, Zimbabwe. **Poster Presentation**

6. **Paul Mushonga**, Martin O. Onani, Abram M. Madiehe, Mervin Meyer, 2012. *Highly luminescent Doped-Indium Phosphide-based Semiconductor Nanocrystals: Synthesis, Characterization and Functionalization.* 4th International Conference on nanoscience and Nanotechnology (NanoAfrica2012), University of the Free State, Bloemfontein, South Africa. **Poster Presentation**

Publications

1. Martin O. Onani, Paul Mushonga, Lehlohonolo F. Koao, Francis B. Dejene, "Luminescence properties of Eu, Mg co-doped sol–gel SiO_2 glasses", *ISRN Nanotechnology,* 2012, *2012, 298694*

2. Paul Mushonga, Martin O. Onani, Abram M. Madiehe, Mervin Meyer, "Indium Phosphide-Based Semiconductor Nanocrystals and Their Applications", *J. Nanomaterials,* 2012, *2012, 869284*

3. Paul Mushonga, Martin O. Onani, Abram M. Madiehe, Mervin Meyer, "One-pot synthesis and characterization of InP/ZnSe nanocrystals" *Mater. Lett., 2013,95, 37*

TABLE OF CONTENTS

LIST OF ABBREVIATIONS AND SYMBOLS

Ab	Antibody
°C	Degrees Celsius
DHLA	dihydrolipoic acid
d-dot	Doped quantum dot
DMEM	Dulbecco's Modified Eagle's Medium
EDC	1-ethyl-3-(3-dimethylaminopropyl)carbodiimide hydrochloride
EDX	Energy-dispersive X-ray spectroscopy
EPR	Enhanced permeability and retention
eV	Electron volt
FWHM	full width at half maximum
g	Gram
h	Hour
HRTEM	High resolution transmission electron microscopy
kDa	Kilodalton
L	Litre
µ	micro
min	Minute
mol	Moles
mmol	Millimoles
MPA	3-mercaptopropionic acid
MWCO	molecular weight cut-off
ODE	1-octadecene
NC	Nanocrystal
nm	Nanometer

PA	Palmitic acid
PBS	Phosphate buffered saline
PEG	Polyethylene glycol
PL	Photoluminescence
QD	quantum dot
QY	quantum yield
rpm	revolutions per minute
SAED	selected area electron diffraction
STEM-EELS	Scanning transmission electron microscopy – Electron energy loss spectroscopy
STEM-EDS	Scanning transmission electron microscopy - Energy-dispersive X-ray spectroscopy
× g	times gravity
TAT	Trans-activator of transcription
TEM	Transmission electron microscopy
TOP	Trioctylphosphine
TOPO	Trioctylphosphine oxide
UV	Ultraviolet
XAS	X-ray absorption spectroscopy
XRD	X-ray diffraction

LIST OF TABLES

LIST OF FIGURES

LIST OF SCHEMES

CHAPTER 1: INTRODUCTION

1.1 Introduction

Inorganic nanomaterials are substance that are engineered at the nanometer level and act as a bridge between bulk and molecular systems [1,2]. These nanomaterials fall into three classes – 2D (e.g. thin films or quantum wells), 1D (quantum wires) and 0D (quantum dots) [3]. Quantum dots (QDs) or semiconductor nanocrystals have physical dimensions that are smaller than the excitonic Bohr radius (distance between electron and hole) and this leads to the quantum confinement effect (QCE) [4,5]. The QCE arises from the spatial confinement of the charge carriers and culminates in the widening of the band gap with a decrease in QD size [6]. The excitonic energy is given by equation (Eq. 1.1) adapted from literature [7],

$$E(R) = E_{bulk}(InP) + \frac{2h^2}{\mu}(\frac{\pi}{R_{nc}})^2 \qquad \text{(Eq. 1.1)}$$

where μ is the effective mass of an electron-hole pair given by $\frac{1}{\mu} = \frac{1}{m_e} + \frac{1}{m_h}$; R_{nc} is the nanocrystallite size and h is the Planck's constant.

This QCE is responsible for the size, shape and composition tunable optical and electronic properties that are not available from either the bulk solids or discrete atoms.

The properties of QDs that are of interest include broad absorption spectra that increase towards the UV from the first absorption band edge [8,9]. QDs also have very large molar extinction

coefficients in the order of 0.5-5 x 10^6 M^{-1} cm^{-1}, about 10-50 times larger than those of organic fluorophores [8]. This makes them brighter probes suitable for *in vivo* studies where light intensities are severely attenuated by absorption and scattering. QDs have longer excited state lifetimes and hence large effective Stokes shifts. This enables the separation of QD fluorescence from background fluorescence. A large surface area-to-volume ratio in QDs allows them to be conjugated to various molecules. QDs are highly photostable, a property that enables visualization of biological material for a longer time. Narrow and symmetrical emission spectra allow various colors to be distinguished without any spectral overlap.

This Chapter will focus on quantum dots – their structure, synthesis methods and some biological applications.

1.2 The core structure of QDs

QDs are nanometer-sized clusters that are synthesized from a variety of semiconductor materials [10]. They are generally composed of a few hundreds to several thousands of atoms [11-13] from Groups II-VI, III-V and IV-VI. These elements constitute the inner core of the binary QDs.

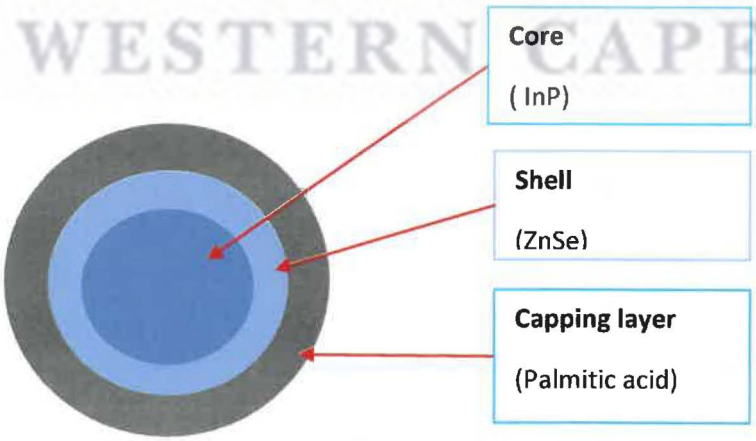

Figure 1.1 Structure of a semiconductor quantum dot

In binary QDs, the band gap energy is tuned by varying the size of the nanocrystals. There are two other types of QD cores which are alloyed and doped cores. Alloyed QDs are synthesized by creating a solid solution of two binary semiconductors. The alloyed QDs can be classified as ternary or quartenary alloys. In ternary QDs, the precursor binary systems share a common cation or anion, e.g. $InAs_xP_{1-x}$ formed from InP and InAs systems. Quartenary QDs are formed when the two binary systems have no common element. They have a general formula $A_xB_{1-x}C_yD_{1-y}$ with A and B cations and C and D anions e.g. $Zn_xCd_{1-x}S_ySe_{1-y}$ [14]. Alloyed QDs allow for the engineering of the band gap energy by varying the composition of the constituents in addition to controlling the size. Doped QDs are formed when impurities or dopants are intentionally added to the semiconductor nanocrystals with the aim of improving their optoelectronic properties [15]. Examples of dopants that have been used include Cu [16-18], Mn [18,19] and Ag [20]. A dopant provides carriers (electrons or holes), hence improving the optical properties of the QDs. When used in biomedical imaging applications, fluorescent dopants may palliate toxicity concerns by allowing the fabrication of infrared emitting QDs from less toxic elements [21].

1.3 The surface structure of QDs

Quantum dots have very high surface area-to-volume ratio and therefore their surface properties have significant effects on both the electronic and optical properties [22]. With a large number of atoms located near the surface, surface states become more important in influencing the optical and photoluminescence properties of these nanocrystals. These surface states are a result of unsatisfied (dangling) bonds that are found at the reconstructed surface. Cationic dangling bonds

give rise to electron traps (donors) near the conduction band edge, while anionic dangling bonds form hole traps (acceptors) in the middle of the band gap [23].

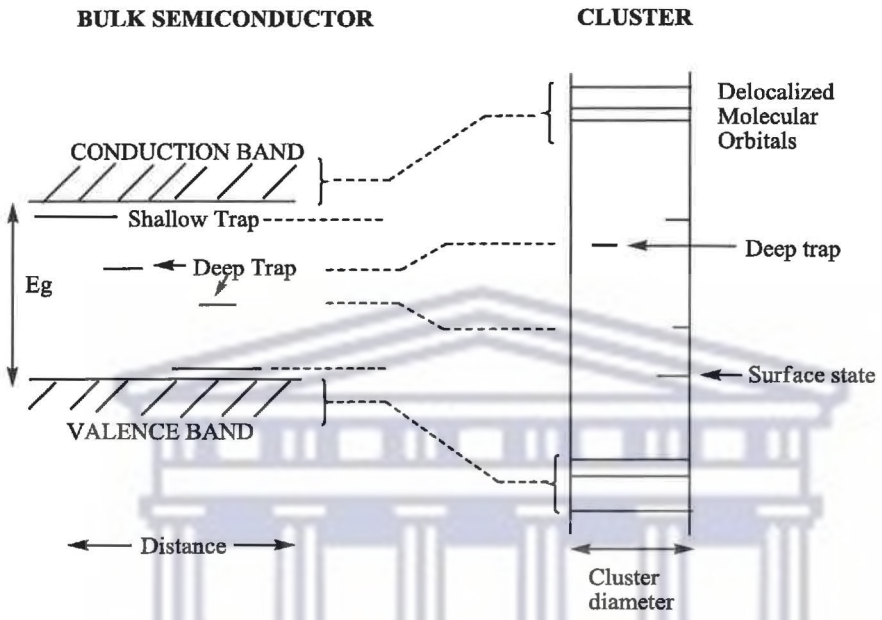

Figure 1.2 Schematic diagram relating cluster states to bulk crystal states (reprinted with permission from [24], Copyright 1986, American Chemical Society)

The surface states have great influence on the exciton relaxation dynamics. They act as sites for non-radiative decay of the QD excited state [25]. Some of the electrons excited to the conduction band transfer to these surface states lying in the mid band gap, and then recombine nonradiatively with the holes in the valence band, reducing the photoluminescence quantum yield.

1.3.1 Organic surface passivants

During quantum dot synthesis, surfactant molecules are added to the reaction medium. These molecules bind to the QD surface preventing aggregation of the particles [26]. Examples of surfactant molecules used include phosphines (trioctylphosphine oxide (TOPO) and

trioctylphosphine (TOP)) [27], oleic acid [28], or tetradecylphosphonic acid (TDPA) [29]. The surfactant layer also has the ability to control the size and shape of the growing QDs. The surfactant molecules should be labile enough to allow for the addition of monomer units as well as strong enough to prevent nanocrystal aggregation [30]. The layer provides imperfect passivation of the nanocrystal surface dangling orbitals [31] due to the lability of the organic ligands [32]. Alivisatos' group reported that it is very difficult to simultaneously passivate both the cationic and anionic surface dangling bonds using organic ligands resulting in some dangling bonds always remaining [33]. In 2012, Lee *et al.* [34] reported detailed experimental (X-ray absorption spectroscopy) and theoretical (*ab initio* calculations) studies on the effects of surface passivation on the electronic structure of CdSe as model QDs. Using TOPO-capped and hexadecylamine (containing coordinating nitrile impurities represented by CN) (HDA/CN)-capped CdSe, they showed that differences in the appearance of their XAS spectra were primarily due to the ligand effects. In order to rule out the effects of different synthetic conditions, the ligands for CdSe-TOPO and CdSe-HDA/CN were exchanged for the alternative surfactant. Further analysis revealed that replacing ligands on the CdSe-HDA/CN system with TOPO culminated in its XAS spectrum adopting the characteristic form for the as-prepared CdSe-TOPO and vice versa. These researchers demonstrated that the electronic properties of CdSe were dependent upon the type of the passivating molecules as well as the nature of ligand-surface interactions. The different chemical methods of synthesizing the QDs of the same size did not affect the electronic structure. Theoretically, the spectral variations observed were attributed to variations in the unoccupied density of states (DOS) as a result of distinct geometries. The researchers reported that surface atoms show a decrease in spectrally active

DOS in the region beyond the absorption edge and its level of partial restoration on passivation is ligand dependent.

1.3.2 Inorganic shell

Overcoating the nanocrystal core with an inorganic shell of a semiconductor effectively passivates surface-related defects resulting in improved fluorescence quantum yield as well as enhanced photostability [35,36]. The enhanced stability with respect to photooxidation is due to the fact that the holes are no longer at the nanoparticle surface [33]. Gong *et al.* [25] reported that the emission efficiency of the core/shell CdSe/ZnS was 3.9 times higher than that of the bare CdSe QDs, demonstrating that surface traps are effectively depressed after epitaxially depositing the larger band gap semiconductor ZnS onto the CdSe nanocrystal core. The size of the CdSe core in CdSe/ZnS core/shell QDs was controlled to be the same with the bare CdSe (average size of 2.98 nm). There are three types of core/shell systems based on band alignments which are type I, type II and reverse type I [37] (**Figure 1.3**). In type I core/shell QDs such as InP/ZnSe, the band gap of the shell material is larger than that of the core. The conduction and valence bands of the shell are respectively higher and lower than those of the core leading to confinement of charge carriers in the core material. In type II systems such as CdTe/CdSe, both the conduction and valence bands of the core are lower (or higher) in energy than the shell leading to separation of charge carriers between the core and the shell. In reverse type I heterostructures, the band gap of the shell material is smaller than that of the core. The charge carriers are, depending on the thickness of the shell, partially or completely delocalized in this type of core/shell systems.

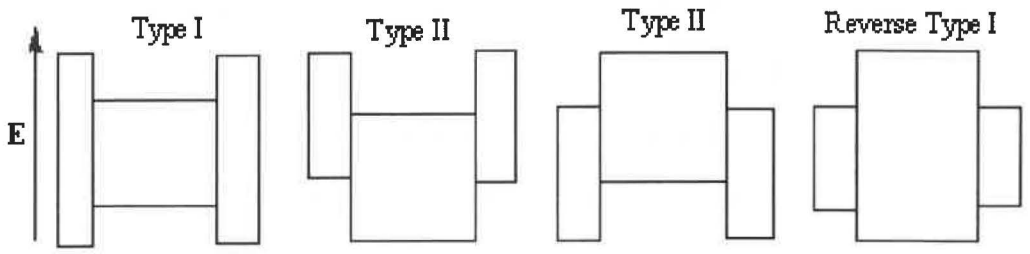

Figure 1.3 Schematic representation of the energy-level alignment in different core/shell systems. The upper and lower edges of the rectangles correspond to the positions of the conduction and valence band edges of the core (centre) and shell materials respectively (reprinted with permission from[38], Copyright 2009, Wiley-VCH Verlag GmbH & Co. KGaA).

Cao and Banin [31] reported that the inorganic shell type as well as shell thickness were critical in the tailoring of the optical and electronic properties of the QDs. Lattice mismatch parameter is also critical in the design of core/shell QD systems as it influences epitaxial deposition of the shell layer onto the core. The lattice mismatch parameters of some selected core/shell QDs are listed in **Table 1.1**.

Table 1.1 Lattice mismatch parameters for selected core/shell combinations

Core/shell system	Lattice mismatch (%)	Ref
CdSe/ZnSe	7	[9]
CdSe/CdS	3.9	[33]
CdSe/ZnS	12	[39]
CdS/ZnS	7	[40]
ZnSe/ZnS	4,6	[41]
InP/ZnSe	3.5	[42]
InP/ZnS	7.6	[43]

1.4 General synthetic techniques

The general synthesis of high-quality QDs is of utmost importance as all their properties are dependent on particle quality which is controlled by size distribution and crystal defects. There are generally two techniques, namely, the hot-injection and heating-up techniques which have evolved in the last two decades. These techniques have been established for the synthesis of the majority of the reported QDs [44].

1.4.1 Hot-injection technique

This technique involves the rapid injection of a room temperature solution of precursors into an extremely hot reaction medium in the presence of carefully chosen surfactant molecules. The rapid injection of the precursor solution induces the sudden supersaturation of the solution resulting in a short burst of nucleation. The injected solution reduces the reaction temperature and dilutes the concentration of reactants. With the reaction temperature dropping in response to addition of the cold precursor solution, coupled with the low concentration of the remaining precursor molecules, further nucleation is prevented. The eventual growth of the nanocrystals follows at a lower temperature than that of the nucleation process. This sequential separation of the nucleation and growth processes generally leads to a precise control of the size and shape of the semiconductor nanocrystals. This latter process forms the strength of this technique. A pioneering example of this technique was reported by Murray *et al.* [45]. These researchers injected cadmium and selenium precursors into a hot (300 °C) solution of tri-n-octylphosphine oxide (TOPO). The growth temperature used was 230-260 °C. Here the surfactant acts in

fourfold; firstly, it is as a coordinating solvent that controls the growth process while at the same time stabilizing the nanocrystal core. Secondly, the surfactant binds to the surface of the nanocrystals providing a barrier to the addition of more material to the surface of the nanocrystals slowing down the growth kinetics [46]. Thirdly, it serves to prevent the aggregation of particles and finally passivates the surface of the nanocrystals.

1.4.2 Heating-up technique

This is a batch process where all precursors are mixed at room temperature followed by a rapid heating of the system to the appropriate growth temperature for the nanocrystals. There is no operation under this method that induces high supersaturation as in the hot-injection method. Under this technique, the supersaturation level and the temperature of the solution increase together, and the nucleation rate is sensitive to both [47]. The procedure allows for scaling up as well as improving reproducibility [48]. An example of the application of the heating-up method was reported by Li *et al.* [49]. The authors mixed copper(I) iodide, indium(III) acetate and 1-dodecanethiol in 1-octadecene at room temperature and then rapidly raised the temperature to 230 °C for the growth of $CuInS_2$ cores. Addition of the ZnS shell yielded highly luminescent core/shell nanocrystals with PL in the range 550 – 815 nm with a maximum quantum yield of 60 %.

1.5 Processes involved in QD synthesis

The synthesis of QDs via the colloidal routes involves two processes; nucleation and growth processes. Control of these processes may enable the fabrication of nanostructures with determined morphologies and sizes [50]. Manna *et al.* [51] reported that the manipulation of parameters such as ratio of surfactants, injection volume and monomer concentration in the synthesis of CdSe QDs yields nanocrystals that have rod, arrow teardrop and tetrapod morphologies.

1.5.1 Nucleation step

In this step, the precursors react at very high temperatures to form a supersaturation of monomers. A burst of nucleation takes place with the formation of a large number of nuclei in a short space of time. The nuclei then grow rapidly by incorporating additional monomers still present in the reaction system [52]. This lowers the concentration of monomer or solute molecules below the nucleation level. Slow growth by diffusion then follows. An energy barrier which exists in the homogenous nucleation step is explained thermodynamically in a review by Park *et al.* [53] as follows: the Gibbs free energy of the formation of spherical crystals with a radius r from a solution with supersaturation S is given by

$$\Delta G = 4\pi r^2 \gamma + \frac{4}{3}\pi r^3 \Delta G_v \qquad \text{(Equ. 1.2)}$$

where γ is the surface free energy per unit area and ΔG_v is the free energy change between the monomers on solution and unit volume of bulk crystal given by the expression

$$\Delta G_v = \frac{(-RTInS)}{Vm} \qquad \text{(Equ. 1.3)}$$

where Vm is the molar volume of the bulk crystal. The term ΔG_v has a negative value as long as the solution is supersaturated.

The value of r at which ΔG is maximum is referred to as the critical radius r_c, which represents the minimum radius of a nucleus that can grow spontaneously in the supersaturated solution. When $d\Delta G/dr) = 0$, then r_c can be determined as:

$$r_c = \frac{2\gamma V_m}{RTInS_c} \qquad \text{(Equ. 1.4)}$$

where S_c is the critical supersaturation.

As r_c is the minimum radius that will persist and not dissolve in solution, S_c should be sufficiently high for r_c to be smaller than the size of crystallites that form nuclei for the homogeneous nucleation step. The sizes of the crystallites are estimated to be less than 1 nm. The substitution of Equ. 1.4 in to Equ. 1.2 gives the critical free energy ΔG_c (which is necessary to form a stable nucleus) as

$$\Delta G_c = \frac{16\pi\gamma^3}{3(\Delta G_v)^2} = \frac{16\pi\gamma^3 V_m^2}{3(RTInS_c)^2} \qquad \text{(Equ. 1.5)}$$

If the rate of increase in the number of particles N is defined as the rate of nucleation, it can be written in the Arrhenius form in terms of ΔG_c as follows [53]:

$$\frac{dN}{dt} = A\exp\left[-\frac{\Delta G_c}{kT}\right] = A\exp\left[\frac{16\pi\gamma^3 V_m^2}{3k^3T^3N_A^2\left(InS_c\right)^2}\right] \qquad \text{(Equ. 1.6)}$$

It should be noted that, in contrast to the simple LaMer model, it is difficult to define the critical supersaturation level S_c at which nucleation starts as there is nucleation and redissolution as a result of energy fluctuations in the solution. However, it is reasonable to establish the level of S_c at which the rate of nucleation is higher than the rate of dissolution and the nuclei start to accumulate. Equ. 1.6 is then expressed in terms of S_c as:

$$InS_c = \left[\frac{16\pi\gamma^3 V_m^2}{3k^3T^3N_A^2\left(A/\left(dN/dt\right)\right)}\right]^{\frac{1}{2}} \qquad \text{(Equ. 1.7)}$$

At this S_c value, the rate of nucleation is so high that the effective number of nuclei increases even while smaller nuclei redissolve. It is important to note that the thermodynamic model assumes that γ and ΔG_c are constant. However, for nanometer-sized particles, the two parameters are strongly size-dependent. **Figure 1.4** shows a schematic representation of LaMer's nucleation concept.

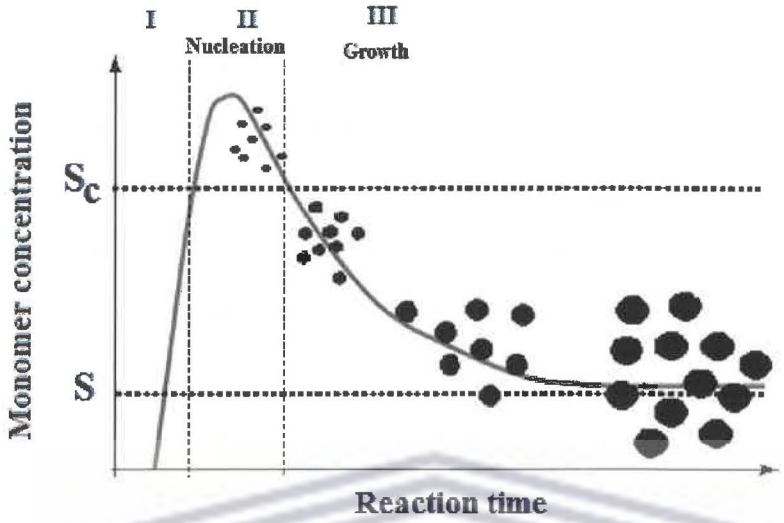

Figure 1.4 Schematic representation of LaMer's nucleation concept. S and S_c represent supersaturation and critical supersaturation respectively [54].

1.5.2 Growth step

This phase comes immediately after the nucleation step has stopped. The nuclei grow larger by the deposition of monomers from a supersaturated solution. Su *et al.* [55] reported a model describing the growth behavior for a particle of radius *r* as depicted in **Figure 1.5**.

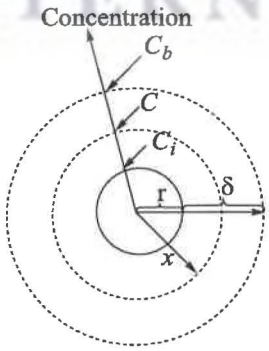

Figure 1.5 Schematic diagram of the diffusion model of spherical particle growth [55]

In their model, for a diffusion layer of thickness δ, the total flux of solute representing the crystallizing material *J,* passing through a spherical surface of radius *x*, is derived by Fick's law as

$$J = 4\pi x^2 D\frac{dC}{dx}, \qquad \text{(Eq. 1.8)}$$

where *D* is the diffusion coefficient and *C* is the solute concentration at *x* ($r \le x \le \delta$). For steady-state growth conditions, the integration of *C*(*x*) from $r+\delta$ to r yields

$$J = \frac{4\pi Dr(r+\delta)}{\delta}(C_b - C_i) \qquad \text{(Eq. 1.9)}$$

where C_b and C_i are the bulk solute concentration and the solute concentration at the interface respectively. Given that the surface reaction is first-order, under the reasonable assumption of high supersaturation, the total flux of solute *J,* is then expressed as

$$J = 4\pi r^2 k(C_i - C_{eq}) \qquad \text{(Eq. 1.10)}$$

where *k* is the rate constant and C_{eq} is the equilibrium concentration of the particle of radius *r*. As *J,* from the mass balance is related to *dr/dt* as

$$J = \frac{4\pi r}{V_m}\frac{dr}{dt} \qquad \text{(Eq. 1.11)}$$

where V_m is the molar concentration of the solid, combining the three equations then gives

$$\frac{dr}{dt} = \frac{DkV_m(r+\delta)}{D(r+\delta)+k\delta r}(C_b - C_{eq}) \qquad \text{(Eq. 1.12)}$$

And for nanoparticles, $r << \delta$, reducing the above equation to

$$\frac{dr}{dt} = \frac{DkV_m}{D+kr}(C_b - Ceq) \qquad \text{(Eq. 1.13)}$$

Further growth of the particles has been explained using the coarsening effect (also called the Ostwald ripening effect), a process that involves the growth of larger particles at the expense of smaller ones [56]. Lee *et al.* [50] reported that the Ostwald ripening effect is independent of the crystal growth that occurs immediately after the nucleation of nanoparticles. The Ostwald ripening model is based on the Thompson-Freundlich equation

$$C_r = C_\infty \exp\left[\frac{2\gamma V_m}{RT}\frac{1}{r}\right] \qquad \text{(Eq. 1.14)}$$

where C_r is the equilibrium concentration for particle with radius r, C_∞ is the equilibrium concentration for a flat surface, γ is the interfacial energy, V_m is the molar volume of the solid phase, R is the universal gas constant and T is the absolute temperature.

The size-dependence of the equilibrium concentration culminates in the preferential dissolution of smaller particles. The resulting concentration gradients lead to the transport of solute molecules from small particles to larger ones.

1.6 Optical properties of QDs

An understanding of the optical properties of nanomaterials in general and QDs in particular is crucial for many of their applications. Burda *et al.* [57] reported that after QD excitation by light, three possible optical transitions can occur that are non-resonant, resonant and interband transitions corresponding to transition energies below, equal to and above the bandgap respectively. **Figure 1.6** shows the diagrammatic representation of absorption and emission

transitions. Spectroscopic techniques that can be used to probe these important transitions include absorption, transition differential absorption, photoluminescence excitation, fluorescence line and photoluminescence narrowing spectroscopy.

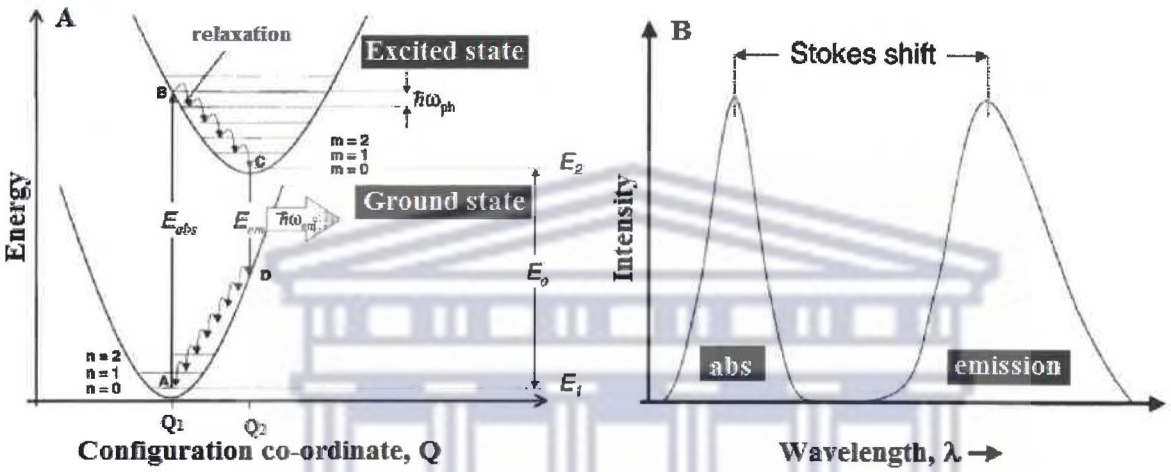

Figure 1.6 **A.** Configurational coordinate diagram illustrating the absorption and emission transitions as well as vibrational levels. **B.** An illustration of an absorption peak, a PL peak and the Stokes shift of a QD (reprinted with permission from [57], Copyright 2005, American Chemical Society).

The brief discussion in this section shall be focused only on two most commonly used techniques - absorption and photoluminescence spectroscopic techniques. Optical absorption in general allows the observation of the evolution of discrete features in absorption spectra (**Figure 1.7**). Inhomogeneous broadening, traceable to nanocrystal size, shape and defect distribution, if present, overshadows the discrete states rendering them invisible [57]. The process of fluorescence is defined as the spontaneous emission of radiation from fluorophores (organic molecules or inorganic semiconducting QDs) on the recombination of excitons [57]. Three stages are involved in the fluorescence process that are – i) excitation, ii) excited state lifetime

and iii) fluorescence emission. The excitation step is initiated by the absorption of a photon of energy that is greater than bandgap energy of the QDs [58]. This leads to generation of excitons. The exciton may return to the ground state via the radiative recombination of the electron and hole. Owing to the quantum confinement effect, QDs exhibit size-dependent photoluminescence.

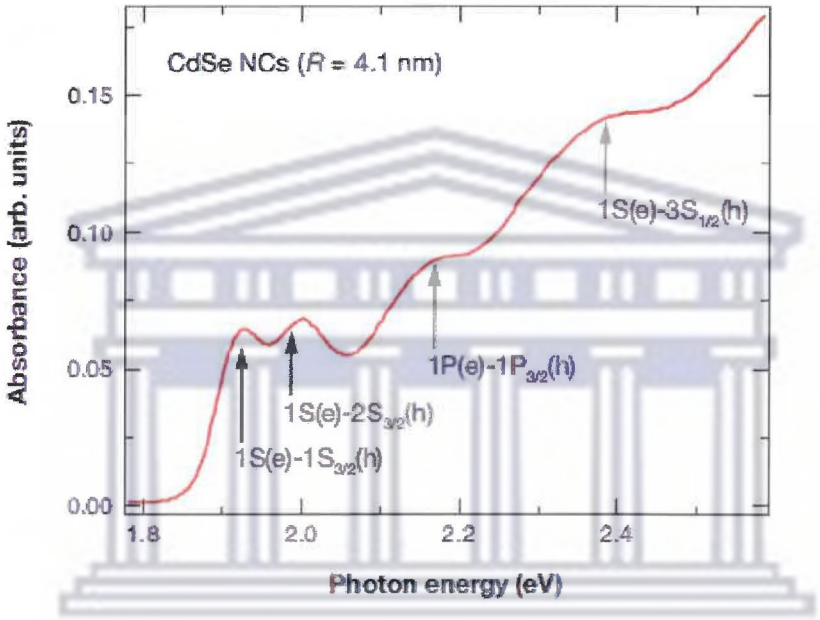

Figure 1.7 Linear absorption spectrum of 4.1 nm CdSe with arrows indicating four well-resolved transitions (reprinted with permission from [59], Copyright 2007, Annual Reviews).

1.7 QDs of group III-V

For more than two decades, research into semiconductor nanocrystals has been focused on the fabrication of versatile groups II-VI QDs owing to their potential application in lasers [60], light-emitting diodes [61], and more importantly biological studies [62,63]. However, due to the presence of highly toxic cadmium in the design, their biological application has been limited. In order to alleviate this toxicity problem, a process of overcoating the cadmium-based core with a

less toxic shell such as ZnS was developed. In this regard, the shell would prevent leakage of the toxic ions. Unfortunately this did not make the II-VI QDs completely innocuous as exposure to UV light or oxidation as a result of inflammatory responses induce the release of cadmium via surface oxidation [64]. The focus in the last two decades was therefore shifted towards the fabrication of III-V QDs in general, and InP in particular. The principal attraction to these semiconductors lies in the robustness of the covalent bond found in groups III-V semiconductor matrix compared to the ionic bond in the groups II-VI semiconductors. The presence of the covalent bond serves two functions, which are the enhancement of the optical stability of the QD systems as well as the reduction of the toxicity as a result of the non-erosion of the constituent species when used in biological milieu [65,66]. The other reason for the interest in the III-V systems lies in the fact that the excitonic Bohr radius is larger in III-V than in the II-VI systems (**Table 1.2**). Consequently, groups III-V QDs exhibit stronger size quantization effects in comparison with the groups II-VI systems [67].

Table 1.2 Band gap (E_g) and excitonic Bohr radius (r_B) in some semiconductors

Compound	Band gap (eV)	r_B (nm)	Reference
InP	1.35	15	[68]
InAs	0.354	34	[69]
CdS	2.43	5.8	[70]
CdSe	2.87	5.3	[71]
CdTe	1.5	7.3	[72]
ZnSe	2.67	4.5	[73]

1.7.1 Synthesis and optical properties of core and core/shell InP based QDs

The central part of a nanocrystal constitutes the core, and the immediate surrounding comprises the shell. In 1994, well-crystallized InP QDs with a zinc blende structure were synthesized for the first time [74]. A chloroindium oxalate complex (prepared from the reaction of indium trichloride and sodium oxalate) and tris(trimethylsilyl)phosphine [$(TMS)_3P$] were used as sources of indium and phosphorus respectively. A mixture of TOPO and trioctylphosphine (TOP) was used as a stabilizer and the reaction was carried out at 270 °C over three days. The nanocrystals were characterized by X-ray diffraction (XRD) and high resolution transmission electron microscopy (HRTEM) (**Figure 1.8**). X-ray diffraction data on the InP nanocrystal powders showed the ‹111›, ‹220› and ‹311› peaks of crystalline zinc blende InP at 2θ values of 26.2 ± 0.2°, 46.3 ± 0.2°, and 51.7 ± 0.2° respectively. HRTEM images showed that the particles were ellipsoidal rather than spherical in shape.

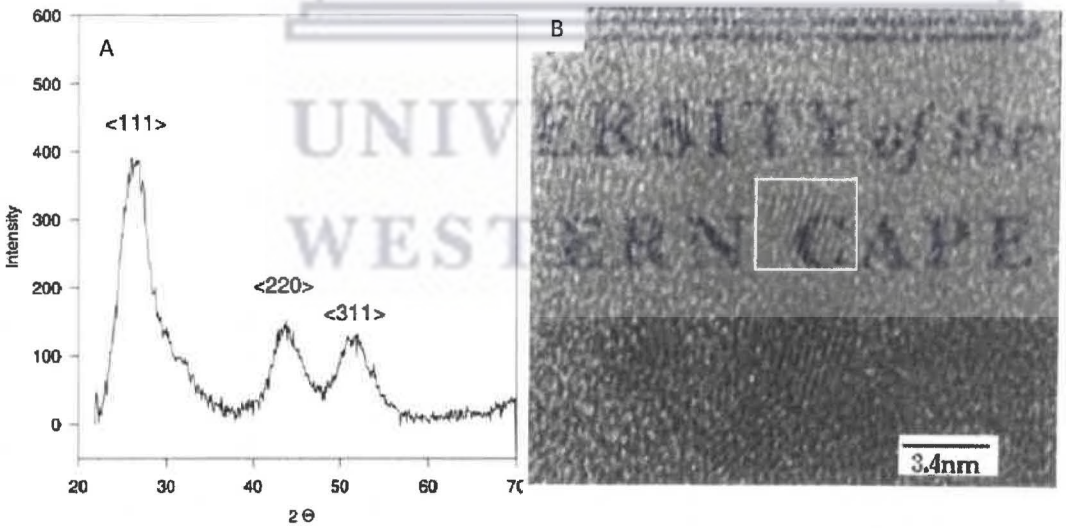

Figure 1.8 An X-ray diffraction pattern for dried InP QD exhibiting broadened prominent peaks for InP (A) and an HRTEM micrograph showing lattice fringes (B) (reprinted with permission from [74], Copyright 1994, American Chemical Society).

An optimization exercise for the properties of the obtained nanocrystals was done by changing the ratios of the In:P. A marked narrowing of the QD size distribution was obtained when indium was added in excess whereas the photoluminescence (PL) spectrum had two bands - one close to the band edge and the other above 800 nm (**Figure 1.9**) [75]. In the case of excess addition of phosphorus, only band edge emission was observed and the absorption spectrum did not show any resolved excitonic structure indicating a broad size distribution.

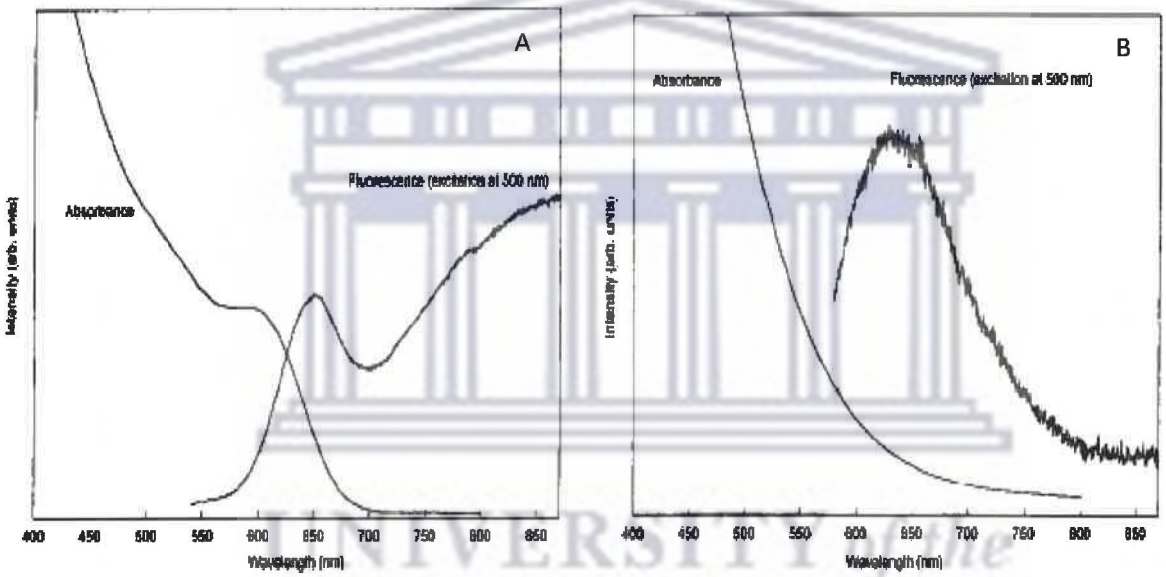

Figure 1.9 Room temperature absorption and PL spectra of InP QDs synthesized with different ratios of In and P – (A) In:P = 1.6; (B) In: P = 0.62 (reprinted with permission from [75], Copyright 1996, Elsevier).

Further optimization was achieved by the etching process [76]. The etching of the QDs by using HF produced a photoluminescence emission spectrum consisting of a single narrow peak near the absorption band edge with quantum yield (QY) of about 30 % after the treatment. The InP QD cores with a lattice-matched $ZnCdSe_2$ shell and photoluminescence QYs of 5-10 % have also

been synthesized [77]. However, it is worth noting that pre-etching the InP cores before shell growth results in poor core-shell structures as the HF blocks the surface of the QDs.

Kim *et al.* [78] synthesized InP/CdSe core/shell type structure showing an increase in QY at the beginning of the overcoating process due to the small difference between the InP and CdSe conduction bands of 0.19 eV which gives a type-I configuration, but changes to type-II which is associated with loss of QY yield with increased shell thickening. In such a synthesis, increase in the thickness of the shell should be avoided because it may result in a red shift, broadening of the full width at half maximum (FWHM) and a decrease in QYs. In 2009, InP/ZnS QDs with a diameter of 15-20 nm were reported [66]. Here, myristic acid was used as a stabilizer and octadecene as the non-coordinating solvent. The PL studies showed that the QDs exhibited a band edge emission at around 650 nm with QY of 25-30 %. These InP/ZnS QDs were further functionalized using mercaptosuccinic acid rendering them highly dispersible in aqueous media. The mercaptosuccinic acid-capped QDs were stable for more than one week while dispersed in a common physiological buffer such as the phosphate buffer saline (PBS).

Highly luminescent InP/ZnS nanocrystals were also synthesized following a single-step heating-up procedure [48]. Here, indium myristate, $(TMS)_3P$, zinc stearate and dodecanethiol were used for the fabrication of the nanocrystals which gave high fluorescence quantum yields (50-70 %). These high PL QYs are attributed to the nanocrystals possessing a radial composition gradient that relieves the strain due to the lattice mismatch between InP and ZnS.

A similar preparation was reported by another group but using step-wise process [79]. Again, palmitic acid was used as a stabilizer and octadecene as the non-coordinating solvent. The reaction between zinc acetate and palmitic acid gave acetic acid which causes the etching of the

surface of the InP core leading to the easy formation of the shell. A blue shift in the emission and an improvement in the quantum yield (38 %) were realized. The use of the poisonous PH_3 gas, generated from the reaction of a metal phosphide (calcium phosphide) with HCl as a phosphorus source in InP QD synthesis was also reported by Li *et al.* [80]. Again, octadecene and myristic acid were used as non-coordinating solvent and ligand, respectively. Unlike the single injection of $(TMS)_3P$, here the PH_3 gas is continuously and slowly generated and added in to the reaction system ensuring that the growth of the InP nanocrystals takes place in the size-focusing regime. The use of higher overall precursor concentrations resulted in the formation of a large number of nuclei and hence a smaller average size of the QDs. The PL spectra of the as-prepared InP nanocrystals showed two additional bands around 730 and 820 nm. These bands were attributed to trap-state related emissions, which are suppressed upon overcoating with ZnS obtained from the monomolecular zinc ethylxanthate precursor. The PL QY of up to 22 % was achieved [80]. In a different experiment, the as-synthesized bare InP nanocrystals, prepared using PH_3 gas, did not exhibit detectable photoluminescence owing to the presence of surface states [81]. However, when overcoated with a ZnS shell, a very strong PL intensity was observed, which was attributed to the passivation of these surface states by the inorganic shell. The emission profiles of the InP core varied as a function of size in the range of 600-700 nm while the 470 nm band is attributed to defect –related emissions from the shell (**Figure 1.10**).

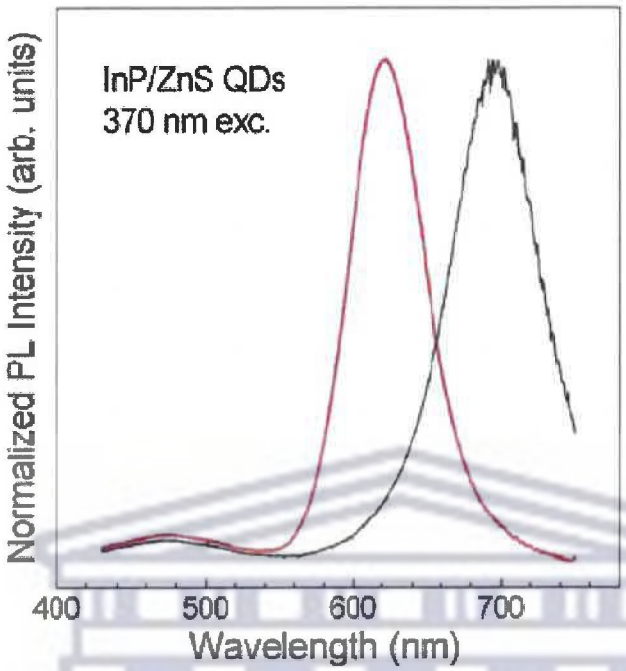

Figure 1.10 Steady-state photoluminescence spectra of two different sized InP/ZnS QD samples under the 370 nm excitation (reprinted with permission from [81], Copyright 2009, IOP Publishing Ltd).

The molar ratios of indium to phosphorus of 2:1 give the best quality InP nanocrystals when the non-coordinating octadecene is used as a solvent [82,83]. When the ratios of the metal to ligand are above or below this ratio, the reaction gives nanocrystals with no distinguishable UV-Vis spectral features, implying that the size distribution is broad. The use of the ZnS coating layer gives the red-shift in both the absorption and PL spectra of about 2-3 nm (**Figure 1.11**) as well as an improvement in the PL QY from <1 to ~20 % [83].

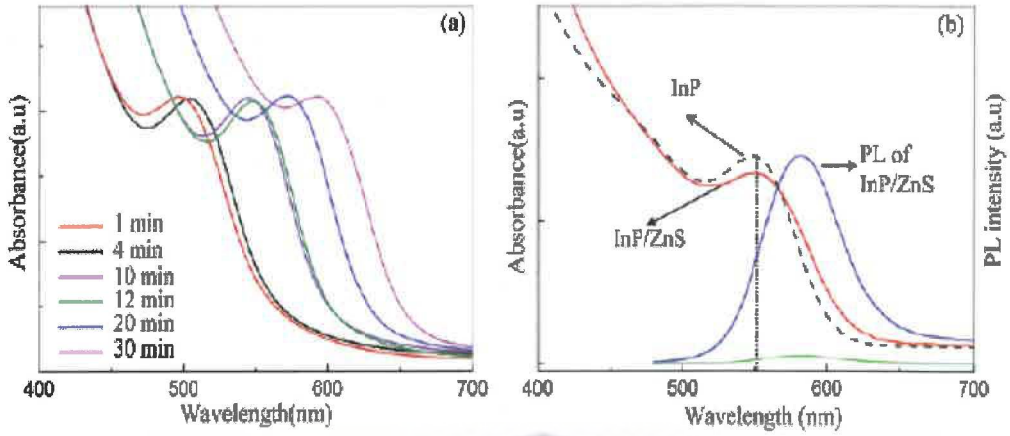

Figure 1.11 (a) Temporal evolution of the UV-vis spectra of InP nanocrystals in ODE. (b) UV-vis spectra of InP nanocrystals before (black dashed) and after (red solid) passivation with ZnS and PL spectra of InP (green solid) and InP/ZnS nanocrystals (blue solid) (reprinted with permission from [83], Copyright 2008, American Chemical Society).

Myristic and palmitic acids, which are fatty acids of intermediate chain length, serve as the best ligands for controlled nucleation growth rates that yield relatively monodisperse nanocrystals when the ratio of the fatty acid to indium is 3:1 [82]. Uniquely, a 'green' approach where by high quality InP nanocrystals are synthesized without the addition of a coordinating solvent or ligands, using indium carboxylates as precursors for indium was reported [84]. The carboxylate ions act as the *in situ* coordination ligands. The usage of weakly coordinating fatty acid esters in the preparation of high-quality InP QDs is known [85]. In these reactions, trimethylindium is used. It readily dissolves in the ester at room temperature and generates a soluble indium-ester complex with a higher activity than the indium carboxylate. The reported reaction pathway for this reaction is given in **Scheme 1.1**.

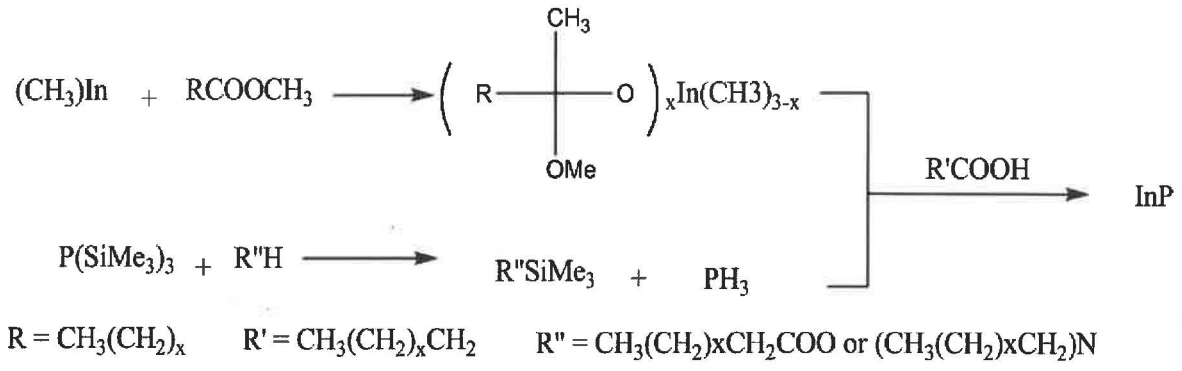

Scheme 1.1 Proposed reaction scheme through an indium-ester intermediate [85].

The FWHM of the produced InP QD PL spectra is about 60 nm. When protic reagents such as amines are used, they hydrolyze $(TMS)_3P$ thereby accelerating the reaction with the indium precursors, but reducing the FWHM to around 48 nm. The role of the fatty acids and the protic reagents is mainly to increase the polarity of the reaction media affording better solubility as well as homogeneity of the precursors culminating in rapid but controlled reactions [86]. Polyethylene glycol (PEG) has been used as a weakly coordinating solvent for the one–pot synthesis of InP/ZnS QDs [86]. PEG offers the major advantages that it is nontoxic, inexpensive and recyclable. The InP/ZnS QDs prepared in the PEG medium have quantum efficiencies as high as 30 % with emissions ranging from 500 to 655 nm with FWHM of approximately 46 nm. Extremely small InP QDs have also been synthesized in a reaction where the protic reagents are used and heating carried out at 100-220 °C for a day [87]. Portiere and Reiss also reported the activation effects of amines in their preparation of In_2O_3-coated InP QDs giving an emission profile of 583 nm and FWHM of 50-60 nm [88]. The shell growth was done *in situ* without an addition of any precursor, but was induced by oleylamine which was added at the start of the reaction. In 2010, Bawendi's group published a mechanism for the formation of InP QDs

(**Scheme 1.2**) [89], demonstrating that amines inhibited precursor decomposition, contrary to the above reports that they are activating agents in the synthesis.

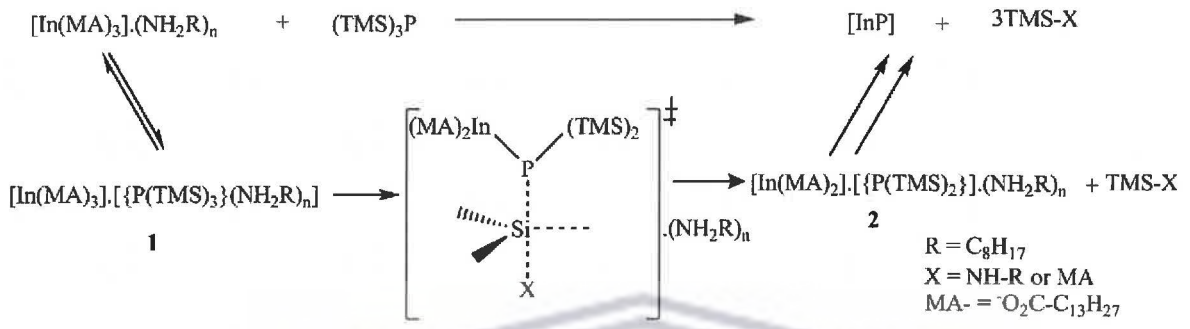

Scheme 1.2 Proposed mechanism for amine inhibited InP synthesis [89].

According to the scheme, amine inhibition resulted from solvation effects associated with steps that lead to the formation of complexes **1** and **2**. Both the amine and $(TMS)_3P$ compete for the same indium metal centre and hence an increase in the concentration of the amine decreases the formation of complex **1** as the sterically hindered phosphine precursor is less likely to approach the metal centre. During the nucleation step, molecular phosphorus precursors are completely used up. As a result, subsequent growth in nanocrystal sizes is exclusively due to ripening from non-molecular InP species giving rise to broad size distributions.

Murase and co-workers [90] reported a low temperature solvothermal synthesis of InP nanocrystals that gave a broad size distribution due to a lack of separation of the nucleation and growth steps. UV irradiation of the nanocrystals in the presents of Zn^{2+} ions and thioglycolic acid yielded a thick ZnS shell and improved their PL efficiencies (30-68 %). When the HF etching of the InP cores preceded the ZnS coating step, a blue shift in the absorption spectra was observed and this was ascribed to a slight QD size reduction during the etching process, while the

observed improvement in the photoluminescence was due to a partial surface oxidation of the InP QD surfaces [68].

Another green chemistry approach recently documented involves the usage of an aqueous synthetic route to InP QDs. The system uses an indium oxide, In_2O_3 and white phosphorus, P_4 for the synthesis of the InP core [91]. The formation of the InP nanocrystals (**Scheme 1.3**) was confirmed by both the X-ray photoelectron spectroscopy and energy-dispersive X-ray (EDX) analyses that gave In:P ratios of 1:1.02 and 1:1.01 respectively.

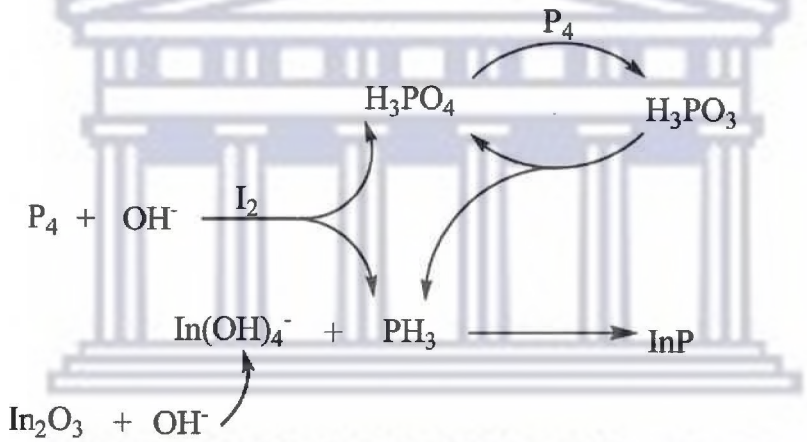

Scheme 1.3 Growth pathway to InP QDs adapted from the GaP scheme [91]

However, this synthetic route produces larger-sized nanocrystals with poor size distribution. Yet another approach by Green and O'Brien involves the pyrolysis of a single source precursor $In(PBu_2^t)_3$ in 4-ethylpyridine at 167 °C to give large InP QDs [92]. The nanocrystals obtained were about 7 nm in diameter with the PL spectrum exhibiting a broad near-band-edge luminescence peak at 534 nm. No QY data was reported here. A coreduction colloidal method for the synthesis of relatively high quality InP nanocrystals using indium acetate, PCl_3 and a

superhydride $LiBH(C_2H_5)_3$ and stearic acid is equally known [93]. In this heating-up type synthesis in the presence of non-coordinating octadecene, the simultaneous reduction of the indium and phosphorus precursors was carried out at low temperature followed by the elevation of the temperature to around 250-270 °C for growth of the InP nanocrystals. The PL spectra containing both a high energy band edge and a low energy surface trap-related emission were obtained. Post-treatment of the cores with the etchant HF resulted in the fluorescence intensity increasing by a factor of 80 and the PL efficiency improved from about 0.25 % to about 20 %.

1.7.2 Alloying and doping of the InP QDs

Most of the prepared QDs are binary in nature. The binary QDs have the size of the nanocrystals, and hence the emission profile is controlled by a systematic adjustment of the reaction parameters namely temperature, time and concentration of both the precursors and surfactant molecules. The emission profiles of alloyed III-V nanocrystals can be fine-tuned using composition as well, allowing them to emit in the near-infrared region. One such system, $InAs_xP_{1-x}$/InP/ZnSe, with a PL QY of about 3.5 %, has been reported [94]. Another alloyed QD system, InGaP, was synthesized using a microwave-enhanced method [95]. The cationic intermediates of indium and gallium were prepared by mixing indium(III) acetate, gallium(III) 2,4-pentanedionate, hexadecanoic acid and 1-octadecene followed by heating the mixture at 110 °C for 2 h. Tris(trimethylsilyl)phosphine was then added at 50 °C and the In/Ga/P precursor solution was heated in a microwave oven at temperature and power of 280 C and 280 W to afford the InGaP nanocrystals (**Figure 1.12**).

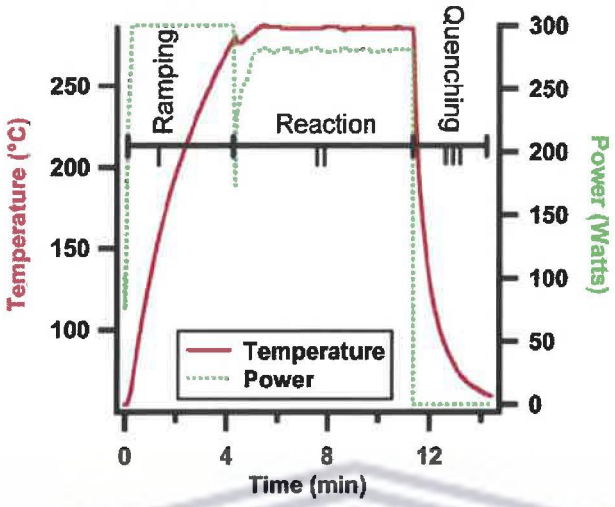

Figure 1.12 Temperature (°C) and power (W) profiles of a typical InGaP reaction. Region I shows temperature ramp done at 300 W until desired temperature (280 °C) is reached. Region II is the reaction time during which temperature and power were maintained at 280 °C and 280 W. Region III is when reaction is complete and thermally quenched by compressed air (reprinted with permission from [95], Copyright 2005, American Chemical Society).

QYs of about 15 % were obtained prior to etching and improved to 68 % upon etching due to the passivation of surface states.

There are a few literature reports on the doping of InP QDs and this is attributed to the low solubility of the dopants in group III-V semiconductor matrix [96,97]. Manganese-doped InP QDs were obtained by using the high temperature dehalodesilylation and injection methods in a coordinating solvent. The PL studies showed only small differences between the doped and pure samples. In another report, InP:Mn QDs gave a PL spectrum with a maximum peak at 570 nm and a FWHM of 110 nm. However, it was not feasible to estimate the contribution of the dopant to the overall PL property of this system [98]. Copper-doped InP/ZnSe (Cu:InP/ZnSe) QDs, have also been reported, exhibiting emission profiles that could be tuned from 630-1100 nm, thus covering the critical near-infrared (NIR) window for biomedical applications [99]. In these

copper-doped QDs, the band edge emission from InP is eliminated (**Figure 1.13**) and pure dopant emission, with PL QYs of up to 40 % is attained.

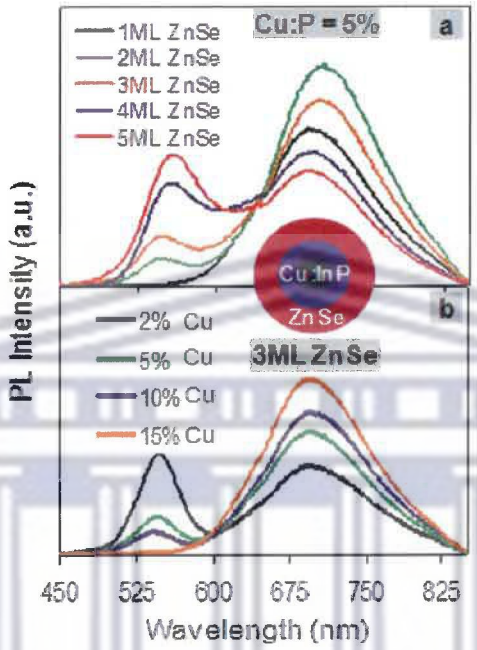

Figure 1.13 PL spectra of Cu:InP d-dots (5% of Cu:P precursor ratio) with different thicknesses of ZnSe shells (a) and PL spectra of Cu:InP/ZnSe QDs formed with different Cu:P precursor ratios (b) (reprinted with permission from [99], Copyright 2009, American Chemical Society).

1.8 QD surface chemistry

Luminescent QDs have found a wide range of applications in biotechnology and medicine. These biological applications require water-soluble QDs [100]. QDs are normally synthesized via the organometallic route in the presence of hydrophobic surfactants such as TOPO. A lot of research effort has gone into providing biocompatible organic interfaces that on the one hand solubilize

the QDs while maintaining their photophysical properties in biological milieu and on the other hand providing functional groups for subsequent conjugation to biomolecules.

1.8.1 Water solubilization strategies

The strategies for introducing the hydrophilic capping ligands fall under (a) ligand exchange and (b) ligand shielding chemistries [101].

1.8.1.1 Ligand exchange chemistries

Bi-functional capping agents are introduced after QD synthesis to replace the native organic capping layer [102]. These capping agents comprise of a surface anchoring moiety (e.g. thiol group) and a hydrophilic end (e.g. carboxyl group, hydroxyl or PEG). In 1998, Chan and Nie [103] reported the use of mercaptoacetic acid for the solubilization of CdSe/ZnS core/shell QDs. The mercapto group coordinates to the metal centre while the polar carboxylic acid group renders the nanocrystals soluble in the aqueous environment. Bidentate capping agents such as dihydrolipoic acid (DHLA) and dithiothreitol have also been introduced in order to produce more stable caps than the monodentate ones. This stability is attributed to the chelate effect where two thiol groups coordinate to the inorganic surfaces of the QDs simultaneously [104,105]. **Figure 1.14** shows a QD surface functionalized using DHLA.

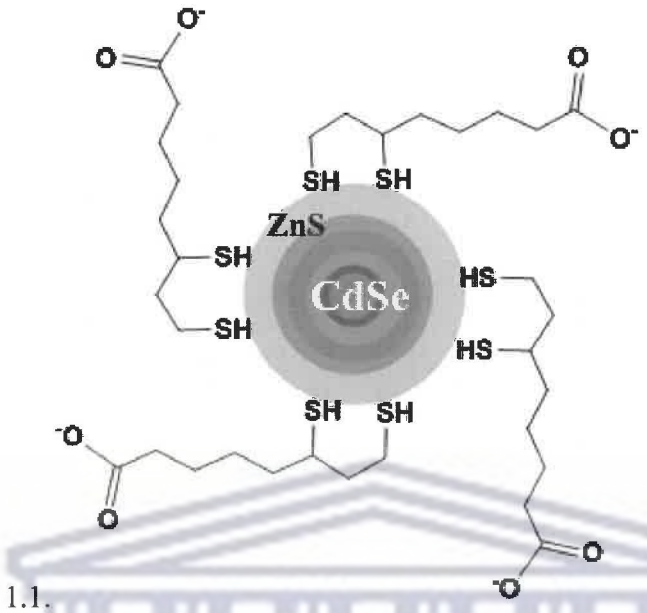

1.1.

Figure 1.14 CdSe/ZnS QD capped by dihydrolipoic acid layer [104]

Silanization reactions have also been employed to solubilize hydrophobic QDs. Bruchez *et al.* [106] reported the use of silica on CdSe/ZnS QDs. 3-(mercaptopropyl)trimethoxysilane was directly adsorbed onto the nanocrystal surface.

1.8.1.2 Surface shielding chemistries

The surface ligand shielding retains the hydrophobic capping layer through encapsulation or coating with phospholipid micelles [107] or amphiphilic diblock and triblock copolymers [108,109]. Amphiphilic polymers that contain a hydrophobic segment (mostly hydrocarbon chain) and a hydrophilic segment (polyethylene glycol or carboxylate groups) can be used to encapsulate the hydrophobic QDs. The interlocking of the native hydrophobic ligands on the QD surface with the hydrophobic groups on amphiphilic polymers allows the native capping layer to

remain intact as well as the retention of the QD's quantum efficiency [110]. The resulting polymer-encapsulated QDs have been reported to be essentially non-toxic to cells [111]. There are several reported examples of polymers that have been used in the solubilization of QDs. Luccardini *et al.* [112] reported the surface coating of CdSe/ZnS QDs with alkyl-modified poly(acrylic acid)-based amphiphilic polymers as depicted in **Figure 1.15**.

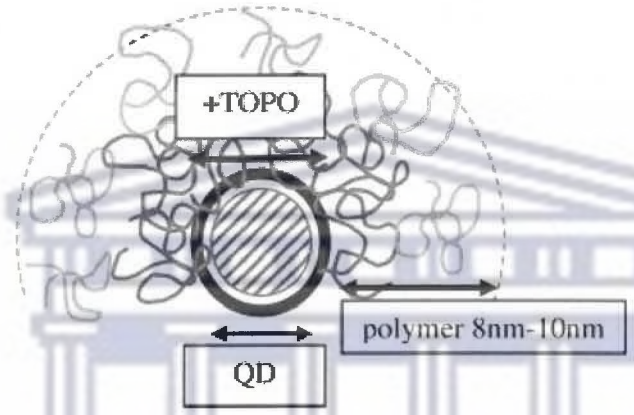

Figure 1.15 Sketch of a QD coated with amphiphilic polymers (reprinted with permission from [112], Copyright 2006, American Chemical Society).

The thickness of the adsorbed monolayers of the polymers was comparable to the polymer radium in solution. Gao *et al.* [113] used 100 kDa amphiphilic triblock copolymer that consisted of a poly(butylacrylate) segment, a poly(ethylacrylate) segment and a poly(methylacrylate) segment for the encapsulation of TOPO-capped CdSe/ZnS QDs (**Figure 1.16**). Subsequent pegylation of the polymeric shell afforded polymer-coated QDs whose optical properties were stable over a broad pH range (1-14).

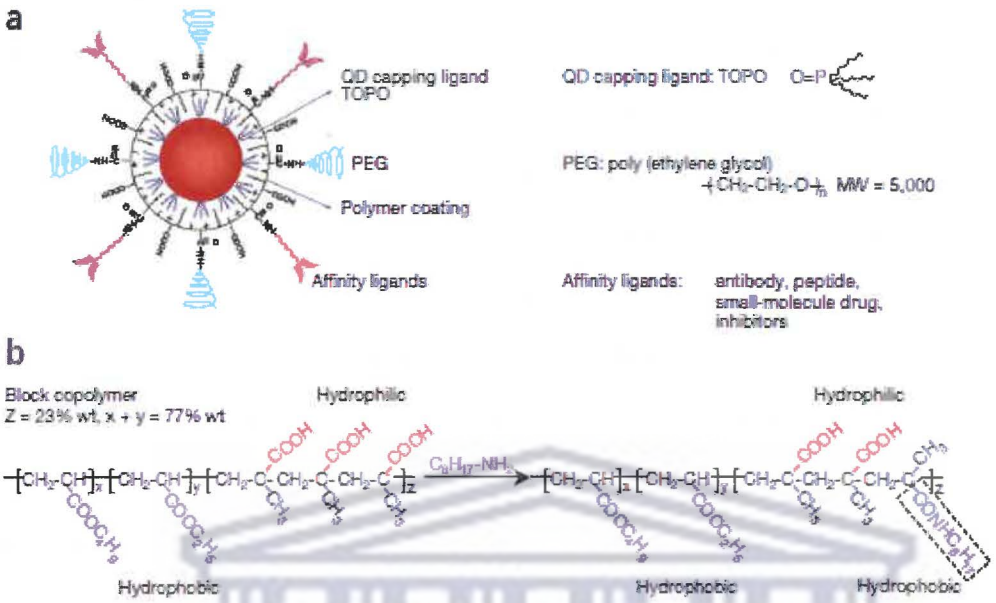

Figure 1.16 (a) Schematic representation of a QD coated with a triblock polymer that is shown in (b) (reprinted with permission from [113], Copyright 2004, Nature Publishing Group).

Another polymer that has been used for encapsulating QDs is poly(maleic anhydride alt-1-tetradece), a low molecular weight polymer [114]. The polymer was cross-linked with bis(6-aminohexyl)amine to increase the polymer shell stability. Agarose gel electrophoresis of the polymer coated nanocrystals showed that they had a homogeneous distribution of sizes and charges. A survey of polymers that have been used for QD coating via hydrophobic-hydrophobic interactions is given in **Table 1.3**.

Table 1.3 Survey of polymers used for QD coating via hydrophobic-hydrophobic interactions [115]

Polymer coating	QD type	Width of the polymeric shell
Poly(maleic anhydride alt-1-tetradecene)	CdSe/ZnS	6-7 nm
Amphiphilic triblock copolymer	CdSe/ZnS	2 nm
Alkyl-modified poly(acrylic acid)	CdSeZnS	8-10 nm
Polymer-modified phospholipids	CdSe/ZnS	3-6 nm
Gallate amphiphile with PEG	CdSe/ZnS	7-15 nm

Overcoating QDs with a silica shell either by surface silanization (ligand exchange) or indirect silica encapsulation can also be used as strategy for rendering QDs water compatible. In 1995, Darbandi *et al.* [116] reported a novel method of encapsulating QDs in silica shells using a microemulsion synthetic technique. These authors proposed two hypothetical mechanisms for the microemulsion process (**Figure 1.17**) .

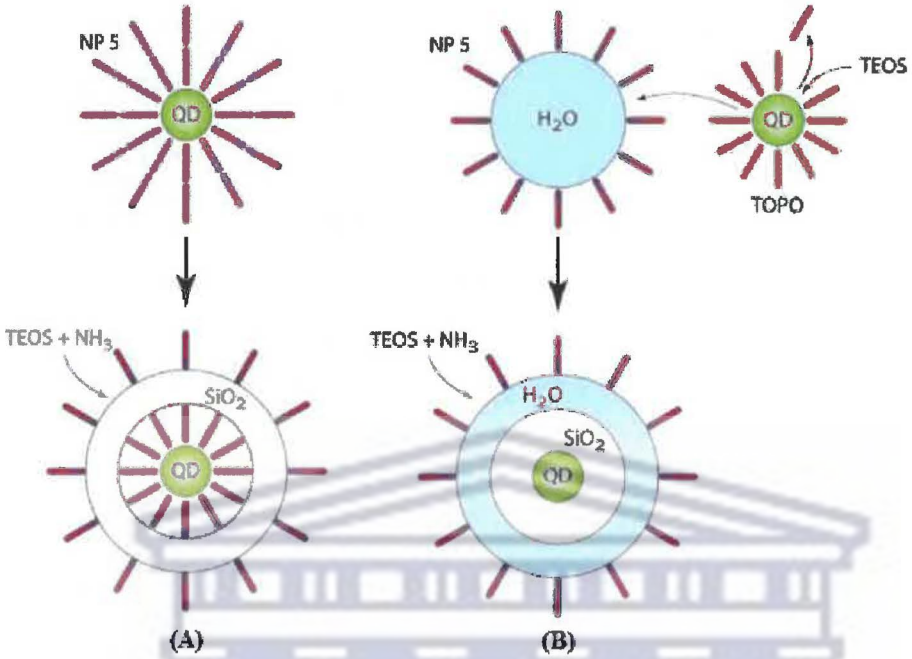

Figure 1.17 Schematic diagram of the two mechanisms of silica shell growth on the QDs. Path **A** is shell growth without ligand exchange and **B** is growth with ligand exchange and phase transfer (reprinted with permission from [116], Copyright 2005, American Chemical Society).

In path **A,** the Snyperonic NP-5 (NP-5) surfactant formed an inverted bilayer around the TOPO-capped CdSe/ZnS QDs followed by the growth of a silica shell on addition of ammonia catalyst for tetraethyl orthosilicate (TEOS) polymerization. In path **B**, the TOPO ligands were first replaced by TEOS allowing phase transfer of QDs into the aqueous phase. Subsequent polymerization took place on addition of catalyst. Parak *et al.* [117] also reported the synthesis of charged phosphonate and PEG/ammonium silane- and neutral PEG-silane-coated CdSe/ZnS QDs (**Figure 1.18**).

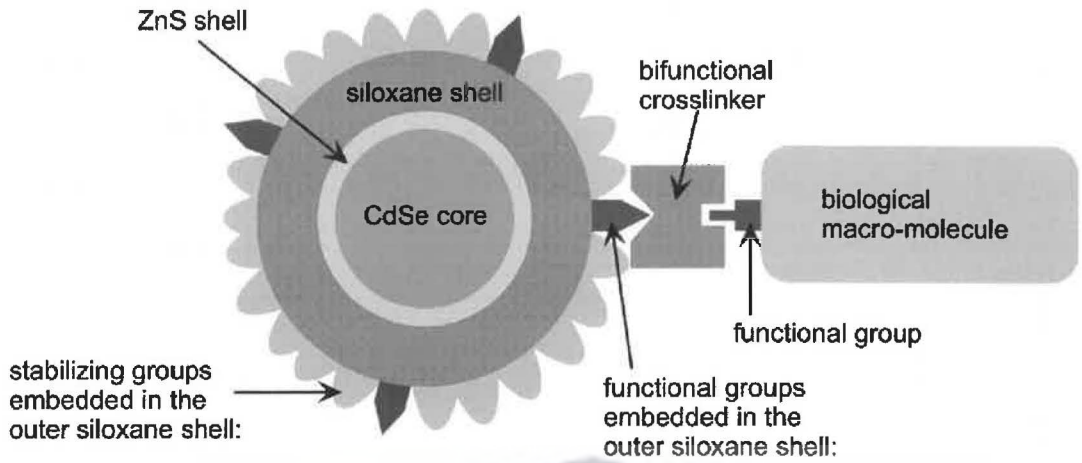

Figure 1.18 Schematic diagram of QD-biomolecule conjugate with the CdSe/ZnS QD embedded in a siloxane shell. Phosphonate, PEG or ammonium groups on the outer siloxane surface act as stabilizers to maintain water compatibility while thiol, amine or caboxyl groups are incorporated in the shell as functional groups (reprinted with permission from [117], Copyright 2002, American Chemical Society).

1.8.2 Biofuntionalization strategies

QDs are conjugated to biomolecules to make them applicable to molecular imaging and other biological applications. The three modes of attaching biomolecules to QDs that are commonly employed are (a) covalent attachment, (b) direct attachment of biomolecules to the surface of the QDs and (c) non-covalent electrostatic interaction.

1.8.2.1 Covalent attachment of biomolecules to surface ligand

Covalent attachment of biomolecules to the QDs takes advantage of functional groups such as amines, thiols and carboxyl present on the capping layer (**Figure 1.19**).

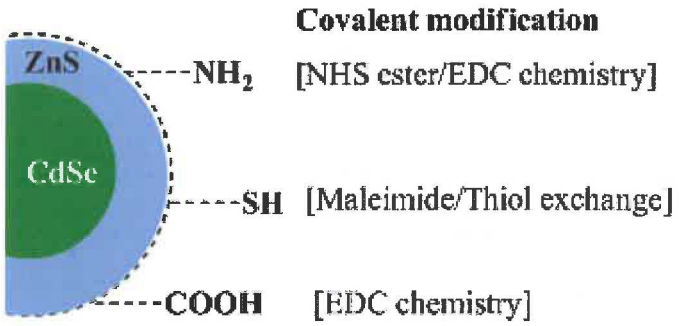

Figure 1.19 Schematic display of the covalent attachment strategy [118]

As most of the water solubilization strategies result in QDs with a capping layer containing amine, thiol and carboxyl functional groups, linking these QDs to biomolecules containing similar groups is feasible. Cross-linkers 1-ethyl-3-(3-dimethylaminopropyl) carbodiimide (EDC) and N-hydroxysuccinimide (NHS) are used in linking $-NH_2$ terminated QDs to biomolecules containing terminal –COOH groups. The thiol functional groups are sites for attachment by maleimide chemistry thiol exchange reactions. Using EDC chemistry, carboxyl terminated QDs can also be attached to amine-terminated biomolecules. Covalent coupling provides the most robust form of attachment of biomolecules to QDs [119]. Various biomolecules including peptides [120], oligonucleotides, biotin [106], antibodies [121] and protein molecules including avidin/streptavidin [121] have been conjugated to QDs using this mode of attachment. Prasad's group reported the covalent attachment of several biomolecules to Si QDs via the covalent coupling strategy [122]. The group was able to successfully image human pancreatic cancer cells (Panc-1) using the QDs tagged with folate, apo-transferrin and antimesothelin. Using QDs encapsulated in phospholipid micelles, Dubertret *et al.* [123] reported the covalent attachment of the QDs to thiol-modified DNA. In this work, it was demonstrated that QD-micelles coupled to oligonucleotides did not prevent hybridization of the oligonucleotides to complementary DNA

targets. In 2010, Chen and coworkers labeled polymer-coated InAs/InP/ZnSe QDs with the thiolated arginine-glycine-aspartic acid (RGD) peptide covalently using maleimide chemistry. These QD-peptide conjugates were then used for *in vivo* imaging integrin $\alpha_v\beta_3$–positive tumor vasculature. In 2011, Bruce's laboratory reported the carbodiimide-mediated coupling of QDs to antibodies providing new mechanistic insights into the coupling reaction under basic conditions (**Figure 1.20**) [124]. The QD-Ab conjugates were significantly resistant to photobleaching and the optimum pH for coupling was 10.8.

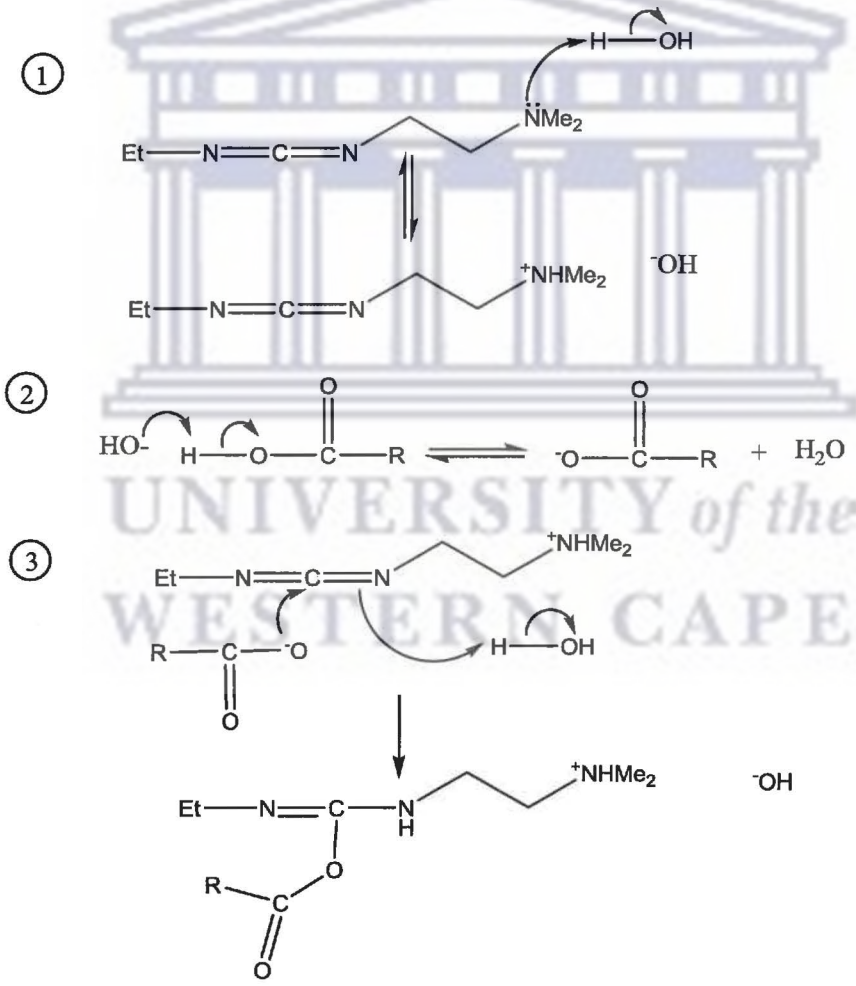

Figure 1.20 **(a)** Mechanism for EDC mediated carboxyl-amine coupling under basic conditions. Steps 1-3 involve the formation of isoacylurea [124].

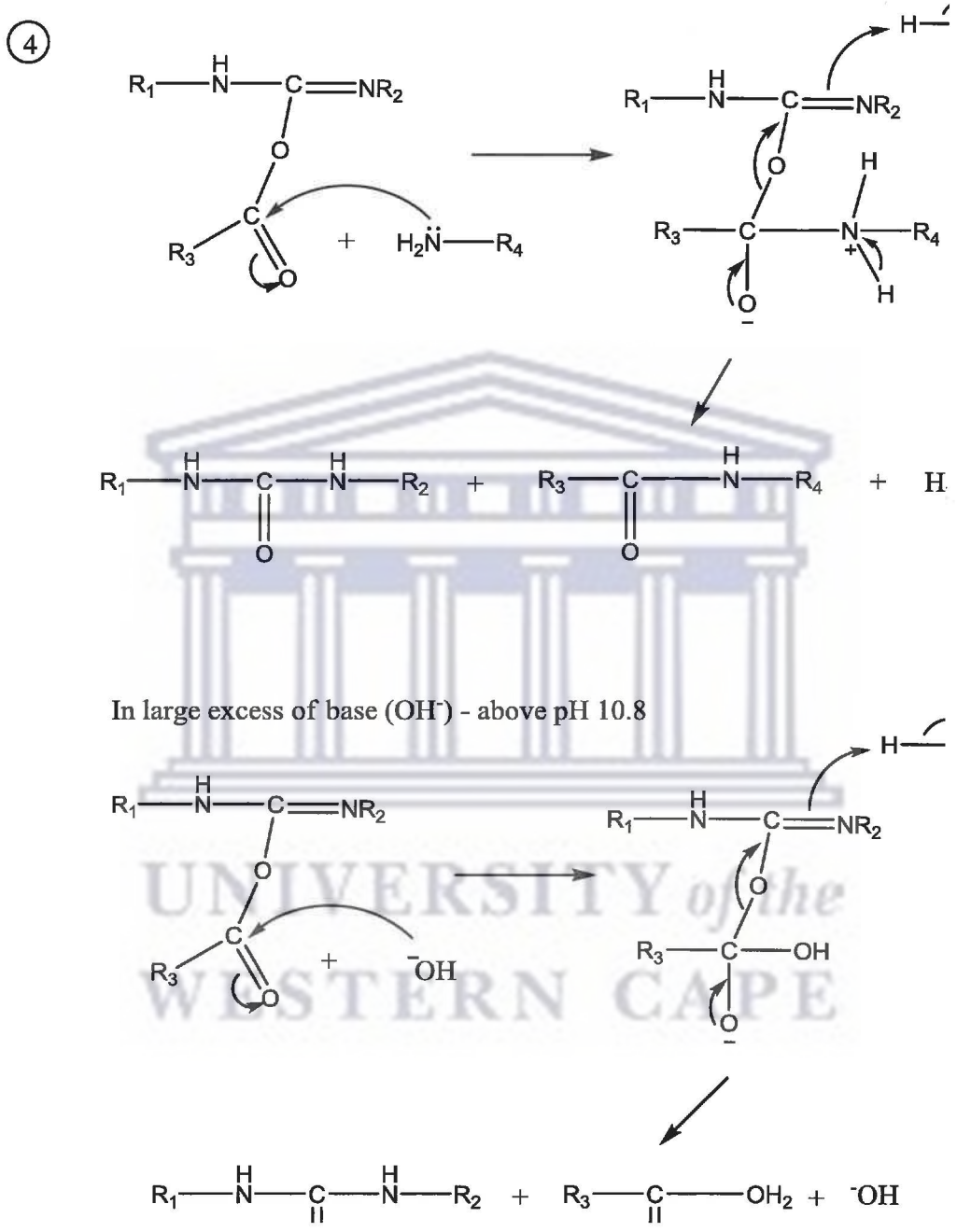

Figure 1.20 (b) Step 4 involves conjugation and reaction likely to occur in excess base [124].

1.8.2.2 Direct attachment of biomolecules to QDs

Direct conjugation of biomolecules to QDs surfaces can be effected through dative thiol bonding of sulfur groups from the biomolecules to the surface sulfur in ZnS-coated QDs [120]. This mode of attachment has been employed by Weiss' group using phytochelatin-related peptides containing multiple cysteine residues both to cap the CdSe/ZnS QD surfaces and impart bioactivity. They have shown that the peptide coating that is effected in a single-step reaction affords superior colloidal properties causing red-shift in both the absorption and emission spectra of the QD systems attributed to exciton-molecular orbital coupling. Metal-affinity coordination of polyhistidine (His) appended protein molecules to the ZnS shell of core/shell QDs has also been reported as a method for conjugating biomolecules [125]. The QD-His interactions have very strong binding affinities ($K_d^{-1} \sim 1 \times 10^9\ M^{-1}$) making the bioconjugates stable in cellular environments. Liu *et al.* [126] have reported the use of metal affinity coordination to couple His6-streptavidin to QDs for targeted cell labeling. **Figure 1.21** shows a schematic display of direct bonding of biomolecules to QDs using either dative thiol bonding or metal affinity coordination.

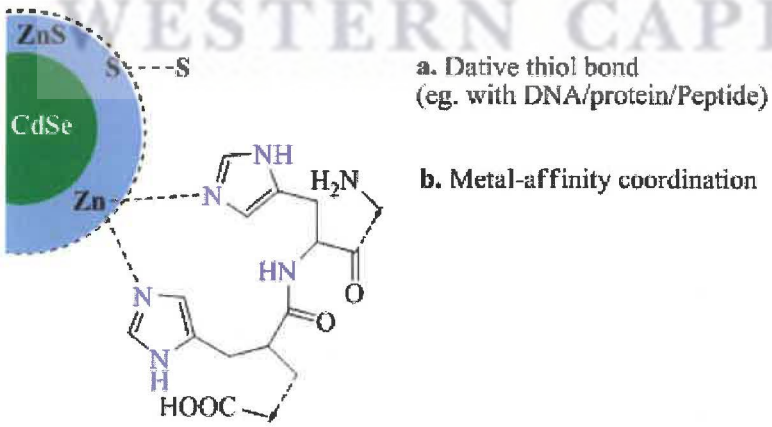

Figure 1.21 Schematic display of direct conjugation of biomolecules to QD [118]

1.8.2.3 Non-covalent electrostatic interaction

This is a strategy designed to provide multipurpose QD-protein bioconjugates based on non-covalent assembly. Mattoussi *et al.* [104,127] have reported on the electrostatically driven self-assembly of CdSe/ZnS QDs capped with negatively charged carboxyl-terminated dihydrolipoic acid with engineered recombinant proteins bearing a positively charged attachment domain. Maltose-binding protein dimers appended with leucine zipper domain (MBP-zb) in combination with protein G were used to prepare the self-assembled QD-protein conjugates. The MBP-zb allowed for the purification of the bioconjugated over amylose resin and the protein G provided sites for attachment of antibodies.

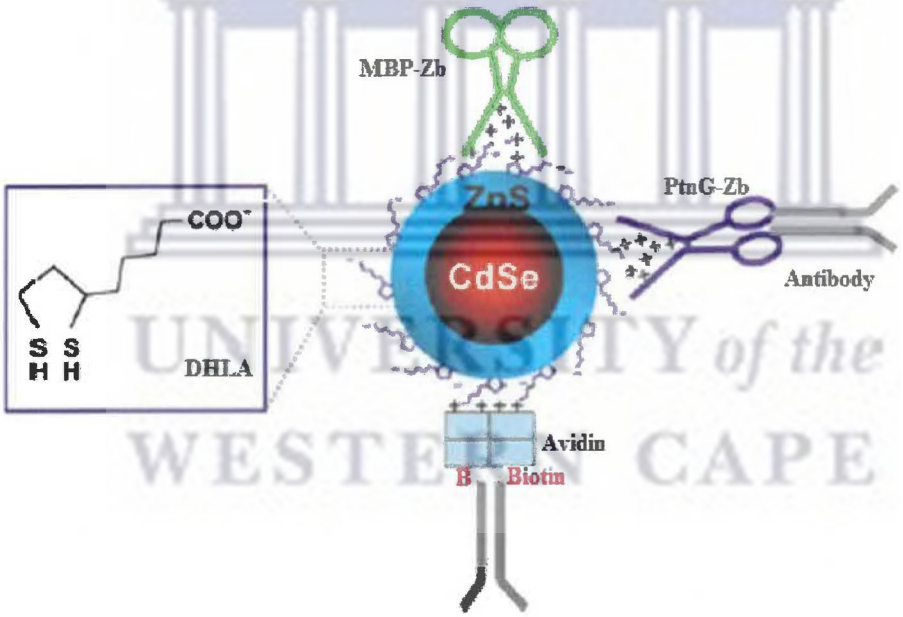

Figure 1.22 Schematic diagram of a mixed surface DHLA-capped CdSe/ZnS QD with a protein G dimer appended with a leucine zipper domain (PtnG-Zb), an MBP-Zb and positively charged avidin (reprinted with permission from [128], Copyright 2005, Springer-Verlag).

The driving force for the adsorption of protein molecules onto the QDs is charge-charge interaction [129]. The advantage of the self-assembly strategy is that it can easily be applied to other QDs systems such as group III-V. The self-assembly strategy provides a general approach of preparing a wide selection of biomolecules amenable to changes in the interaction domain such as charge and stability to temperature and pH.

1.9 Applications of QDs in biology

Chan and Nie [103] and Bruchez *et al.* [106] have pioneered the use of colloidal QDs in biology through their publications that appeared in the journal *Science* in 1998. A lot of research effort has followed after these publications, as evidenced by numerous reviews on the applications of quantum dots in biology [130-135]. This section shall therefore be limited to briefly discussing methods of delivering QDs into tumor cells as well as reviewing their use in nanomaterials in cancer and obesity diagnostic and therapeutic studies.

1.9.1 Delivering QDs into tumor cells

The strategies that are followed for the targeting of QDs into cells can be grouped into two classes that are passive and active targeting.

1.9.1.1 Passive targeting

Passive targeting is a strategy in which QDs accumulate at tumor site via the enhanced permeability and retention (EPR) effect [136]. The particles leak from the blood circulation into

the tumors which are sites lacking effective lymphatic drainage system. Passive targeting takes place either by convection or passive diffusion [137] with the former involving movement of molecules through the fluid and the latter involving movement of particularly low molecular weight molecules through diffusion [138]. However, the process of convection is poor owing to interstitial hypertension, leaving diffusion as the major player in passive targeting. Passive targeting relies on both size and surface properties of the QDs with the EPR effect more optimal when the nanoparticle carriers can circulate for longer periods. Iyer *et al.* [139] reported that very high local concentrations of drug-carrying nanoparticles (10-50 –fold higher than in normal tissues) can be attained at the tumor sites within 1-2 days. Some drawbacks of passive targeting have been identified. The high interstitial fluid pressure that is associated with solid tumors renders successful uptake and homogeneous distribution of the drug difficult [140]. As the targeting mode also depends on the degree of both tumor vascularization and angiogenesis, the process of extravasation of the nanoparticle carriers will vary with tumor types [141]. **Figure 1.23** shows a schematic diagram of nanotechnology-based drug delivery systems.

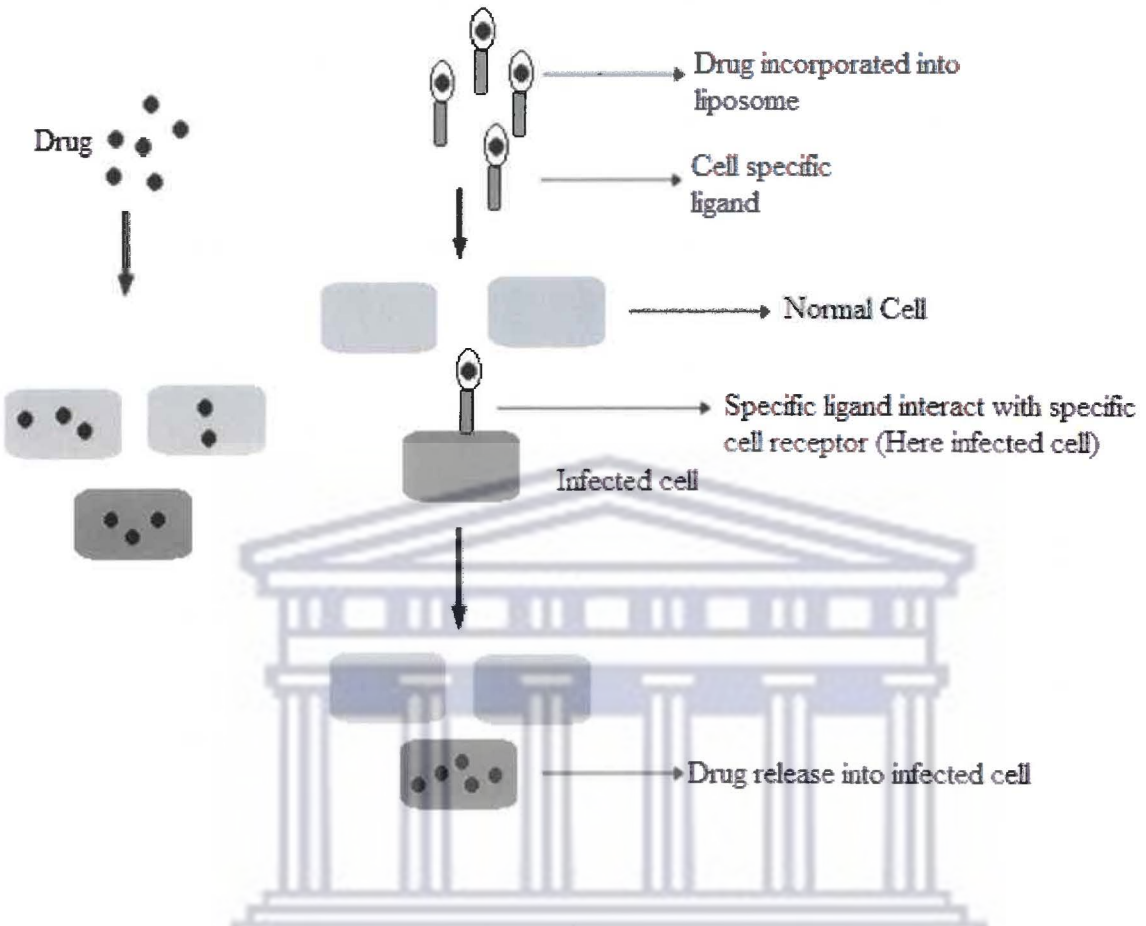

Figure 1.23 Schematic diagram showing drug delivery system using nanotechnology [142].

1.9.1.2 Active targeting

In active targeting, the QDs are bioconjugated to specific targeting molecules possessing a high affinity for unique molecular signatures that are found on tumor cells [54]. These molecular signatures or receptors should be exclusively or overexpressed by the tumor cells or its vasculature. The type of the targeting moiety has a bearing on the mechanism of cellular uptake of the drug carriers. Targeting ligands that allow for the internalization of their cargo have been reported to be associated with increased drug therapeutic effects [143]. Representative cell penetrating peptides (CPPs) are listed in **Table 1.4**.

Table 1.4 A brief survey of CPPs, their origins and sequences [144].

Peptides	Origin	Sequence
TAT	HIV-TAT protein	PGRKKRRQRRPPQ
Penetratin	Homeodomain	RQIKIWFQNRRMKWKK
Pep-1	Trp-rich motif –SV40 NLS	KETWWETWWTEWSQPKKKRKV
MAP	Chimeric	KALAKALAKALA
SAP	Proline-rich motif	VRLPPPVRLPPPVRLPPP
Oligoarginine	Chimeric	Agr8 or Arg9
hCT(9-32)	Human calcitonin	LGTYTQDFNKTFPQTAIGVGAP

Akerman *et al.* [145] were the first to demonstrate the use of QD bioconjugates bearing homing peptides F3 (which targets blood vessels and tumor cells) and LyP-1 (that targets lymphatic vessels and tumor cells in certain tumors). *In vitro* histological results on tissues from mice injected intravenously with the QD-peptide conjugates showed that the QDs homed to the tumor vessels.

1.9.2 Use of QDs in cancer and obesity diagnostic studies

1.9.2.1 Cancer diagnosis

Cancer is one of the leading causes of death in both economically developed and developing countries [146]. This makes early diagnosis of the disease and its effective treatment of paramount importance [147]. Semiconductor nanocrystals are emerging as luminescent labels for cellular imaging. Lee and Lee have reported the successful use of bioconjugated CdTe/CdSe for

labeling human breast cancer cells SK-BR3 [148]. The QDs were first biofunctionalized with herceptin monoclonal antibody that binds to the extracellular epitope of HER-2 receptors overexpressed by breast cancer cells. In 2006, Cai *et al.* [149] demonstrated for the first time that arginine-glycine-aspartic acid (RGD) peptide-conjugated QDs specifically target integrin $\alpha_v\beta_3$ *in vitro*, *ex vivo* and *in vivo*. For the *in vivo* work, athymic nude mice bearing subcutaneous U87MG human glioblastoma tumors were used. Prasad and co-workers have imaged pancreatic cancer cells using InP/ZnS nanocrystals bioconjugated with cancer specific monoclonal antibodies anticlaudin 4 and anti-prostate stem cell antigen (anti-PSCA) [66]. This group has also carried out *in vivo* targeted cancer imaging in mice using micelle encapsulated Si QDs decorated with RGD peptides that target $\alpha_v\beta_3$ integrins in the tumors [150].Weng *et al.* [151] adopted a multimodal strategy in which they used antibody- and immunoliposome-based QDs for targeting, drug delivery and imaging of cancer cells. They used anti-HER2 as tumor-targeting moieties, the immunoliposome as doxorubicin drug carrier and CdSe/ZnS QDs as the imaging agents for breast cancer cells (see **Figure 1.24**). These researchers conducted both in vitro (using HER2-overexpressing SK-BR3 and HER2-nonoverexpressing MCF7 cancer cell lines) and *in vivo* (using nude mice bearing MCF-7/HER2 xenografts implanted in their lower backs)

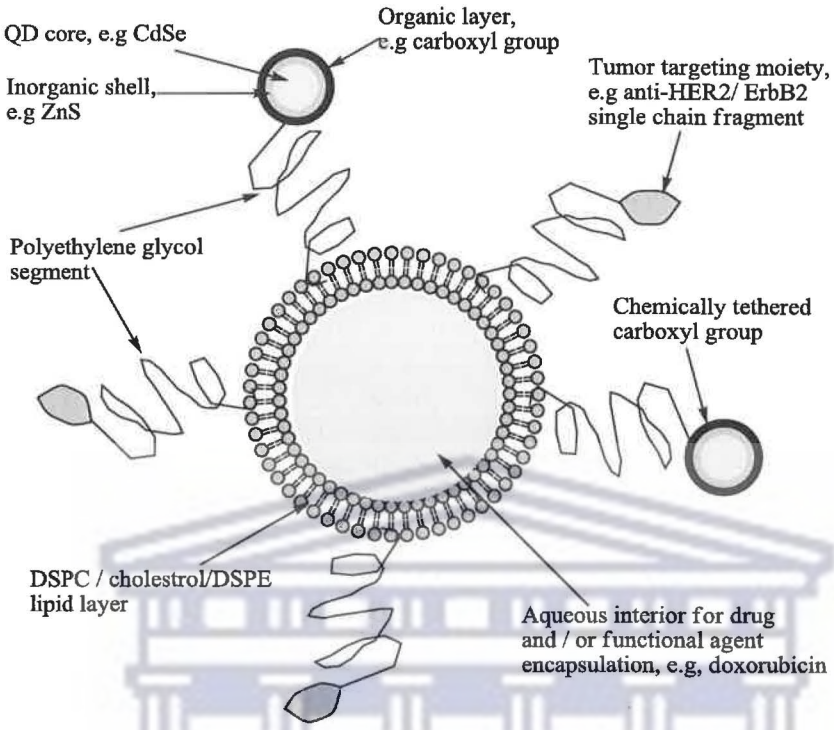

Figure 1.24 Schematic diagram showing an immunoliposome (with interior for doxorubicin loading) conjugated with QDs and anti-HER2 antibody [151].

1.9.2.2 Obesity diagnosis

Obesity is a chronic endocrine disease that occurs when energy intake chronically exceeds its expenditure culminating in the excess body fat being stored in white adipose tissue. The fat cells or adipocytes that make up the adipose tissue have been identified as being part of the endocrine system secreting several peptides such as leptin, adiponectin, tumor necrosis factor-a (TNF-a) and interleukin-6 (IL-6) [152]. Therefore treatments regimes are aimed at targeting these fat cells bearing in mind that they are an essential part of the endocrine system. There are four ways of managing obesity that are – i) having a healthy diet; ii) doing regular exercises; iii) undergoing bariatric surgery and iv) undergoing pharmacotherapy. Traditionally, use of drugs in obesity

treatments has been associated with undesired consequences resulting in their withdrawal (**Table 1.5**) [153]. Bray and Tartaglia have identified some targets for anti-obesity drugs (see **Figure 1.25**) [154].

Table 1.5 Undesired consequences from use of anti- obesity drugs [153]

Drug	**Undesired consequences**
Thyroid extract	Hyperthyroidism
Dinitrophenol	Cataracts, neuropathy
Amphetamine	Addiction
Rainbow pills	Deaths
Aminorex	Pulmonary hypertension
Collagen-based (very low calorie diet)	Deaths
Fenfluramine/phentermine	Valvular insufficiency

A nanotechnology-based strategy involving the use of nanomaterials such as QDs as drug carriers for dealing with the obesity problem would target pharmacotherapeutic methods. Dhobale *et al.* [155] have reported the use of zinc oxide nanoparticles as possible alpha-amylase inhibitors with potential applications in diabetes control. The 1-thioglycerol-capped QDs used in the work showed maximum alpha-amylase inhibition (49 %) at an inhibitor concentration of 20 µg/mL.

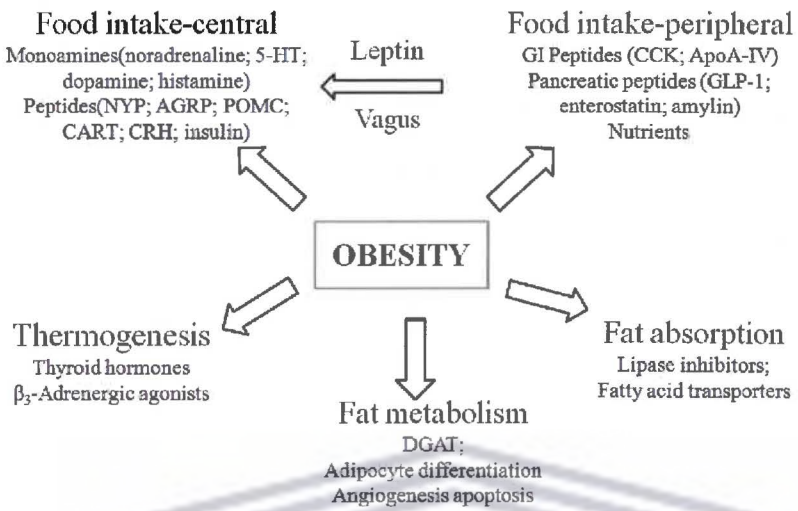

Figure 1.25 Strategies for molecules targeted against obesity [154]

1.10 Quantum dot cytotoxicity

The subject of quantum dot toxicity is very complex given the assortment of the quantum dot systems that have been and continue to be synthesized. Each quantum dot type or batch possesses its own unique physicochemical properties that have an influence on the potential toxicity or lack of it [156]. Environmental conditions such as particle size, charge, concentration, outer coating and stability (oxidative, photolytic or mechanical) have also been implicated to influence QD toxicity [134].

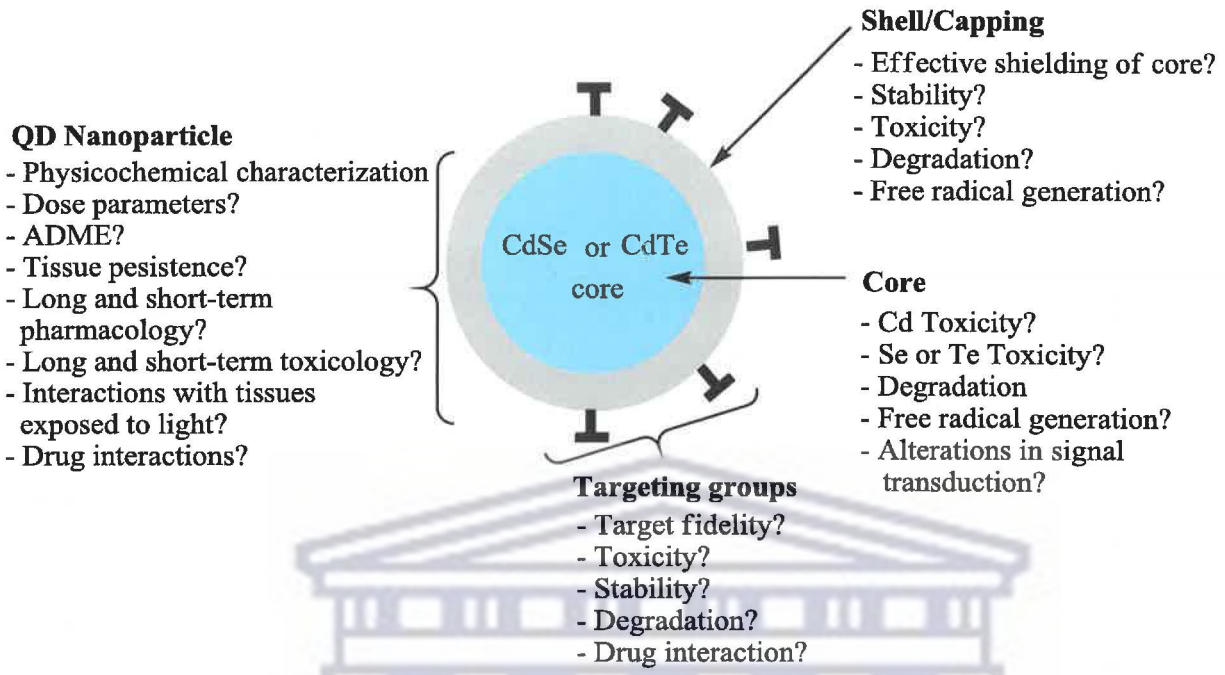

Figure 1.26 Components of a representative cadmium-containing QD that must be considered on the pharmacology and toxicology of QDs [157].

The discussion on the nanotoxicity of these QDs will be divided into three sections (as illustrated in **Figure 1.26**); toxicity of the core, shell or capping groups.

The bulk of biomedical studies using QDs has relied heavily on the group II-VI systems which are cadmium-based, mainly CdSe or CdTe systems. Cytotoxicity of these QDs is based on the properties of the components. Derfus *et al.* [64] reported a marked increase in hepatotoxicity with increasing oxidation time, of CdSe QDs incubated with rat hepatocytes. This was attributed to the degradation of the QD core according to the following mechanism (**Scheme 1.1**).

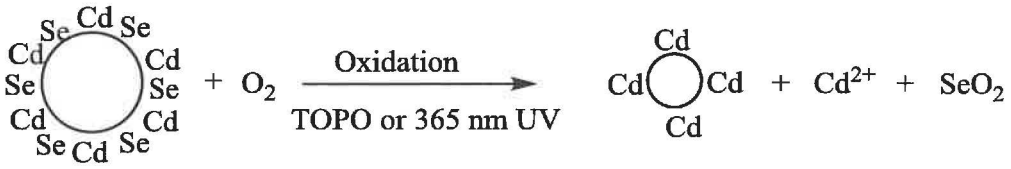

Scheme 1.4 Proposed mechanism of Cd^{2+} release from the QD surface via UV-catalyzed or TOPO-mediated surface oxidation [64].

Unmodified QDs have also been implicated in the generation of reactive oxygen species (ROS). Maysinger and her group reported that unmodified CdTe QDs induced the formation of ROS leading to multiple organelle damage and cell death [158]. **Scheme 1.2** shows the mechanism of QD cytotoxicity via the possible formation of ROS.

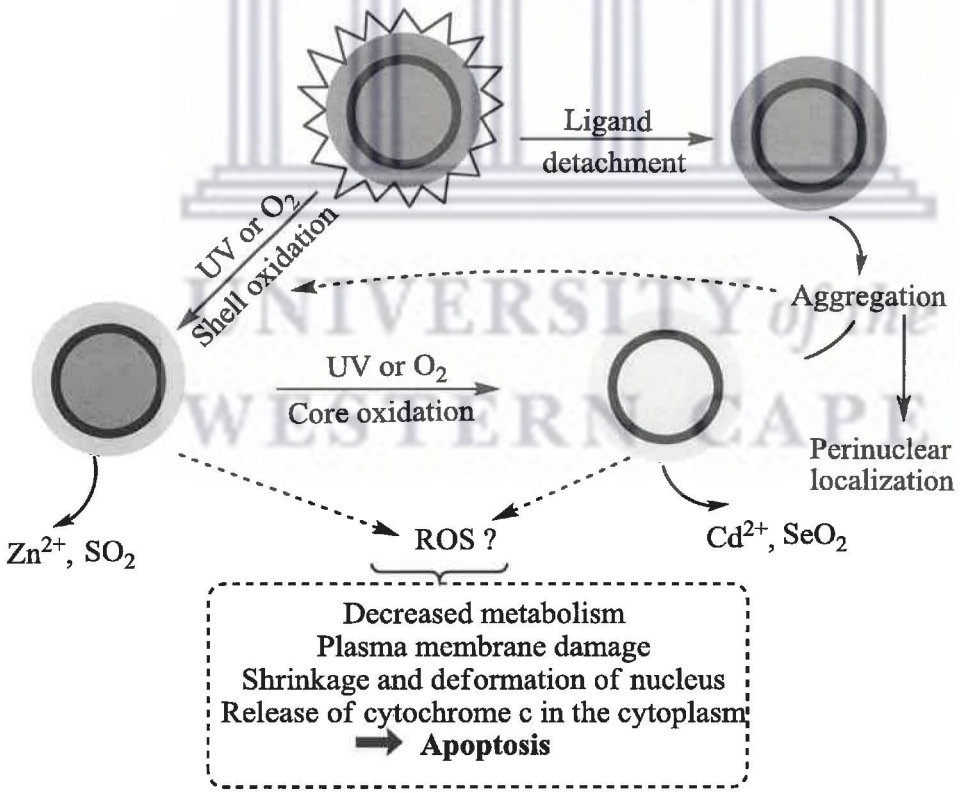

Scheme 1.5 Mechanism of QD cytotoxicity via the possible formation of ROS [158].

The introduction of an inorganic shell around the QD core has been used as a way to reduce toxicity of QDs emanating from the core [159]. This is a result of the improvement in the stability of the nanocrystals after overcoating the cores with inorganic shell (as discussed in **Section 1.2.2**).

1.11 Motivation for the study

As mentioned in **Section 1.8**, fluorescent QDs have found application as optical probes to target and image fundamental events that occur within biological systems. Important in this regard are QDs with emission profiles within the near-infrared window (600-900 nm). In this diagnostic window, absorption by tissues is minimal [160-162]. Cadmium-based QDs have been the most commonly used systems for *in vivo* studies. In 1998, Chan and Nie [100] and Bruchez *et al.* [106] pioneered the use of bioconjugated CdSe/ZnS in cellular imaging. Ballou *et al.* [163] reported that coating CdSe/ZnS QDs with amphiphilic poly(acrylic acid) polymer enhanced their circulation time as well as reduced non-specific deposition *in vivo*. They reported that PEGylation of the semiconductor nanocrystals prolonged their serum lifetime and aided in targeting. Gao *et al.* [111] reported that linking QDs to bioaffinity ligands such monoclonal antibodies, peptides oligonucleotides aids in binding specificity. They further reported that *in vivo* toxicity is a key factor in determining whether or not QD-based imaging probes would receive approval by regulatory agencies for human clinical use. Thus, the development of non-cadmium-based QDs would be of great importance in advancing their use in human clinical applications such as *in vivo* imaging.

The aim of the project is therefore to fabricate less toxic near-infrared emitting QDs that are to be used as diagnostic tools for *in vivo* imaging studies. The specific objectives are:

- To synthesize indium phosphide quantum dots overcoated with a ZnSe shell.
- To synthesize transition metal- doped InP/ZnSe QDs and investigate the effects of the dopants on the emission profile of the InP/ZnSe quantum dot systems.
- To characterize the as-prepared QDs using PL, HRTEM and XRD techniques.
- To carry out ligand exchange reactions in order to render the QDs water compatible.
- To carry out cytotoxicity studies of InP/ZnSe QDs
- To carry out cellular internalization studies of TAT-conjugated InP/ZnSe QDs

1.12 References

1 Henglein A, *Chem. Rev.*, **1989**, *89, 1861*

2 Talapin DV, Rogach AL, Shevchenko EV, Kornowski A, Haase M, Weller H, *J. Am. Chem. Soc.*, **2002**, *124, 5782*

3 Bera D, Qian L, Tseng T-K, Holloway PH, *Materials*, **2010**, *3, 2260*

4 Chan WCW, Maxwell DJ, Gao X, Bailey RE, Han M, Nie S, *Curr. Opin. Biotechnol.*, **2002**, *13, 40*

5 Vashit SK, Tewari R, Bajpai RP, Bharadwaj LM, Rateri R, *J. Nanotechnol.*, **2006**, *2, 1*

6 Andersen KE, Fong CY, Picket WE, *J. Non-Cryst. Solids*, **2002**, *299-302, 1105*

7 Sharma SN, Kholi S, Rastogi, *Physica E*, **2002**, *25, 554*

8 Leatherdale CA, Woo WK, Mikulec FV, Bawendi MG, *J. Phys. Chem. B.*, **2002**, *106, 7619*

9 Dabbousi BO, Rodriguez-Viejo J, Mikulec FV, Heine JR, Mattoussi H, Ober R, Jensen KF, Bawendi MG, *J. Phys. Chem. B.*, **1997**, *101, 9463*

10 Alivisatos AP, *Science*, **1996**, *271, 933*

11 Lee K-H, *J. Nucl. Med.*, **2007**, *48, 1408*

12 Klimov VI, *Los Alamos Sci.*, **2003**, *28, 214*

13 Lundstrom T, Schoenfeld W, Lee H, Petroff PM, *Science*, **1999**, *286, 2312*

14 Deng Z, Yan H, Liu Y, *J. Am. Chem. Soc.* **2009**, *131, 17744*

15 Zu L, Norris DJ, Kennedy TA, Erwin SC, Efros AL, *Nano Lett.*, **2006**, *6, 334*

16 Kim J-U, KimYK, Yang H, *J. Colloid Interf. Sci.*, **2010**, *341, 59*

17 Xie P, Peng X, *J. Am. Chem. Soc.* **2009**, *131, 10645*

18 Pradhan N, Goorskey D, Thessing J, Peng X, *J. Am. Chem. Soc.* **2005**, *127, 17586*

19 Stowell CA, Wiacek RJ, Saunders AE, Korgel BA, *Nano Lett.*, **2003**, *3,1441*

20 Murugadoss A, Chattopadhyay A, *Bull. Mater. Sci.*, **2008**, *31, 533*

21 Norris DJ, Efros AL, Erwin SC, *Science*, **2008**, *319, 1776*

22 Liang D-S, Shen L, Wang Z-B, Cui Y-P, Zhang J-Y, Ye Y-H, *Chin. Phys. Lett.*, **2008**, *25, 4431*

23 Pendyala NB, Rao KSRK, *J. Lumin.*, **2008**, *128, 1826*

24 Brus L, *J. Phys. Chem.*, **1986**, *90, 2555*

25 Gong H-M, Zhou Z-K, Song H, Hao Z-H, Han J-B, Zhai Y-Y, Xiao S, Wang Q-Q, *J. Fluoresc.*, **2007**, *17, 715*

26 Talgorn E, Abellon RD, Kooyman PJ, Piris J, Savenije TJ, Goossens A, Houtepen AJ, Siebbeles LDA, *ACS Nano*, **2010**, *4, 1723*

27 Peng X, Wickham J, Alivisatos AP, *J. Am. Chem. Soc.*, **1998**, *120, 5343*

28 Yu WW, Peng X, *Angew. Chem. Int. Edit.*, **2002**, *41, 2368*

29 Peng ZA, Peng X, *J. Am. Chem. Soc.*, **2001**, *123, 1389*

30 Manna L, Scher EC, Alivisatos AP, *J. Clust. Sci.*, **2002**, *13, 521*

31 Cao YW, Banin U, *J. Am. Chem. Soc.*, **2000**, *122, 9692*

32 Kuno M, Lee JK, Dabbousi BO, Mikuec FV, Bawendi MG, *J. Chem. Phys.*, **1997**, *106, 9869*

33 Peng X, Schlamp MC, Kadavanich AV, Alivisatos AP, *J. Am. Chem. Soc.*, **1997**, *119, 7019*

34 Lee JRI, Whitley HD, Meulenberg RW, Wolcott A, Zhang JZ, Prendergast D, Lovingood DD, Strouse GF, Ogitsu T, Schwegler E, Terminello LJ, Van Buuren T, *Nano Lett.*, **2012**, *12, 2763*

35 Yang H, Santra S, Holloway PH, *J. Nanosci. Nanotech.*, **2005**, *5, 1364*

36 Hines MA, Guyot-Sionnst PJ, *J. Phys. Chem.*, **1996**, *100,46*

37 Kim S, Park J, Kim T, Jang E, Jun S, Jang H, Kim B, Kim S-W, *Small* **2011**, *7, 70*

38 Reiss P, Protiere M, Li L, *Small* **2009**, *5, 154*

39 Wang S, Jarrett BR, Kauzlarich SM, Louie AY, *J. Am. Chem. Soc.*, **2007**, *129, 3848*

40 Hwang C-S, *J. Nano Bio Tech*, **2006**, *3, 66*

41 Fang Z, Li Y, Zhang H, Zhong X, Zhu L, *J. Phys. Chem. C*, **2009**, *113, 14145*

42 Stoehr M, Maurin M, Hamdani F, Lascaray JP, Barbusse D, Fraisse B, , R. Fourcade, Abraham P, Monteil Y, *Mater. Sci. Eng. B,* **1993**, *21, 257*

43 Huang K, Huang K, Demadrille R, Silly MG, Sirotti F, Reiss P, Renault O, *ACS Nano,* **2010**, *4, 4799*

44 Reiss P, *New J. Chem.,* **2007**, *31, 1843*

45 Murray CB, Norris DJ, Bawendi MG, *J. Am. Chem. Soc.,* **1993**, *115, 8706*

46 Murray CB, Sun S, Gaschler W, Doyle H, Betley TA, Kagan CR, *IBM J. Res. Dev.,* **2001**, *45, 47*

47 Kwon SG, Piao Y, Park J, Angappane S, Jo Y, Hwang N-M, Park J-G, Hyeon Y, *J. Am. Chem. Soc.,* **2007**, *129, 12571*

48 Li L, Reiss P, *J. Am. Chem. Soc.,***2008**, *130, 11588*

49 Li L, Daou TJ, Texier I, Chi TTK, Liem NQ, Reiss P, *Chem. Mater.,* **2009**, *21, 2422*

50 Lee EJH, Ribeiro C, Longo E, Leite ER, *Chem. Phys.,* **2006**, *328, 229*

51 Manna L, Scher EC, Alivisatos AP, *J. Am. Chem. Soc.,* **2000**, *122, 12700*

52 Yin Y, Alivisatos AP, *Nature,* **2005**, *437, 664*

53 Park J, Joo J, Kwon SG, Jang Y, Hyeon T, *Angew. Chem. Int. Ed.,* **2007**, *46, 4630*

54 Schladt TD, Schneider K, Schild H, Tremel W, *Dalton Trans.,* **2011**, *40, 6315*

55 Su H, Dixon JD, Wang AY, Low J, Xu J, Wang J, *Nanoscale Res. Lett.,* **2010**, *5, 823*

56 Wong EM, Hoertz PG, Liang CJ, Shi B-M, Meyer GJ, Searson PC, *Langmuir,* **2001**, *17, 8362*

57 Burda C, Chen X, Narayanan R, El-Sayed MA, *Chem. Rev.,* **2005**, *105, 1025*

58 Smith AM, Dave S, Nie S, True L, Gao X, *Expert Rev. Mol. Diagn.,* **2006**, *6, 231*

59 Klimov VI, *Annu. Rev. Phys. Chem.,* **2007**, *58, 635*

60 Artemyev MV, Woggon U, Jaschinski H, Langbein W, *Nano Lett.,* **2001**, *1, 309*

61 Gaponik NP, Talapin DV, Rogach AL, EychmuÈller A, *J. Mater. Chem.,* **2000**, *10, 2163*

62 Bruchez M Jr., Moronne M, Gin P, Weiss S, Alivisatos AP, *Science,* **2016**, *281, 2013*

63 Michalet X, Pinaud FF, Bentolila LA, Tsay JM, Doose S, Li JJ, Sundaresan G, Wu AM, Gambhir SS, Weiss S, *Science,* **2005**, *307, 538*

64 Derfus M, Chan WCW, Bhatia SN, *Nano Lett.,* **2004**, *4, 11*

65 Bharali DJ, D. Lucey W, Jayakumar H, Pudavar HE, Prasad PN, *J. Am. Chem. Soc.,* **2005**, *127, 11364*

66 Yong K-T, Ding H, Roy I, Law W-C, Bergey EJ, Maitra A, Prasad PN, *ACS Nano,* **2009**, *3, 502*

67 Langof L, Ehrenfreund E, Lifshitz E, Micic OI, Nozik AJ, *J. Phys. Chem. B,* **2002**, *106, 1606*

68 Byun H-J, Lee JC, Yang H, *J. Colloid Interf. Sci.,* **2011**, *355, 35*

69 Puangmali T, Califano M, Harrison P, *J. Phys. Chem. C,* **2010**, *114, 6901*

70 Yadav RS, Mishra P, Mishra R, Kumar M, Pandey AC, *Ultrason. Sonochem.,* **2010**, *17, 116*

71 Kyhm K, Kim JH, Kim SM, Yang H-S, *Opt. Mater.,* **2007**, *30, 158*

72 Rajh T, Micic OI, Nozik AJ, *J. Phys. Chem.,* **1993**, *97, 11999*

73 Ramanathan S, Patibandla S, Bandyopadhyay S, Anderson J, Edwards JD, *Nanotechnology,* **2008**, *19, 195601.1*

74 Micic OI, Curtis CJ, Jones KM, Spargue JR, Nozik AJ, *J. Phys. Chem.,* **1994**, *98, 4966*

75 Micic OI, Nozik AJ, *J. Lumin.,* **1996**, *70, 95*

76 Talapin DV, Gaponik N, Borchert H, Rogach AL, Haase M, Weller H, *J. Phys. Chem. B,* **2002**, *106, 12659*

77 Micic OI, Smith BB, Nozik AJ, *J. Phys. Chem. B,* **2000**, *104, 12149*

78 Kim S, Park J, Kim S, Jung W, Sung J, Kim S-W, *J. Colloid Interf. Sci.,* **2010**, *346, 347*

79 Ryu E, Kim S, Jang E, Jun S, Jang H, Kim B, Kim S-W, *Chem. Mater.,* **2009**, *21, 573*

80 Li L, Protiere M, Reiss P, *Chem. Mater.,* **2008**, *20, 2621*

81 Thuy PT, Thuy UTD, Chi TTK, Phuong LQ, Liem NQ, Li L, Reiss P, *J. Phys. Conf. Ser.,* **2009**, *187, 012014*

82 Battaglia D, Peng X, *Nano Lett.*, **2002**, *2, 1027*

83 Narayanaswamy A, Feiner LF, Van der Zaag PJ, *J. Phys. Chem. C*, **2008**, *112, 6775*

84 Lucey DW, MacRae DJ, Furis M, Sahoo Y, Cartwright AN, Prasad PN, *Chem. Mater.*, **2005**, *17, 3754*

85 Xu S, Kumar S, Nann T, *J. Am. Chem. Soc.*, **2006**, *128, 1054*

86 Hussain S, Won N, Nam J, Bang J, Chung H, Kim S, *ChemPhysChem.* **2009**, *10, 1466*

87 Micic OI, Ahrenkiel SP, Nozik AJ, *Appl. Phys. Lett.*, **2001**, *78, 4022*

88 Portiere M, Reiss P, *Chem. Commun.*, **2007**, *23, 2417*

89 Allen PM, Walker BJ, Bawendi MG, *Angew. Chem. Int. Edit.*, **2010**, *49, 760*

90 Li C, Ando M, Enomoto H, Murase N, *J. Phys. Chem. C*, **2008**, *112, 20190*

91 Gao S, Lu J, Chen N, Zhao Y, Xie Y, *Chem. Commun.*, **2002**, *3064*

92 Green M, O'Brien P, *Chem. Commun.*, **1998**, *2459*

93 Liu Z, Kumbhar A, Xu D, Zhang J, Sun Z, Fang J, *Angew. Chem. Int. Edit.*, **2008**, *47, 3540*

94 Kim S-W, Zimmer JP, Ohnishi S, Tracy JB, Frangioni JV, Bawendi MG, *J. Am. Chem. Soc.*, **2005**, *127, 10526*

95 Gerbec JA, Magana D, Washington A, Strouse GF, *J. Am. Chem. Soc.*, **2005**, *127, 15791*

96 Somaskandan K, Tsoi GM, Wenger LE, Brock SL, *Chem. Mater.*, **2005**, *17,1190*

97 Mocatta D, Cohen G, Schattner J, Millo O, Rabani E, Banin U, *Science*, **2011**, *332, 77*

98 Sahoo Y, Poddar P, Srikanth H, Lucey DW, Prasad PN, *J. Phys. Chem. B*, **2005**, *109, 15221*

99 Xie R, Peng X, *J. Am. Chem. Soc.*, **2009**, *131, 10645*

100 Chu VH, Nghiem THL, Le TH, Vu DL, Tran HN, Vu TKL, *Adv. Nat. Sci. Nanosci. Nanotechnol.*, **2012**, *3, 025017*

101 Pinaud F, Michalet X, Bentolila LA, Tsay JM, Doose S, Li JJ, Iyer G, Weiss S, *Biomaterials*, **2006**, *27, 1679*

102 Sutherland AJ, *Curr. Opin. Solid. Mater. Sci.*, **2002**, *6, 365*

103 Chan WCW, Nie S, *Science,* **1998**, *281, 2016*

104 Mattoussi H, Mauro JM, Goldman ER, Anderson GP, Sundra VC, Mikulee FV, Bawendi MG, *J. Am. Chem. Soc.,* **2000**, *122, 12142*

105 Oswaldowski S, Zawistowska-Gibula K, Roberts KP, *Cent. Eur. J. Chem.,* **2011**, *9, 572*

106 Bruchez M Jr., Moronne M, Gin P, Weiss S, Alivisatos AP, *Science,* **1998**, *281, 2013*

107 Mulder WJM, Strijkers GJ, Nicolay K, Griffioen AW, *Angiogenesis,* **2010**, *13, 131*

108 Pellegrino T, Manna L, Kudera S, Liedl T, Koktysh D, Rogach AL, Keller S, Radler J, Natile G, Parak WJ, *Nano Lett.,* **2004**, *4, 703*

109 Mattheakis LC, Dias JM, Choi Y-J, Gong J, Bruchez MP, Liu J, Wang E, *Anal. Biochem.,* **2004**, *327, 200*

110 Nida DL, Nitin N, Yu WW, Colvin VL, Richards-Kortum R, *Nanotechnology,* **2008**, *19, 035701*

111 Gao X, Yang L, Petros JA, Marshall FF, Simons JW, Nie S, *Curr. Opin. Biotechnol.,* **2005**,*16, 63*

112 Luccardini C, Tribet C, Vial F, Marchi-Artzner V, Dahan M, *Langmuir,* **2006**, *22,* 2304

113 Gao X, Cui Y, Levenson RM, Chung LWK, Nie S, 1, *Nature Biotechnol.,* **2004**, *22, 969*

114 Pellegrino T, Manna L, Kudera S, Liedl T, Koktysh D, Rogach AL, Keller S, Radler J, Natile G, Parak WJ, *Nano Lett.,* **2004**, *4, 703*

115 Tomczaka N, Jan´czewski D, Hana M, Vancso GJ, *Prog. Polym. Sci.,* **2009**, *34, 393*

116 Darbandi M, Thomann R, Nann T, *Chem. Mater.,* **2005**, *17, 5720*

117 Parak WJ, Gerion D, Zanchet D, Woerz AS, Pellegrino T, Micheel C, Williams SC, Seitz M, Bruehl RE, Bryant Z, Bustamante C, Bertozzi CR, Alivisatos AP, *Chem. Mater.,* **2002**, *14, 2113*

118 Sapsford KE, Pons T, Medintz IL, Mattoussi H, *Sensors,* **2006**, *925*

119 Dennis AM, Sotto DC, Mei BC, Medintz IL, Mattoussi H, Bao G, *Bioconjugate Chem.* **2010**, *21, 1160*

120 Pinaud F, King D, Moore H-P, Weiss S, *J. Am. Chem. Soc.,* **2004**, *126, 6115*

121 Wu X, Liu H, Liu J, Haley KN, Treadway JA, Larson JP, Ge N, Peale F, Bruchez MP, *Nat. Biotechnol.*, **2003**, *21, 41*

122 Erogbogbo F, Tien C-A, Chang C-W, Yong K-T, Law W-C, Ding H, Roy I, Swihart MT, Prasad PN, *Bioconjugate Chem.*, **2011**, *22, 1081*

123 Dubertret B, Skourides P, Norris DJ, Noireaux V, Brivanlou AH, Libchaber A, *Science* **2002**, *298, 1759*

124 East DA, Mulvihill DP, Todd M, Bruce IJ, *Langmuir*, **2011**, *27, 13888*

125 Boeneman K, Delehanty JB, Susumu K, Stewart MH, Igor L. Medintz IL, *J. Am. Chem. Soc.*, **2010**, *132, 5975*

126 Liu W, Howarth M, Greytak AB, Zheng Y, Nocera DG, Ting AY, Bawendi MG, *J. Am. Chem. Soc.*, **2008**, *130, 1274*

127 Mattoussi H, Mauro JM, Goldman ER, Green TM, Anderson GP, Sundar VC, Bawendi MG, *Phys. Stat. Sol. B*, **2001**, *224, 277*

128 Goldman ER, Medintz IL, Mattoussi H, *Anal. Bioanal. Chem.*, **2006**, *384, 560*

129 Goldman ER, Balighian ED, Mattoussi H, Kuno MK, Mauro JM, Tran PT, Anderson GP, *J. Am. Chem. Soc.*, **2002**, *124, 6378*

130 Medintz IL, Uyeda HT, Goldman ER, Mattoussi H, *Nature Mater.*, **2005**, *4, 435*

131 Parak WJ, Gerion D, Pellegrino T, Zanchet D, Micheel C, Williams SC, Boudreau R, Gros MAL, Larabell CA, Alivisatos AP, *Nanotechnology*, **2003**, *14, R15*

132 Salata OV, *J. Nanobiotechnol.*, **2004**, *2, 3*

133 Mazumder S, Dey R, Mitra MK, Mukherjee S, Das GC, *J. Nanomater.*, **2009**, *2009, 815734*

134 Jin S, Hu Y, Gu Z, Liu L, Wu H-C, *J. Nanomater.*, **2011**, *2011, 834139*

135 Rosenthal SJ, Chang JC, Kovtun O, McBride JR, Tomlinson ID, *Chem. Biol.*, **2011**, *18, 10*

136 Smith AM, Duan H, Mohs AM, Nie S, *Adv. Drug Deliver. Rev.*, **2008**, *60 1226*

137 Haley B, Frenkel E, *Urol. Oncol.-Semin. Ori.*, **2008**, *26, 57*

138 Danhier F, Feron O, Préat V, *J. Control. Release*, **2010**, *148, 135*

139 Iyer AK, Khaled G, Fang J, Maeda H, *Drug Discov. Today*, **2006**, *11, 812*

140 Heldin CH, Rubin K, Pietras K, Ostman A, *Nat. Rev. Cancer,* **2004**, *4, 806*

141 Bae HY, *J. Control. Release,* **2009**, *133, 2*

142 Prabhu V, Uzzaman S, Grace VMB, Guruvayoorappan C, *J. Can. Ther.*, **2011**, *2, 325*

143 Byrne JD, Betancourt T, Brannon-Peppas L, *Adv. Drug Deliver. Rev.*, **2008**, *60, 1615*

144 Heitz F, Morris MC, Divita G, *Brit. J. Pharmacol.*, **2009**, *157, 195*

145 Akerman ME, Chan WCW, Laakkonen P, Bhatia SN, Ruoslahti E, *Proc. Natl. Acad. Sci. USA,* **2002**, *99, 12617*

146 Jemal A, Bray F, Center MM, Ferlay J, Ward E, Forman D, *CA Cancer J. Clin.*, **2011**, *61, 69*

147 Mols F, Thong MSY, Vissers P, Nijsten T, van de Poll-Franse LV, *Eur J Cancer,* **2012**, *48, 2037*

148 Lee DK, Lee Y-K, *Macromol. Res.*, **2010**, *18, 641*

149 Cai W, Shin D-W, Chen K, Gheysens O, Cao Q, Wang SX, Gambhir SS, Chen X, *Nano Lett.*, **2006**, *6, 669*

150 Erogbogbo F, Yong K-T, Roy I, Hu R, Law W-C, Zhao W, Ding H, Wu F, Kumar R, Swihart MT, Prasad PN, *ACS Nano,* **2011**, *5, 413*

151 Weng KC, Noble CO, Papahadjopoulos-Sternberg B, Chen FF, Drummond DC, Kirpotin DB, Wang D, Hom YK, Hann B, Park JW, *Nano Lett.*, **2008**, *8, 2851*

152 Kokkoris P, Pi-Sunyer FX, *Endocrinol. Metab. Clin. N. Am.*, **2003**, *32, 895*

153 Bray GA, Greenway FL, *Endocr. Rev.*, **1999**, *20, 805*

154 Bray GA, Tartaglia LA, *Nature,* **2000**, *404, 672*

155 Dhobale S, Thite T, Laware SL, Rode CV, Koppikar SJ, Ghanekar R-K, Kale SN, *J. Appl. Phys.*, **2008**, *104, 09490*

156 Male KB, Lachance B, Hrapovic S, Sunahara G, Luong JHT, *Anal. Chem.*, **2008**, *80, 5487*

157 Rzigalinski BA, Strobl JS, *Toxicol. Appl. Pharm.*, **2009**. *238, 280*

158 Lovri J, Cho SJ, Winnik FM, Maysinger D, *Chem. Biol.*, **2005**, *12, 1227*

159 Su Y, He Y, Lu H, Sai L, Li Q, Li W, Wang L, Shen P, Huang Q, Fan C, *Biomaterials,* **2009**, *30, 19*

160 Kim S-W, Zimmer JP, Ohnishi S, Tracy JB, Frangioni JV, Bawendi MG, *J. Am. Chem. Soc.*, **2005**, *127, 10526*

161 Weisslder R, *Nat. Biotechnol.*, **2001**, *22, 316*

162 Gao J, Xu B, *Nano Today,* **2009**, *4, 37*

163 Ballou B, Lagerholm BC, Ernst LA, Bruchez MP, Waggoner AS, *Bioconjugate Chem.*, **2004**, *15, 79*

CHAPTER 2: EXPERIMENTAL

2.1 General Experimental Details

All reagents were of analytical grade and were used as received. Indium acetate ($In(OAc)_3$), palmitic acid, zinc undecylenate, zinc acetate, silver nitrate, selenium powder, tellurium powder, sodium borohydride, trioctylphosphine (TOP), 1-octadecene (ODE, 90 %), tetramethylammonium hydroxide pentahydrate (TMAH), N-hydroxysuccinimide and (NHS), 1-ethyl-3-(dimethylaminopropyl)carbodiimide hydrochloride (EDC), polyethylene glycol (PEG), 3-mercaptopropionic acid (MPA), thiourea and tris(trimethylsilyl)phosphine ($P(TMS)_3$, 95 %) were purchased from Sigma Aldrich. Sodium hydroxide, cobalt(II) chloride hexahydrate, iron(II) chloride tetrahydrate were purchased from Saarchem. The solvents used: methanol, acetone, 2-isopropanol, hexane chloroform were also purchased from Sigma Aldrich. For cell culture work, Dulbecco's modified Eagle's medium (DMEM) (Gibco), dimethyl sulfoxide (DMSO) (Sigma), paraformaldehyde (Sigma), 4,6-diaminidino-2-phenylindole dihydrochloride (DAPI) (Sigma), foetal bovine serum (Invitrogen), phosphate buffered saline (PBS) (Invitrogen), trypsin (Invitrogen) and antibiotics (penicillin–streptomycin, 1 µg/mL of culture medium) (Invitrogen) were used.

2.2 Instrumentation

Various instruments were used in the characterization of the nanocrystals fabricated in this project. Characterization techniques used include photoluminescence spectroscopy, transmission electron microscopy and X-ray diffraction, which are described below.

2.2.1 Photoluminescence spectroscopy

As stated in Chapter 1, the process of fluorescence is defined as the spontaneous emission of radiation from an excited fluorophore with the formation of a fluorophore of the same spin multiplicity, according to the IUPAC glossary of terms [1].

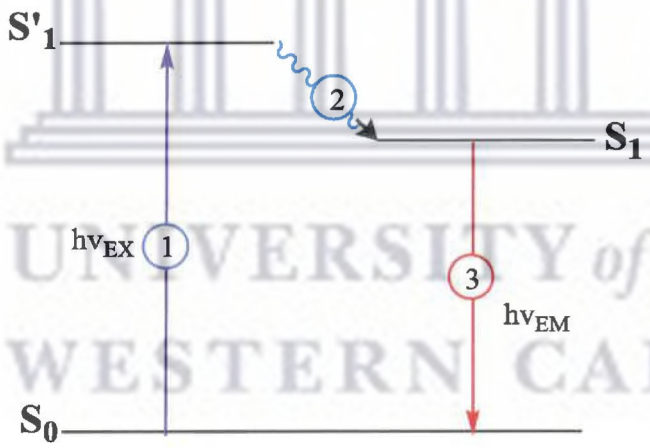

Figure 2.1 The Jablonski diagram illustrating the fluorescence process [2]

Photoluminescence (PL) spectra were recorded on a HORIBA Nanolog FL3-22-TRIAX. The schematic diagram of the Nanolog system configuration is shown in **Figure 2.2.** The light source for the instrument was a 450 W Xenon arc lamp while the signal detector was a standard R928 photomultiplier tube (PMT) with a detection range spanning 200 – 850 nm.

The photoluminescence quantum yield (QY) for the InP/ZnSe NCs was determined using Rhodamine 6G as a standard according to a published procedure [3]. The optical densities of all the solutions were adjusted to values below 0.05 at the excitation wavelength of 400 nm to avoid re-absorption effects. The absorbances for the standard in ethanol and the InP/ZnSe in hexane at this excitation wavelength and the photoluminescence spectra of the same solutions were measured respectively. The integrated fluorescence intensity from the corrected spectrum was calculated.

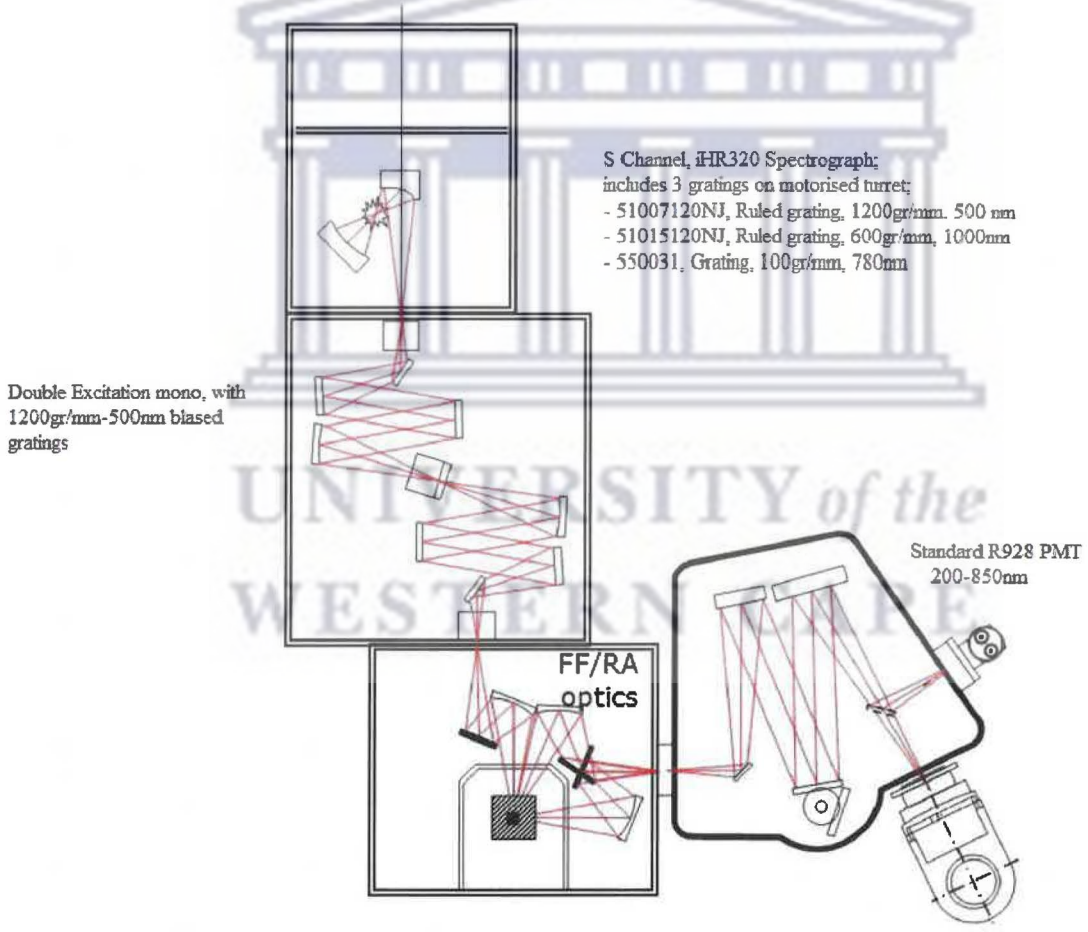

Figure 2.2 Schematic diagram of a HORIBA Nanolog FL3-22-TRIAX system configuration [4].

2.2.2 Transmission electron microscopy (TEM)

TEM studies were performed on a Field Emission TECNAI F20 TEM. Samples for TEM studies were prepared by placing a hexane solution of the nanocrystals on ultrathin carbon-film-coated copper grids and allowed to dry at room temperature. In order to image and analyze the microstructure of nanomaterials with atomic scale resolution, a high energy electron beam was transmitted through the very thin sample on the grid. The electrons were focused with electromagnetic lenses and the image was observed on a fluorescent screen. For the high resolution imaging mode, the microscope imaged the crystal lattice of the nanomaterial as an interference pattern between the transmitted and diffracted beams, allowing the observation of planar and line defects, grain boundaries and interfaces with atomic scale resolution.

2.2.3 XRD

X-ray diffraction was used to determine the crystallinity of the indium phosphide-based nanocrystals. The X-ray diffraction experiments were carried out at iThemba Labs, Cape Town using a Bruker AXS D8 Advanced Diffractometer equipped with a CuKα (λ = 1.5418 Å) X-ray source. X-ray diffraction is premised on the fact that the diffraction patterns are characteristic of both the crystal form and spacing of the chemical compounds and not their constituent elements or chemical groups [5]. Therefore, when a beam of monochromatic X-rays strikes on the planes of atoms in a given crystal, interference occurs and the X-ray beams are diffracted from the crystal in specific directions. Bragg's law gives the relationship between the wavelength of the X-rays (λ), the incident angel of the X-rays (θ), and the interatomic distance (d):

$$n\lambda = 2d\sin\theta$$

where n = the order of diffraction with values of n = 1,2,3…etc. The data are collected in the (θ - 2θ) geometry. In this work, samples for XRD analysis were prepared on a glass substrate.

2.3 Experimental details

2.3.1 Preparation of precursors used in QD fabrication

2.3.1.1 Preparation of Phosphorus precursor solution

Generally the phosphorus precursor injection solutions were freshly prepared in the glove box by transferring the appropriate volume of $P(TMS)_3$ into sample vials containing TOP (0.5 mL) using a micropipette. The vials were then sealed with rubber septa and transferred to the reaction fume hood ready for injection into the reaction.

2.3.1.2 Preparation of TOPSe

The general procedure for the preparation of TOPSe was adapted from literature with some modifications [6]. The selenium injection solution TOPSe (0.1 M) was prepared by dissolving selenium powder in a mixture of ODE (9 mL) and TOP (1 mL) at 140 °C. A clear solution was obtained which was used in subsequent reactions.

2.3.1.3 Preparation of zinc undecylenate solution

The zinc precursor solution (0.1 M) was prepared following a published method with modifications [6]. Zinc undecylenate (0.432 g, 0.001mol) was dissolved in a mixture of ODE (9 mL) and TOP (1 mL) at 140 °C. A clear solution was produced and stored at room temperature.

2.3.1.4 Preparation of silver(I) palmitate

A procedure by Uznanski and Bryszewska [7] was adopted for the synthesis of silver palmitate. Palmitic acid (5.12 g, 0.02 mol) and deionized water (200 mL) were added to a two-necked flask and heated at 80 °C with stirring. NaOH (0.72 g, 0.018 mol) in water (4 mL) was added giving a clear solution. $AgNO_3$ (3.058 g, 0.018 mol) in water (25 mL) was then added precipitating silver palmitate as a white product. The product was dried at 60 °C overnight.

2.3.1.5 Preparation of cobalt(II) palmitate

Cobalt(II) palmitate was synthesized following a procedure by Acharya and Pradhan with some modifications [8]. Palmitic acid (5.128 g, 0.02 mol), was added to methanol (20 mL) in a two-necked round bottomed flask and heated to 60 °C to obtain a clear solution. Tetramethylammonium hydroxide pentahydrate (3.625 g, 0.02 mol) was dissolved separately in methanol (10 mL) and transferred into a dropping funnel. The resulting solution was then added drop wise to palmitic acid solution with stirring over 20 min to complete the reaction. $CoCl_2.6H_2O$ (2.379 g, 0.01 mol) was dissolved in methanol (10 mL) and again added drop wise

to the above solution with vigorous stirring. A faint pink product, cobalt(II) palmitate was obtained, filtered, washed with methanol (3 x 10 mL) and dried under vacuum.

2.3.1.6 Preparation of iron(II) palmitate

Iron(II) palmitate was synthesized following the same procedure as in **Section 2.3.1.4** with some modifications. Iron(II) chloride tetrahydrate (4.012g, 0.02 mol)) was dissolved in methanol (100 mL) Palmitic acid (10.313g, 0.04 mol) and methanol (100 mL) were added to a two-necked flask, heated at 80 °C with stirring and slowly added to the above solution. NaOH (0.815 g, 0.02 mol) in water (20 mL) was added precipitating brown iron(II) palmitate. The product was filtered, washed with methanol (3 x 10 mL) and dried under vacuum.

2.3.2 Experimental details pertaining to Chapter 3

2.3.2.1 Synthesis of InP/ZnSe QDs in non-coordinating solvent 1-octadecene

The NCs were synthesized in a non-coordinating solvent 1-octadecene according to the procedure by Ryu *et al.* [9] with some modifications. In a typical synthesis, indium acetate (0.15 mmol) was mixed with palmitic acid (0.45 mmol) and ODE (4 mL) in a three-necked flask inside the glove box. The flask was sealed and transferred to a Schlenk line and heated to 120 °C and kept under vacuum for 1.5 h. The system was then purged with argon and then heated to 300 °C. On reaching 300 °C, a freshly prepared injection solution of $P(TMS)_3$ in TOP (0.075 mmol in 1 mL TOP prepared in the glove box) was injected rapidly under argon flow. For the growth of the InP core, the reaction mixture was kept at 270 °C for 2 h. After 2 h, the temperature was lowered to 150 °C. For the shelling process, the zinc injection solution (0.1 M) was prepared by

dissolving zinc undecylenate in a mixture of ODE (9.5 mL) and TOP (0.5 mL) at 140 °C. Similarly the selenium injection solution (0.1 M) was prepared by dissolving selenium in a mixture of ODE (9.5 mL) and TOP (0.5 mL) at 140 °C. The zinc precursor solution (0.375 mmol, 0.375 mL) was added and the temperature was raised to 230 °C and maintained at that temperature for 4 h. A selenium precursor solution (0.15 mmol, 1.5 mL) was injected in to the flask and kept at this temperature for 1 h. Aliquot portions were taken during core and shell growth for characterization using PL. The InP/ZnSe nanocrystals were purified from the reaction mixture by precipitation with acetone and redissolving them in hexane. HRTEM was also performed to characterize the crystallinity of the nanocrystals.

2.3.2.2 Synthesis of InP/ZnSe QDs using polyethylene glycol (PEG) as solvent

InP/ZnSe nanocrystals were synthesized using polyethylene glycol as a solvent according to a procedure by Hussain *et al.* [10] with some modifications. Indium acetate (0.4 mmol) was mixed with palmitic acid (1.6 mmol) and PEG (4 g) in a three-necked flask in the glove box. The flask was sealed, transferred to a Schlenk line and the mixture was heated to 120 °C for 1.5 h under vacuum to obtain a clear solution. The flask was then purged with argon and heated to 200 °C. A solution of freshly prepared $P(TMS)_3$ (0.2 mmol in 0.5 mL of TOP) was injected at 200 °C and the nanocrystals were allowed to grow for 1 h. A solution of zinc undecylenate (1 mL, 0.1 M) was added at 200 °C. The temperature was lowered to 180 °C and the selenium injection solution (1 mL, 0.1 M) was added after 10 min. ZnSe shell growth was allowed to proceed at 230 °C for 1 h. After completion of the reaction, the mixture was cooled to 60 °C, mixed with 3 mL of hexane and shaken in order to transfer the nanocrystals to the hexane layer. PEG became solidified and

was recovered by decanting. Aliquot samples were taken during the course of the reaction for PL characterization. HRTEM was performed to characterize the crystallinity of the nanocrystals.

2.3.2.3 Synthesis of InP/ZnSe using multiple injection method

The NCs were synthesized in a non-coordinating solvent 1-octadecene according to the concept reported by Weller and co-workers [11], with zinc undecylenate added at the start of the reaction (the ratio of In:P:Zn used was 1:0.5:0.75). In a typical synthesis, indium acetate (0.4 mmol) was mixed with palmitic acid (1.6 mmol), zinc undecylenate (0.3 mmol) and ODE (4 mL) in a three-necked flask in the glove box. The flask was sealed and transferred to a Schlenk line and heated to 120 °C and kept under vacuum for 1.5 h. The system was then purged with argon and then heated to 300 °C. On reaching 300 °C, a freshly prepared injection solution of $P(TMS)_3$ in TOP (0.2 mmol in 0.5 mL TOP prepared in the glove box) was injected rapidly under argon flow. For the growth of the InP core, the reaction mixture was kept at 270 °C for 30 min. After 30 min, the temperature was lowered to ~25 °C. Indium acetate (0.4 mmol) was added again and the reaction was degassed at 120 °C for 1 h. The temperature was then increased to 230 °C and a second injection of $P(TMS)_3$ in TOP (0.2 mmol in 0.5 mL TOP prepared in the glove box) was made. The reaction was maintained at this temperature for 1 h. Zinc undecylenate solution (1 mL, 0.1M) was added. After 10 min, TOPSe (2 mL, 0.2M) was added and the reaction was kept at 230 °C for 1 h. Aliquots were taken during core and shell growth for PL studies and the InP/ZnSe nanocrystals were purified from the reaction mixture by precipitation with acetone and redissolving them in hexane. The effect of the In^{3+}: Zn^{2+} ratio was investigated using the ratios of 1:0.4 and 1:0.75.

2.3.2.4 Synthesis of InP/ZnSe using single injection of high moles of precursors

The effect of using a single injection of high moles of the indium and phosphorus precursors was investigated with zinc undecylenate solution added at the start of the reaction (the ratio of In:P:Zn used was 1:0.5:0.4). In the synthesis, indium acetate (0.8 mmol) was mixed with palmitic acid (3.2 mmol), zinc undecylenate (0.32 mmol) and ODE (4 mL) in a three-necked flask in the glove box. The flask was sealed and transferred to a Schlenk line and heated to 120 °C and kept under vacuum for 1.5 h. The system was then purged with argon and then heated to 300 °C. On reaching 300 °C, a freshly prepared injection solution of $P(TMS)_3$ in TOP (0.4 mmol in 0.5 mL TOP prepared in the glove box) was injected rapidly under argon flow. For the growth of the InP core, the reaction mixture was kept at 270 °C for 6 h. After 6 h, zinc undecylenate solution (2 mL, 0.1 M) was added. After 10 min, TOPSe (2 mL, 0.2 M) was added and the reaction was kept at 230 °C for 2 h. Aliquot portions were taken during core and shell growth for characterization. The InP/ZnSe nanocrystals were purified from the reaction mixture by precipitation with acetone and redissolving them in hexane. The core growth time was also varied (4 and 8 h). HRTEM was also performed to characterize the crystallinity of the nanocrystals.

2.3.3 Experimental details pertaining to Chapter 4

All experiments involving the doping of InP/ZnSe nanocrystals with transition metal elements (Ag, Fe and Co) were carried out following a published method, with some modifications [12].

2.3.3.1 Synthesis of Ag:InP/ZnSe

The Ag-doped InP/ZnSe QDs were synthesized at a doping level of 5 % Ag with respect to P. In the synthesis, indium acetate (0.2 mmol) was mixed with palmitic acid (0.8 mmol) and ODE (4 mL) in a three-necked flask in the glove box. The flask was sealed and transferred to a Schlenk line and heated to 120 °C and kept under vacuum for 1.5 h. The system was then purged with argon and then heated to 300 °C. On reaching 300 °C, a freshly prepared injection solution of $P(TMS)_3$ in TOP (0.1 mmol in 0.5 mL TOP prepared in the glove box) was injected rapidly under argon flow. For the growth of the InP core, the reaction mixture was kept at around 270 °C for 1 h. The temperature was lowered to 130 °C and silver palmitate (0.5 mL, 0.01 M) was added. The temperature was raised to 210 °C for 1h to effect the doping. The temperature was then lowered to 150 °C for the addition of zinc and selenium precursors for the ZnSe shell. Zinc undecylenate (0.6 mL, 0.1 M) and TOPSe (0.6 mL, 0.1 M) were added with a 10 min interval between the two injections. The temperature was raised to 230 °C for 1 h. The temperature was again lowered to 150 °C and zinc undecylenate (0.8 mL, 0.1 M) and TOPSe (0.8 mL, 0.1 M) were added with a 10 min interval between the injections. The temperature was raised to 230 °C for 1 h. The Ag dopant levels were varied as 0, 5 and 10 % with respect to moles of phosphorus. Aliquots were taken for emission profile characterization using PL. XRD and HRTEM were also performed to characterize the crystallinity, size and size distribution of the nanocrystals.

2.3.3.2 Synthesis of Co:InP/ZnSe

Co-doped InP/ZnSe QDs were synthesized at doping levels of 0, 15 and 20 % Co with respect to P. In a typical synthesis, indium acetate (0.2 mmol) was mixed with palmitic acid (0.8 mmol)

and ODE (4 mL) in a three-necked flask in the glove box. The flask was sealed and transferred to a Schlenk line and heated to 120 °C and kept under vacuum for 1.5 h. The system was then purged with argon and then heated to about 300 °C. On reaching 300 °C, a freshly prepared injection solution of $P(TMS)_3$ in TOP (0.1 mmol in 0.5 mL TOP) was injected rapidly under argon flow. For the growth of the InP core, the reaction mixture was kept at around 270 °C for 1 h. The temperature was lowered to 130 °C and cobalt(II) palmitate (1.5 mL, 0.01 M) was added. The temperature was raised to 210 °C for 1h to effect the doping. The temperature was then lowered to 150 °C for the addition of zinc and selenium precursors for the ZnSe shell. Zinc undecylenate (0.6 mL, 0.1 M) and TOPSe (0.6 mL, 0.1 M) were added with a 10 min interval between the two injections. The temperature was raised to 230 °C for 1 h. The temperature was again lowered to 150 °C and zinc undecylenate (0.8 mL, 0.1 M) and TOPSe (0.8 mL, 0.1 M) were added with a 10 min interval between the injections. The temperature was raised to 230 °C for 1 h. The Co:InP/ZnSe nanocrystals were precipitated by addition of acetone. Aliquots were taken for the emission profile characterization using PL. XRD and HRTEM were performed to characterize the crystallinity, size and size distribution of the nanocrystals.

2.3.3.3 Synthesis of Fe:InP/ZnSe

The Fe-doped InP/ZnSe nanocrystals were synthesized at doping levels of 0, 5 and 10 % Fe with respect to P. In a typical synthesis, indium acetate (0.2 mmol) was mixed with palmitic acid (0.8 mmol) and ODE (4 mL) in a three-necked flask in the glove box. The flask was sealed and transferred to a Schlenk line and heated to 120 °C and kept under vacuum for 1.5 h. The system was then purged with argon and then heated to about 300 °C. On reaching 300 °C, a freshly

prepared injection solution of $P(TMS)_3$ in TOP (0.1 mmol in 0.5 mL TOP) was injected rapidly under argon flow. For the growth of the InP core, the reaction mixture was kept at around 270 °C for 1 h. The temperature was lowered to 130 °C and iron(II) palmitate (0.5 mL, 0.01 M) was added. The temperature was raised to 210 °C for 1h to effect the doping. The temperature was then lowered to 150 °C for the addition of zinc and selenium precursors for the ZnSe shell. Zinc undecylenate (0.6 mL, 0.1 M) and TOPSe (0.6 mL, 0.1 M) were added with a 10 min interval between the two injections. The temperature was raised to 230 °C for 1 h. The temperature was again lowered to 150 °C and zinc undecylenate (0.8 mL, 0.1 M) and TOPSe (0.8 mL, 0.1 M) were added with a 10 min interval between the injections. The temperature was raised to 230 °C for 1 h. The Fe:InP/ZnSe nanocrystals were precipitated by addition of acetone. Aliquots were taken for emission profile characterization using PL. XRD and HRTEM were performed to characterize the crystallinity, size and size distribution of the nanocrystals.

2.3.3.4 Ligand exchange reaction

3-mercaptopropionic acid (0.44 mL, 5 mmol) in PBS (1mL, pH 11) was transferred into a 50 mL round bottom flask and degassed with argon for 5 min. 1 mL of chloroform containing the QDs (30 mg) was then added and the mixture was vigorously stirred at room temperature for 4 h. The aqueous phase was then syringed out and filtered using a Simplepure filter (0.45 μm). Excess MPA was removed by precipitation of MPA-capped QDs with 2-propanol followed by centrifugation, decantation of the supernatant and re-dispersion of the QDs in PBS.

2.3.4 Experimental details pertaining to Chapter 5

2.3.4.1 Synthesis of CdTe/ZnS QDs

The CdTe/ZnS QDs used in the cytotoxicity studies were synthesized following published methods with some modifications [13,14]. $NaBH_4$ (0.0378 g, 1.00 mmol) and Te (0.051 g, 0.40 mmol) were added to deionized water (10 mL) and heated at 80 °C for 30 min to prepare NaHTe as a purple solution. 5 mL of this solution were used for the synthesis of CdTe. $CdCl_2.H_2O$ (0.081 g, 0.40 mmol) and MPA (52 µL, 0.6 mmol) were dissolved in water (15 mL) and the pH was adjusted to 11.7 using 1 M NaOH solution. The Cd/MPA precursor was heated to 100 °C under argon and Te^{2+} solution (5 mL) at 80 °C was injected. The reaction was maintained at 100 °C for 2 h to grow CdTe nanocrystals. The CdTe solution was rapidly cooled in ice and added to a mixed zinc and sulphur precursor solution (1 mL, 0.1 M) prepared from zinc acetate and thiourea. An additional amount of water (5 mL) was added and the pH was adjusted to 11.5. After degassing the solution, it was heated at 90 °C for 1 h to afford MPA-capped CdTe/ZnS. The PL of the QDs was determined by the Nanolog instrument.

2.3.4.2 Bioconjugation of TAT peptide to InP/ZnSe QDs

MPA-capped InP/ZnSe QDs (25 µL, 6 mg/mL), EDC (10 µL, 0.38 g/mL), NHS (10 µL, 0.50 g/mL) and PBS (5 mL) were transferred into an eppendorf tube and incubated at room temperature with gentle mixing for 15 min to activate the carboxylic acid groups. TAT peptide (20 µL, 3.5 mg/mL) was added and the activated QD solution and the reaction system was further incubated at room temperature for 2 h with gentle mixing. The TAT-QD bioconjugates

were centrifuged in 30 kDa MWCO micro-centrifuge tubes at 6 000 rpm for 5 min and washed twice with PBS to remove excess activation agents and unbound TAT. The bioconjugates were resuspended in PBS solution (50 µL) and then stored at 4 °C for further use.

2.3.4.3 Culturing and trypsinization of Caco-2 cells

Caco-2 cells were cultured in a tissue culture flask containing pre-warmed complete growth medium of DMEM supplemented with 10 % foetal bovine serum and 1 % antibiotics. The flask was labeled with the cell line name and date of culture and incubated at 37 °C and 5 % CO_2 in a humidified incubator. The growing cells were observed daily under a Nikon inverted light microscope in order to monitor their confluency. When the cells had reached the desired confluency of 80 %, the culture medium was decanted and the cells were washed with PBS (5 mL). Pre-warmed sterile trypsin (3 mL) was added and the cells placed in the incubator at 37 °C until completely detached from the bottom of the flask (usually within 10 min). The complete growth medium (3 mL) was then added to inactivate the trypsin and the mixture was transferred into a sterile 15 mL tube using a sterile pipette. The cells were recovered by centrifugation at 300 × *g* for 3 min at room temperature. After centrifugation, the supernatant was decanted and the cells were re-suspended in PBS (5 mL) followed by centrifugation at 300 × *g* for 3 min at room temperature. The supernatant was decanted and the cell pellet was re-suspended in complete medium.

2.3.4.4 Treatment of Caco-2 cells with InP/ZnSe QDs for fluorescence imaging

Caco-2 cells were seeded at a density of 1.0 x 10^6 cells/mL in a 6-well plate with cover slips and incubated at 37 °C for 24 h. The media was removed and the cells were treated with 150 µL of TAT-conjugated and unconjugated InP/ZnSe QDs (125 µg/mL) in the media. The cells were further incubated for another 24 h. The media was then removed and 4 % paraformaldehyde (200 µL) was added into each well to fix the cells. The cells were incubated for 10 min. The cover slips were washed with PBS (2 x 200 µL) and mounted on microscopy slides containing mounting media. Fluorescent images were taken using a ZEISS Axioplan 2 Imaging microscope.

2.3.4.5 Cell viability using MTT Assay method

The MTT stock solution was prepared by dissolving 3-(4,5-dimethylthiazol-2-yl)-2,5-diphenyl-tetrazolium bromide in PBS to afford a concentration of 5 mg/mL. Cell proliferation was determined using the MTT assay following the methods described by Mosmann [15] and Freimoser *et al.* [16] with some modifications. In brief, Caco-2 cells were first cultured and trypsinized in the same manner as stated in **Section 2.3.4.3**. The cells were then seeded in 96-well tissue culture plates at a density of 2.0 x 10^5 cells/mL. After growing to 90 % confluency at 37 °C, with 5 % CO_2, the growth medium was removed and replaced with 100 µL of a fresh medium with or without various concentrations of MPA–capped InP/ZnSe and CdTe/ZnS nanocrystals that ranged from 62.5 to 500 µg/mL. Treatments were done in triplicate. After 24 h of treatment, the medium was removed followed by addition of 100 µL of fresh medium without the QDs and 10 µL of 5 mg/mL MTT solution. The plates were further incubated for 4 h. At the

end of the incubation period, the medium was removed from each well and replaced with 50 µL of DMSO. The plates were then shaken on a rotating shaker for 10 min before taking readings at 560 nm using a BMG Labtech POLARstar Omega microplate reader. Results of cellular viability were tabulated as mean absorbance of each drug dose expressed as a percentage of the untreated control and plotted against drug concentration. To exclude background readings, three wells were seeded with cells but were not treated and neither was MTT added. To correct for non-specific binding of MTT onto the plate, MTT only was added to two wells without cells. Results of triplicate wells were expressed as means ± SD.

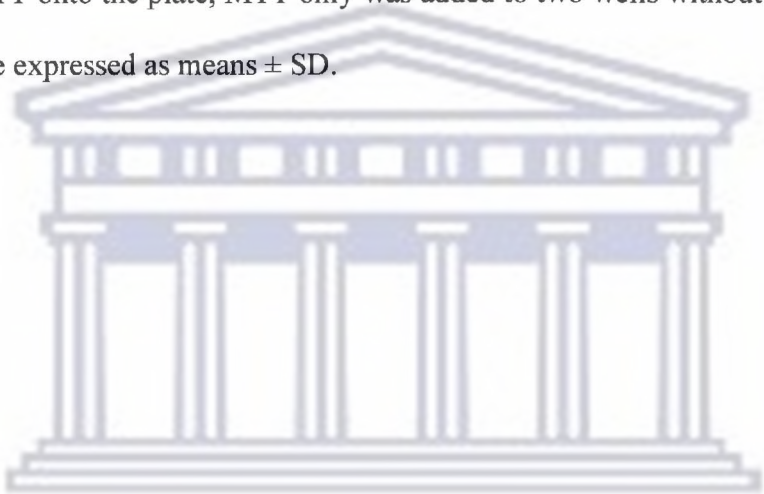

2.4 References

1 Verhoeven JW, *Pure Appl. Chem.*, **1996**, *68, 2223*

2 Fluorescence Fundamentals, accessed on 10 November 2012. *<http://www.invitrogen.com/site/us/en/home/References/Molecular-Probes-The-Handbook/Introduction-to-Fluorescence-Techniques.html>*

3 Byun H-J, Song W-S, Yang H. *Nanotechnology,* **2011**, *22, 235605*

4 HORIBA JOBIN YVON Nanolog Training Notes, 2009

5 Harley JH, Wiberley SE, Instrumental analysis, John Wiley and Sons, 1954.

6 Narayanaswamy A, Feiner LF, Meijerink A, van der Zaag PJ, *ACS Nano,* **2009**, *3, 2539*

7 Uznanski P, Bryszewska E, *J Mater. Sci.*, **2010**, *45, 1547*

8 Acharya S, Pradhan N, *J. Phys. Chem. C,* **2011**, *115, 19513*

9 Ryu E, Kim S, Jang E, Jun S, Jang H, Kim B, Kim S-W, *Chem. Mater.*, **2009**, *21, 573*

10 Hussain S, Won N, Nam J, Bang J, Chung H, Kim S, *ChemPhysChem.*, **2009**, *10, 1466*

11 Talapin DV, Gaponik N, Borchert H, Rogach AL, Haase M, Weller H, *J. Phys. Chem. B,* **2002**, *106, 12659-12663*

12 Xie R, Peng X, *J. Am. Chem. Soc.*, **2009**, *131, 10645*

13 Yuan Z, Zhang A, Cao Y, Yang J, Zhu Y, Yang P, *J. Fluoresc.*, **2012**, *22, 121*

14 Fang Z, Li Y, Zhang H, Zhong X, Zhu L, *J. Phys. Chem. C,* **2009**, *113, 14145*

15 Mosmann T. *J. Immunol. Methods,* **1983**, *65, 55*

16 Freimoser FM, Jakob CA, Aebi M, Tuor U, *Appl. Environ. Microbiol.*, **1991**, *65, 3727*

CHAPTER 3: SYNTHESIS AND CHARACTERIZATION OF SURFACE MODIFIED InP/ZnSe QDS

3.1 Introduction

The colloidal group III-V semiconductor QDs have attracted enormous interest in the past two decades, emerging as alternatives to cadmium-based QDs [1]. Within the group III-V semiconductor nanomaterials, InP QDs appear popular due to their relatively narrow room temperature band gap (1.35 eV) and large excitonic Bohr radius (11.3 nm) [2]. The InP QDs exhibit a broadband emission spectrum comparable to that of CdSe, while at the same time being more environmentally benign [3].

However, owing to the covalent nature of the group III-V, their preparation is more difficulty compared to II-VI systems. The precursors of group III-V nanocrystals possess strong covalent bonding which calls for high synthetic temperatures and long reaction times. This has led to the adoption of the hot-injection [4] and heating-up [5] methods for their preparation. Most of the precursors widely used include indium halides and carboxylates. Specifically, indium chloride has found wide use alongside the coordinating solvents such as trioctylphosphine (TOP) and trioctylphosphine oxide (TOPO). However, strongly coordinating solvents impart a negative influence on the growth of the nanocrystals [6]. Thus, weakly or non-coordinating solvents are highly recommended in this type of work. Furthermore, amine compounds have been reported to prevent the decomposition of the precursors [7]. Inorganic shells of wider bandgap materials (for type I core/shell QDs) are employed to improve optical properties of QDs [8]. In InP research,

the major focus has been on core/shell InP/ZnS QDs. Very little has been reported on ZnSe overcoated InP core/shell QDs [9]. In this chapter, we discuss the synthesis and characterization of InP/ZnSe QDs.

3.2 Results and discussion

3.2.1 InP/ZnSe synthesis using non-coordinating solvent 1-octadecene

Highly fluorescent and monodisperse InP/ZnSe nanocrystals were synthesized by reacting indium acetate with tris(trimethylsilyl phosphine) ($P(TMS)_3$) using palmitic acid as the surfactant and 1-octadecene as the non-coordinating solvent. The palmitic acid, an intermediate chain length fatty acid, facilitates controlled nucleation and growth rates needed for the synthesis of monodisperse InP semiconductor nanocrystals in non-coordinating solvents [10]. We maintained the ratio of 1: 3 indium precursor to surfactant because it yields high-quality nanocrystals [11].

3.2.1.1 Photoluminescence properties

Figure 3.1 shows normalized photoluminescence (PL) spectra of three aliquots taken during the synthesis of the NCs. The spectra show that there is no significant change in the emission peak maxima for aliquots taken 30 min and 120 min into the core growth. Bawendi's group reported that in the synthesis of InP, molecular phosphorus precursors are completely used up at the InP nucleation step culminating in subsequent growth of nanocrystals exclusively being attributed to ripening from non-molecular InP species in the solution [7]. The as-prepared InP/ZnSe NCs showed a maximum emission wavelength at 574 nm. An aliquot taken 120 min into core growth gave an emission peak of 579 nm. The slight blue shift (from 579 –574 nm) observed for these type I core/shell systems is contrary to expectations and is attributed to the fact that

photoluminescence in ZnSe shelled–InP is less contributed by defect emission in comparison to the bare InP NCs [9]. The photoluminescence quantum yield (QY) was measured as 6 %.

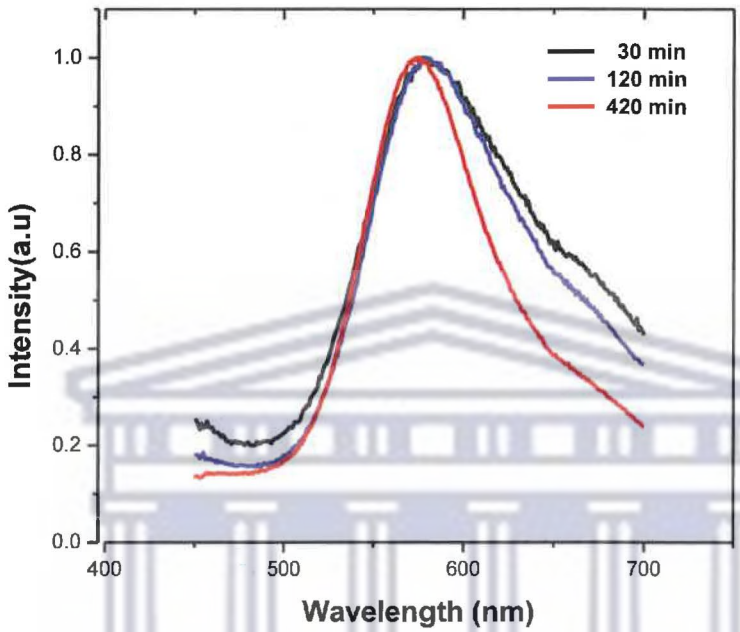

Figure 3.1 The normalized photoluminescence (PL) spectra of three aliquots taken during the synthesis of the NCs

Trap state-related emissions are also exhibited in the PL spectra. The surface states are a consequence of unsatisfied (dangling) bonds that are found at the reconstructed surface. ZnSe, with a lower lattice mismatch with InP, was used as an inorganic shell instead of ZnS that has a relatively large lattice mismatch in the zinc blende phase of about 7.6 % [12]. **Figure 3.2** shows each PL spectrum deconvoluted into two Gaussian peaks. The deep trap-related emissions for the InP/ZnSe and bare InP NCs are around 627 nm and 640 nm respectively. The blue shift observed is an evidence of successful coating of the core and shows that the shell reduces the surface states. The ZnSe shell also greatly reduced the ratio of trap-related emission to band edge emission by a calculated factor of 1.4 [13].

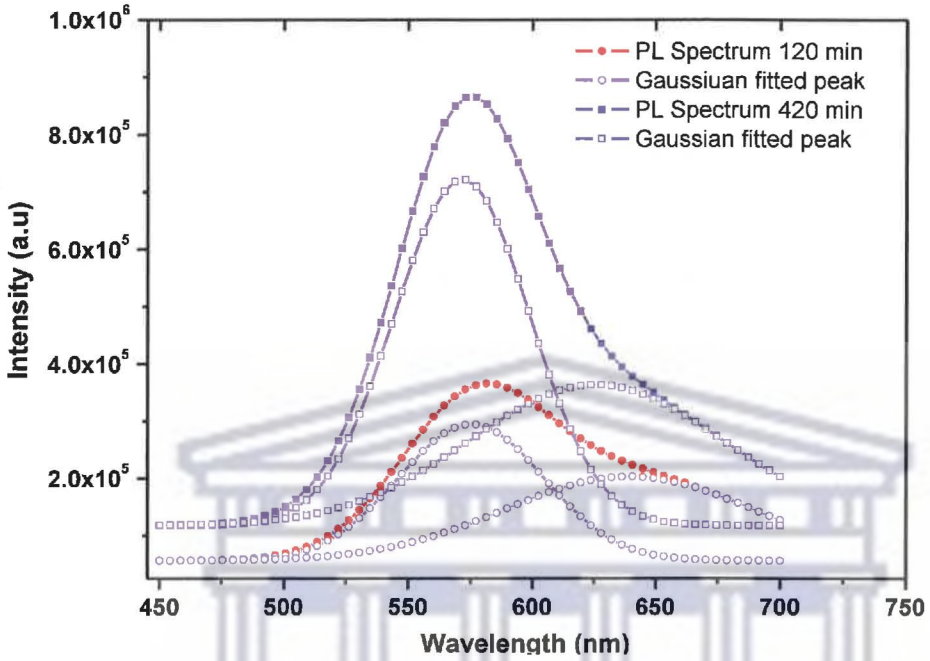

Figure 3.2 PL spectra deconvoluted into Gaussian peaks

3.2.1.2 Structural properties

Figures 3.3 and **3.4** show the HRTEM micrographs and EDX spectrum of the core/shell InP/ZnSe nanocrystals respectively. The insert in **Figure 3.3** is the selected area electron diffraction (SAED) pattern of the nanocrystals. The lattice fringes in the insert confirm the good crystallinity of the nanocrystals with lattice fringe distance of 0.2934 nm which is in good agreement with the plane spacing of 0.29343 nm for <220> planes of the zinc blende structure. The lattice fringes are continuous throughout the QD indicating the epitaxial nature of ZnSe shell growth [14]. Kim *et al.* [9] reported a lattice fringe distance of 0.34 nm which also agreed well with the spacing of 0.3388 nm between the <111> planes of the InP/ZnSe nanocrystals. The

selected area electron diffraction (SAED) pattern (Insert, **Figure 3.3**) confirmed the zinc blende structure of the NCs with three rings indexed to <111>, <220> and <311> lattice planes with corresponding calculated d-spacing values of 0.3404, 0.2069 and 0.1772 nm in good agreement with the standard values. The EDX results for the InP/ZnSe NC sample showed an In : P : Zn : Se ratio of 1:0.96:1.47:0.17 showing an indium-rich core with a zinc-rich particle surface. Thus the InP core has an indium-terminated surface while the shell has zinc-terminated surface. The Zn/In ratio of 1.47 confirms that the InP cores are covered by a ZnSe shell. Even higher ratios (2.34) have been reported for ZnS-capped InP nanocrystals [15].

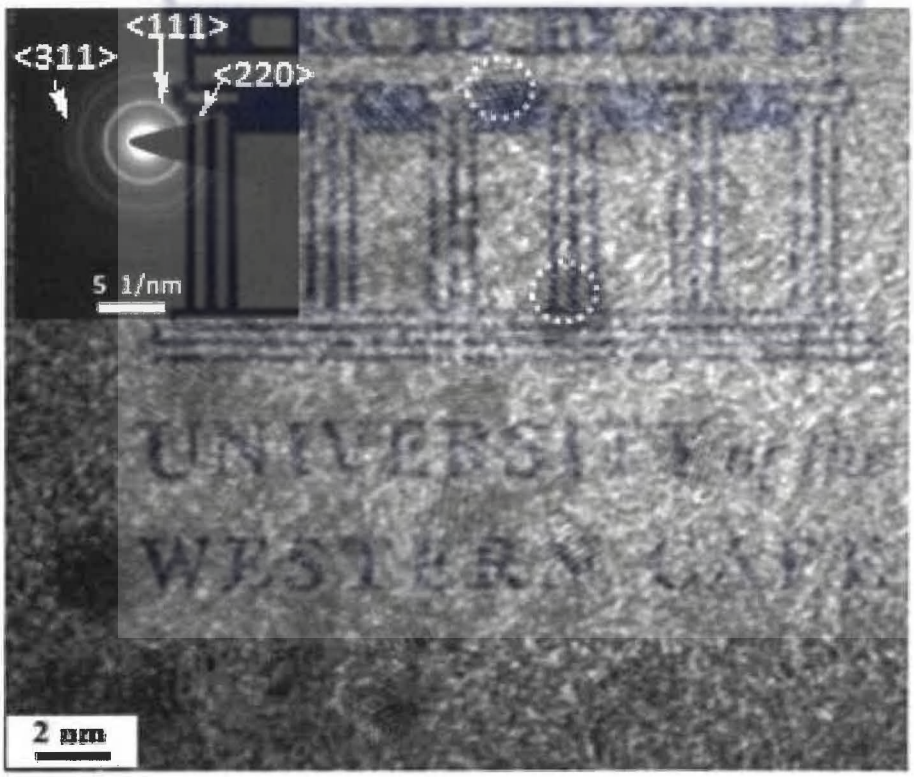

Figure 3.3 HRTEM micrograph of the InP/ZnSe NCs. (Insert is the SAED pattern).

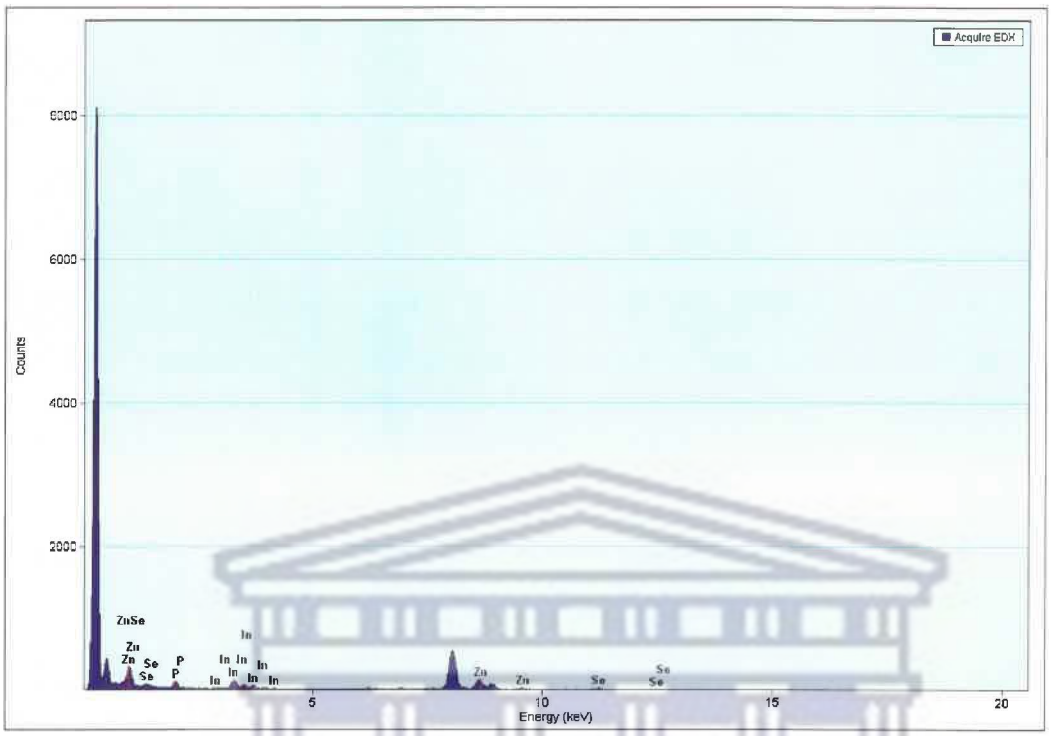

Figure 3.4 EDX spectrum of the InP/ZnSe NCs

3.2.2 InP/ZnSe synthesis using non-coordinating polyethylene glycol as solvent

Polyethylene glycol (PEG) was used as a solvent in the synthesis of high quality InP/ZnSe QDs. The procedure was an adaptation of a published method by Husaain *et al.* [16]. To our knowledge, this is the first time the procedure is applied to ZnSe-overcoated InP QDs. In our system, we chose palmitic acid as a surfactant while literature reported the use of myristic acid. Both acids have been shown to be the best ligands providing balanced nucleation and growth rates that are necessary for the synthesis of relatively monodisperse InP QDs [10]. For the growth of the ZnSe shell, the zinc precursor solution was added at 200 ^{o}C. The temperature was

lowered to 180 °C and the selenium precursor was added. The growth process was allowed to take place for 1h at 230 °C. Deposition of the ZnSe shell has been reportedly effected at temperatures above 220 °C with temperature modulation depending on core size as well as preferred shell thickness [17]. These growth temperatures are also typical for growth of ZnS shells [18].

3.2.2.1 Photoluminescence properties

The highly luminescent as-prepared InP/ZnSe NCs showed a maximum emission wavelength at 605 nm. It was not easy to monitor the PL process during synthesis because of the viscosity of the solvent. PEG, a solid at room temperature, was in the molten state at the reaction temperature. However, the QD solution (reddish brown) was not uniformly distributed in the molten PEG solution. As a result, temporal evolutions of the PL spectrum could not be monitored through the periodic sampling of the reaction system. **Figure 3.5 (a)** shows the PL spectrum of the as-prepared QDs after the synthesis process. The FWHM was found to be 114 nm. The FWHM indicates that the size distribution of the as-prepared InP/ZnSe was very large. A similar large value (110 nm) has been reported for manganese-doped InP NCs [19].

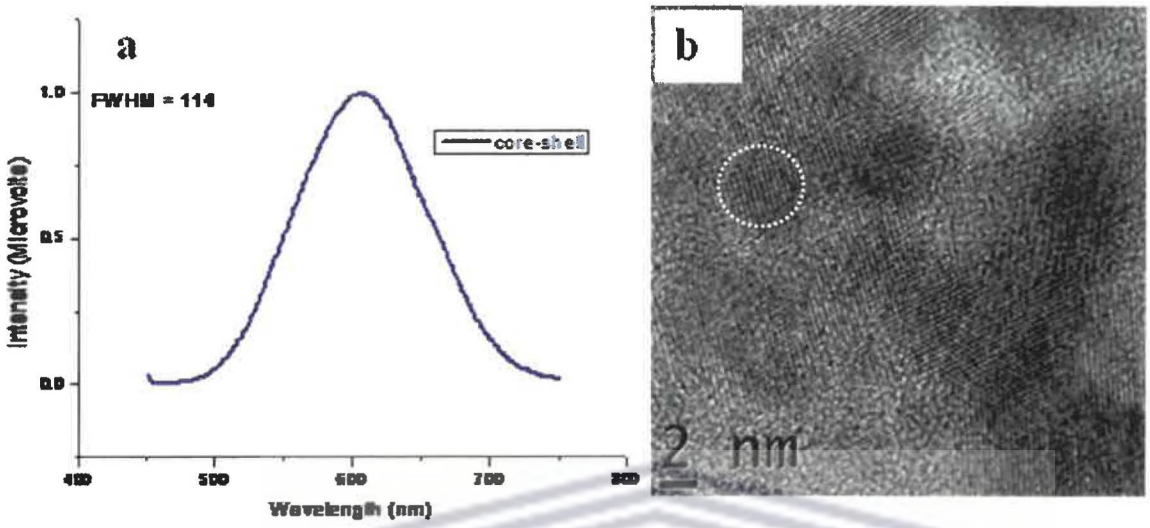

Figure 3.5 (a) The normalized photoluminescence (PL) spectrum and (b) HRTEM micrograph of the as-prepared InP/ZnSe.

3.2.2.2 Structural properties

The HRTEM micrograph (**Figure 3.5 (b)**) showed lattice fringes from the particles indicating that the QDs were of good quality. The lattice fringes are also continuous throughout the QD indicating the epitaxial nature of ZnSe shell growth [14].

3.2.3 InP/ZnSe synthesis using double injection with high moles of precursors

Double injection of precursors is a procedure of adding precursors for nanoparticle synthesis for a second time during the synthesis process. The procedure has an advantage of increasing the amount of monomers available of the growth of the nanoparticles. The effect of double injection of precursors was investigated in the synthesis of InP/ZnSe nanocrystals. The concept of secondary injections has been reported in literature by Battaglia and Peng [10]. After first

preparing the InP NCs in a non-coordinating solvent 1-octadecene, these investigators carried out secondary injections of indium and selenium at 250 °C. They recommended that the secondary injection temperature had to be lower than the primary growth temperature of 270 °C to avoid continuous nucleation which would result in a broad size distribution and therefore hinder their application in the biological field that requires more uniform nanoparticles. In our double injection reaction, the first part involved growing for 30 min the InP core in the presence of zinc undecylenate using the In:P:Zn ratio of 1:0.5:0.4 where 0.4 mmol of indium precursor were used. Addition of the long-chained zinc carboxylate, zinc undecylenate at this stage was done in order to support the nucleation and growth processes. Xu *et al.* [20] have also reported the use of the zinc carboxylate, arguing that it serves as a stabilizer in the reaction system. The second part of the double injection reaction involved the addition of the same amounts of indium and phosphorus precursors. After allowing further core growth for 1 h, ZnSe shell forming precursors were then added. The effect of In^{3+}: Zn^{2+} ratio was also investigated using ratios of 1:0.4 and 1:0.75. The progress of the reactions was monitored by PL analysis of aliquots.

3.2.3.1 Photoluminescence properties

Figures 3.6 and **3.7** show the evolution of PL spectra with time for the nanocrystals synthesized using the In^{3+}:Zn^{2+} ratio of 1:0.75 and the normalized PL spectra for the two In^{3+}: Zn^{2+} ratios of 1: 0.4 and 1: 0.75 respectively. The PL spectra showed emission peaks of 610 and 599 nm for the In^{3+}:Zn^{2+} ratios of 1:0.4 and 1:0.75 respectively. A blue shift in the emission peak position was observed with the increase in zinc concentration (see **Figure 3.7**). A similar pattern was reported by Thuy *et al.* [21]. These researchers synthesized In(Zn)P/ZnS using the heating up method,

with all the precursors (In, P, Zn, and S) mixed at room temperature and then quickly heated to 250 – 300 °C. The ZnS shell was the deposited onto the In(Zn)P core as a distinct step at a much lower temperature. The researchers reported a systematic redshift of the steady-state photoluminescence peak with decreasing Zn^{2+}: In^{3+} molar ratio.

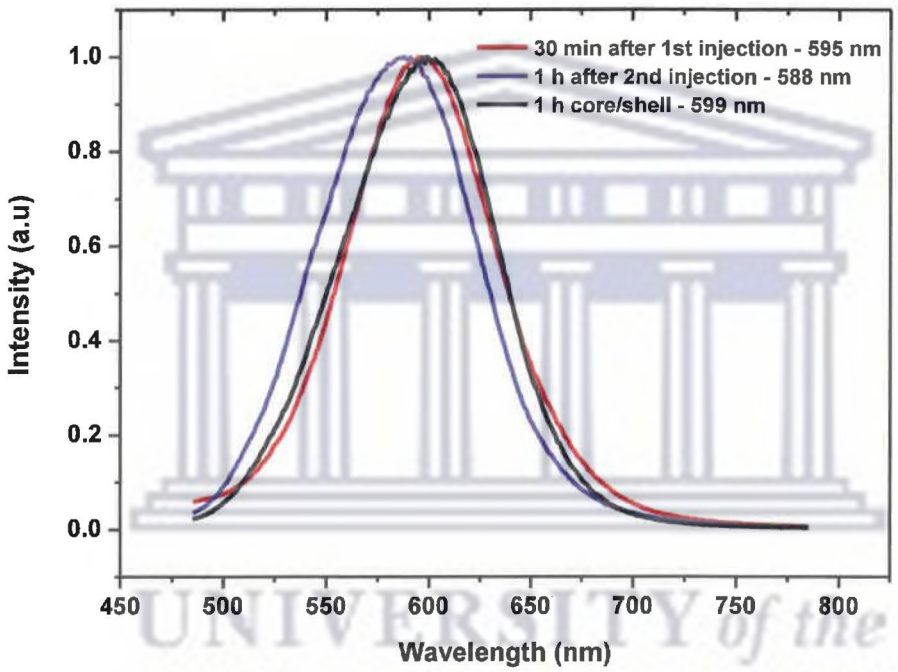

Figure 3.6 Evolution of PL spectra with time for route with In^{3+}:Zn^{2+} ratio of 1:0.4

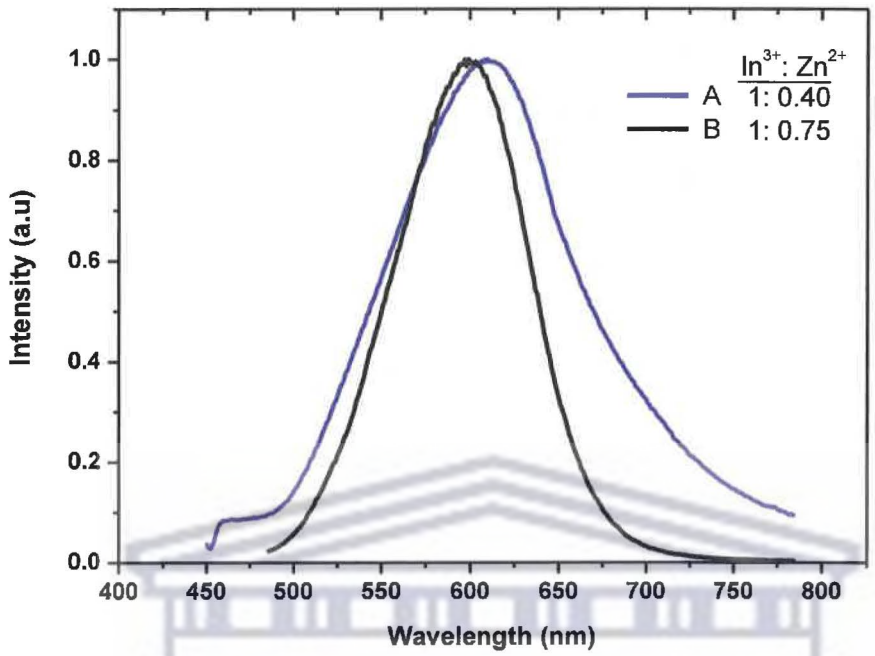

Figure 3.7 Normalized PL spectra for InP/ZnSe QD synthetic methods with In^{3+}: Zn^{2+} ratios of 1: 0.4 (A) and 1: 0.75 (B).

Nann and co-workers also investigated the influence of zinc carboxylate concentration on the optical properties of InP/ZnS [20]. They added zinc undecylenate to indium(III) chloride and hexadecylamine when they synthesized InP using the hot-injection method. Tris(trimethylsilyl)phosphine-octadecene solution was injected at 280 °C, followed by the core growth at 260 °C. Additional zinc undecylenate and zinc diethyldithiocarbamate or cyclohexylisothiocyanate were added for the ZnS overcoating of the InP NCs. Their PL studies showed that the emission wavelength blue shifted with increasing initial concentration of the zinc carboxylate. They reported that the zinc carboxylate slowed down the crystal growth rate.

3.2.4 InP/ZnSe synthesis using single injection with high moles of precursors

The effect of using high moles of precursors was also investigated. Similar studies were reported by Ryu *et al.* [22] when they synthesized InP/ZnS NCs. They used amounts of the indium precursor ranging from 0.04 – 0.08 mmol maintaining the In : P ratio of 1: 0.5. The investigators reported a red shift in emission wavelength with increasing moles of the precursor. In our investigations, instead of the usual 0.2 mmol of indium precursor and 0.1 mmol of the phosphorus precursor, the reactions were scaled up four times in order to match the total amount of precursors used in the double injection method described in **Section 3.2.3**. At these precursor levels, the effect of reaction time during the core growth phase was also investigated. The core growth time was varied between 4 h and 8 h. In the discussion following, the method involving core growth for 4h shall be referred to as route A and the one involving core growth time of 8 h route **B.**

3.2.4.1 Photoluminescence properties

A significant improvement in the emission profiles was observed on using high moles of precursors. However, there was no significant change in the emission wavelength on doubling the core growth time. The growth of the nanocrystals was monitored by measurement of the photoluminescence spectra of the aliquots taken at different time intervals. **Figures 3.8** and **3.9** display the emission profiles with time for routes **A** and **B** respectively.

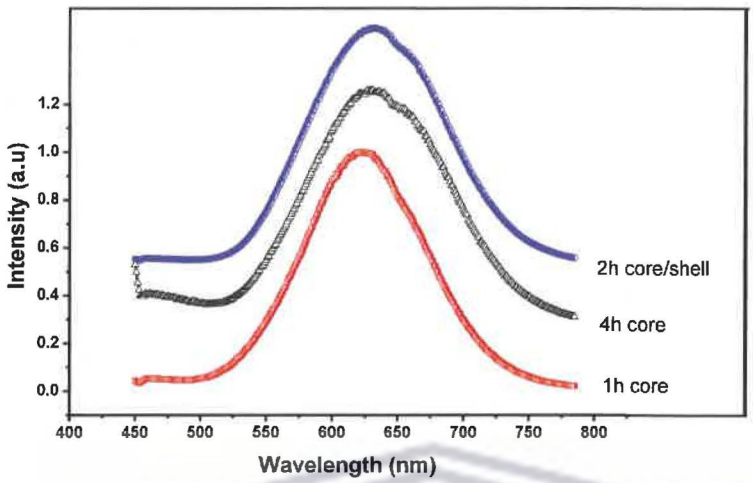

Figure 3.8 Evolution of PL spectra with time for route **A**

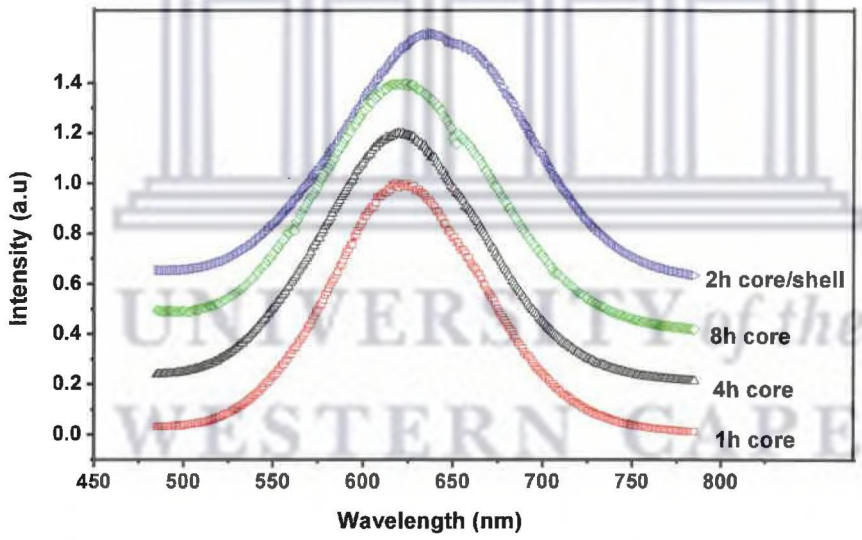

Figure 3.9 Evolution of PL spectra with time for route **B**

The maximum emission wavelengths were 633 nm and 637 nm respectively for QDs fabricated with core growth times of 4 h (route **A**) and 8 h (route **B**) respectively. These improved emission profiles were attributed to higher concentrations of precursors and not to longer growth times.

According to Li *et al.* [23], when Ca_3P_2, a source of the phosphorus precursor PH_3, was consumed, any further extension of time did not culminate in further spectral evolution. The FWHM obtained were 121 and 119 nm for routes **A** and **B** respectively.

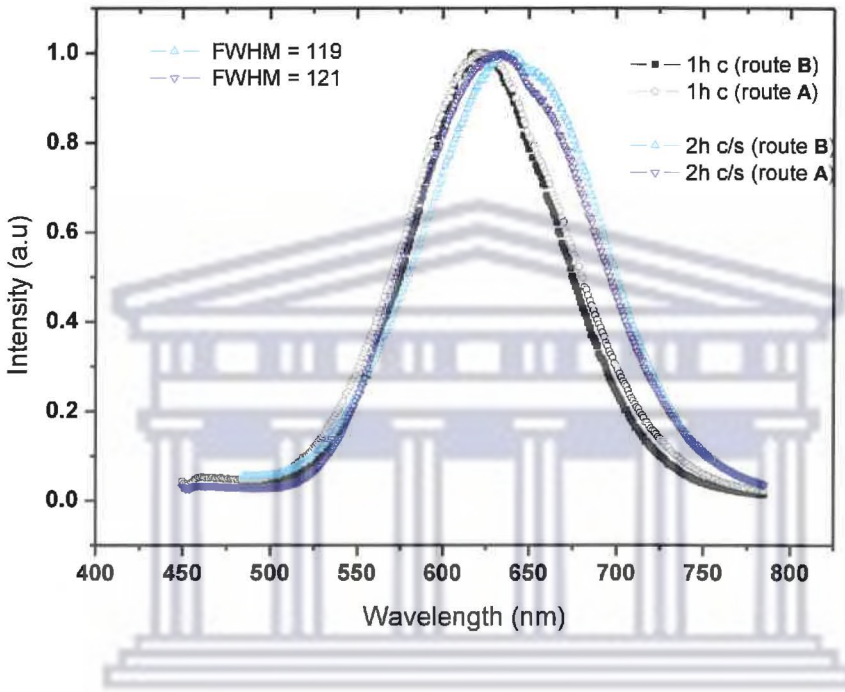

Figure 3.10 PL spectra for routes **A** and **B** generated from analysis of aliquots taken after 1h into core growth time and 2 h of shell growth

In a reported synthesis of InP, molecular phosphorus precursors are completely used up at the InP nucleation step culminating in subsequent growth of nanocrystals exclusively being attributed to ripening from non-molecular InP species in the solution [24]. With the Ostwald ripening mechanism (also called coarsening or defocusing mechanism) in operation at this stage (for both routes **A** and **B**), the nanocrystal size distribution broadens as reflected by the large FWHM. Some smaller nanocrystals will be shrinking in size and eventually dissolving while the larger nanocrystals will be growing [25]. To circumvent the problem of complete depletion of molecular phosphorus precursors, Reiss' group reported an InP synthetic scheme based on the

use of poisonous *in situ* generated gaseous PH_3 [23]. In this reaction, the PH_3 was generated according to the following equation:

$$Ca_3P_2 + 6HCl \rightarrow 2PH_3 + 3CaCl_2 \qquad \text{(Equ. 3.1)}$$

The Ca_3P_2 / HCl reaction ensured continuous supply of the phosphorus precursor to the reaction system. Pham *et al.* [26] have also synthesized InP/ZnS using PH_3 gas generated in situ from the reaction of Zn_3P_2 with H_2SO_4. This also ensured continuous supply of phosphorus precursors to the reaction.

3.2.4.2 Structural properties

The TEM micrographs and particle size distribution curves of the QDs synthesized by routes **A** and **B** are shown in **Figure 3.11** and **Figure 3.12** respectively. The mean sizes of the nanocrystals, estimated from the size distribution curves for routes A and B are 4.60 ± 0.33 and 4.70 ± 0.47 nm respectively.

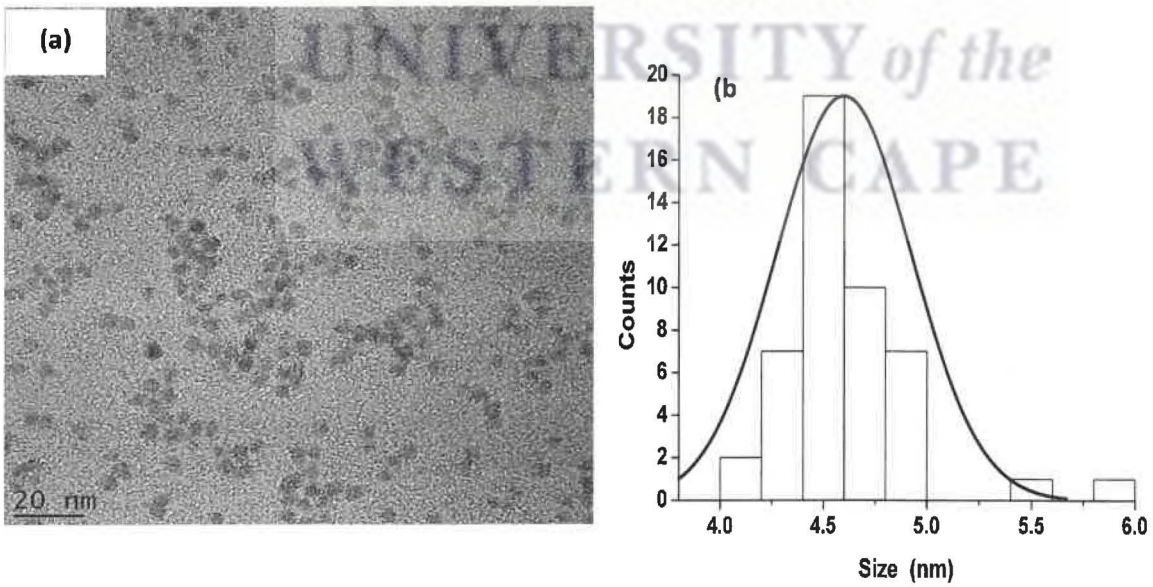

Figure 3.11 TEM micrographs (**a**) and size distribution curve (**b**) for InP/ZnSe NCs synthesized following route **A** involving InP core growth for 4h.

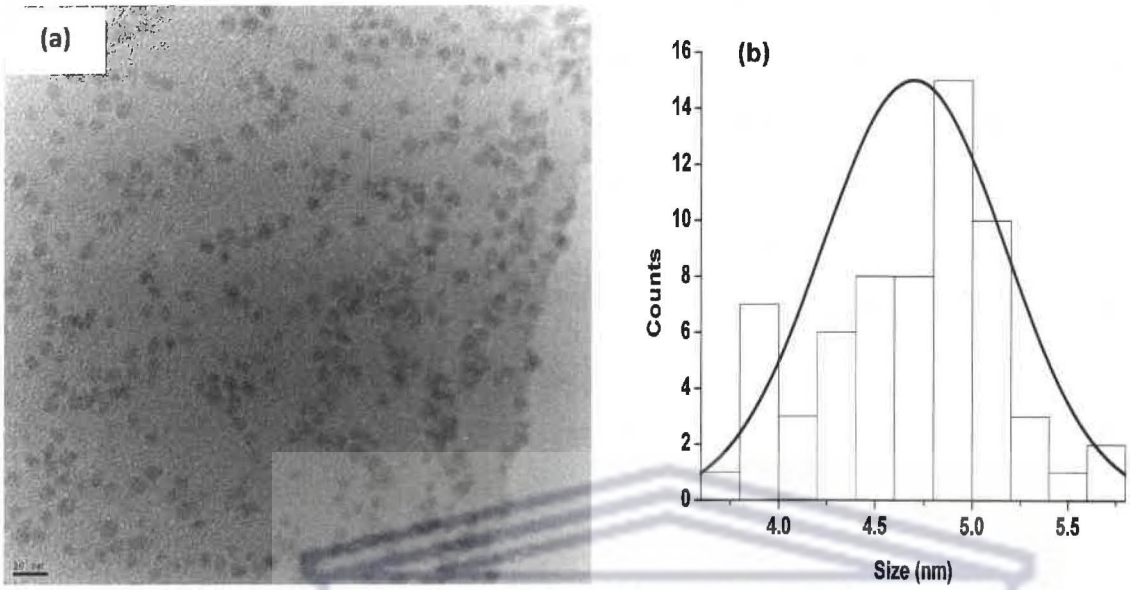

Figure 3.12 TEM micrographs (**a**) and size distribution curve (**b**) for InP/ZnSe NCs synthesized following route **B** involving InP core growth for 8h.

3.2.5 Ligand exchange reactions using 3-mercaptopropionic acid as ligand

Generally, phase transfer reactions involve ligand exchange of the native hydrophobic surfactant on the nanocrystal surfaces with the hydrophilic one (see **Section 1.8.1.1**). **Figure 3.13** shows a schematic display of ligand exchange reaction.

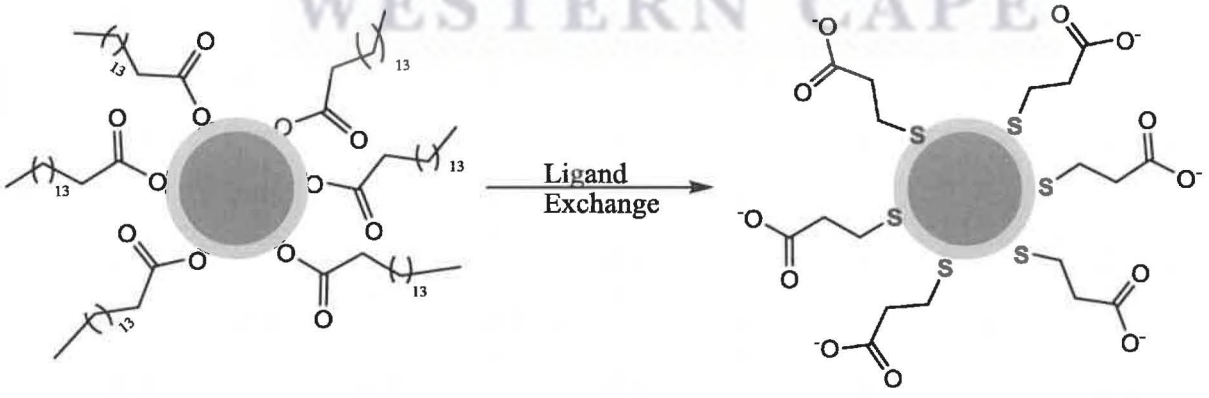

Figure 3.13 Schematic representation of ligand exchange at the surface of the InP/ZnSe NCs

With the InP/ZnSe nanocrystals synthesized using the organometallic route, phase transfer reactions were necessary to make them compatible with the aqueous media. The nanocrystals were made water-soluble by exchanging the native palmitic acid layer with 3-mercaptopropionic acid (MPA) ligand. The MPA ligand provided a thiol group for anchoring to the nanocrystal surface [27] and terminal carboxylic acid functionality for both hydrophilicity and coupling to biomolecules [28,29]. PBS was chosen as the aqueous medium with its pH adjusted to around 11 (slightly above MPA pKa(thiol) value of 10.8). At this pH, the thiol (-SH) group was deprotonated yielding a thiolate ($-S^-$) functionality that has been reported to have greater binding energy on nanocrystal surfaces than the protonated form [30]. A chloroform solution of the MPA-capped nanocrystals was transferred into the PBS phase containing the deprotonated ligand and stirred at room temperature for 4 h. Prasad and co-workers have reported the use of mercaptosuccinic acid in ligand exchange reactions on myristic acid-capped InP/ZnS nanocrystals [31]. Other ligands that have been used to make InP-based nanocrystals dispersible in the aqueous media include dihydrolipoic acid (DHLA), L-cysteine, and D-penicillamine [32].

3.2.5.1 Optical properties of MPA-capped InP/ZnSe QDs

Successful ligand exchange was confirmed using PL studies. **Figure 3.14** shows the PL spectra of InP/ZnSe nanocrystals before and after ligand exchange. The MPA-capped InP/ZnSe nanocrystals gave an emission peak of 636 nm. The red-shift in the emission peak was attributed to changes in the dielectric environment of the solvents from hexane to water [33]. Tsay *et al.* [34] ascribed the red-shift observed after carrying out ligand exchange reaction for TOPO-capped CdSe/CdS/ZnS using phytochelatin-related peptide, to possible changes in the electronic interactions between the nanocrystal excitonic states and the new ligand. The spectral shift was

attributed to the interaction of QD exciton with molecular orbitals of the surface recognition domain in the peptide. Talapin *et al.* [35] attributed PL shifts after ligand exchange to the redistribution of electron density in the semiconductor core caused by the passivating groups. They reported observing reversible PL spectral shift for amine / TOPO ligand exchange reactions using CdSe/ZnS QDs.

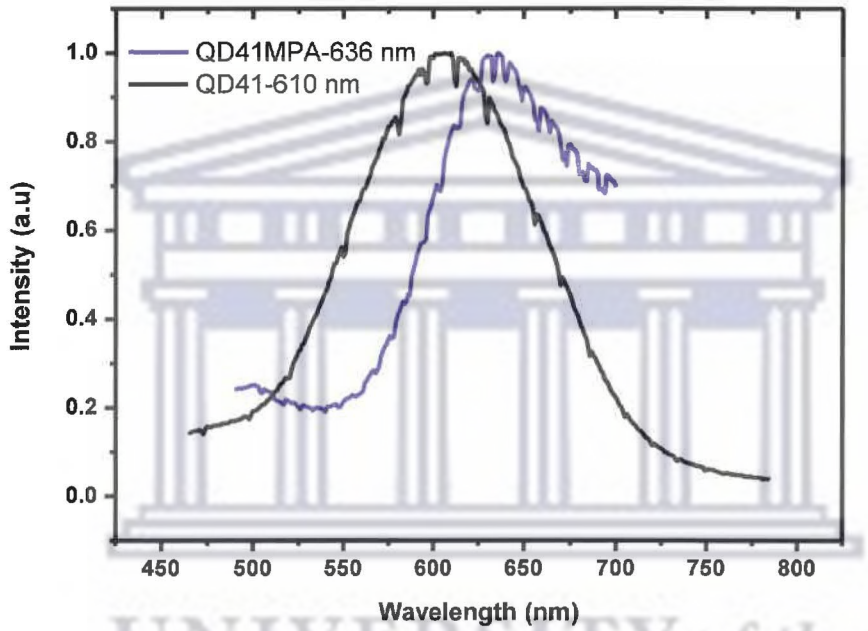

Figure 3.14 PL spectra of InP/ZnSe nanocrystals before (black line) and after (blue line) ligand exchange

3.3 Conclusions

InP/ZnSe QDs were successfully synthesized in ODE under 8 h and gave a QY of 6 % comparable to the only reported literature value of 6.8 % for InP/ZnSe QDs synthesized over several days [9]. The QDs were also successfully synthesized using PEG as a solvent yielding QDs with a maximum emission wavelength of 605 nm.

Secondary injection of precursors in the presence of Zn^{2+} ions of the InP core resulted in an increase in the maximum emission wavelength to around 610 nm. A blue shift was observed in the emission profile on increase in zinc concentration.

It was shown that starting with high moles of precursors would yield QDs with red-shifted emission profiles. However doubling the reaction time did not significantly change the emission profile as further growth of the InP cores is ascribed to ripening from non-molecular InP species present in solution after the depletion of phosphorus precursors at the nucleation stage.

InP/ZnSe QD surfaces were successfully modified using the monodentate ligand 3-mercaptopropionic acid. The observed red-shift in the emission profile was attributed to changes in the dielectric environment of the solvents.

3.4 References

1 Byun H-J, Song W-S, Yang H, *Nanotechnology,* **2011**, *22, 235605*

2 Langof L, Fradkin L, Ehrenfreund E, Lifshitz E, Micic OI, Nozik A, *J. Chem. Phys.,* **2004**, *297, 93*

3 Kim S, Kim T, Kang M, Kwak SK, Yoo TW, Park LS, Yang IY, Hwang S, Lee JE, Kim SK, Kim S-W, *J. Am. Chem. Soc.,* **2012**, *134, 3804*

4 Murray CB, Norris DJ, Bawendi MG, *J. Am. Chem. Soc.,* **1993**, *115, 8706*

5 Li L, Reiss P, *J. Am. Chem. Soc.,* **2008**, *130, 11588*

6 Xu S, Ziegler J, Nann T. *J. Mater. Chem.,* **2008**, *18, 2653*

7 Allen PM, Walker BJ, Bawendi MG, *Angew. Chem. Int. Ed.,* **2010**, *49, 760*

8 Fitzmorris BC, Cooper JK, Edberg J, Gul S, Guo J, Zhang JZ, *J. Phys. Chem. C,* **2012**, *116, 25065*

9 Kim MR, Chung JH, Lee M, Lee S, Du-Jang D-J. *J. Colloid Inter. Sci.,* **2010**, *350, 5*

10 Battaglia D and Peng X, *Nano Lett.,* **2002**, *2, 1027*

11 Xu S, Kumar S, Nann T, *J. Am. Chem. Soc.,* **2006**, *128, 1054*

12 Huang K, Demadrille R, Silly MG, Sirotti F, Reiss P, Renault O, *ACS Nano,* **2010**, *4, 4799*

13 Protiere M, Reiss P, *Chem. Commun.,* **2007**, *2417*

14 Gao S, Zhang C, Liu Y, Su H, Wei L, Huang T, Dellas N, Shang S, Mohney SE, Wang J, Xu J, *Opt. Express,* **2011**, *19, 5528*

15 Byun H-J, Lee JC, Yang H, *J. Colloid Inter. Sci.,* **2011**, *355, 35*

16 Hussain S, Won N, Nam J, Bang J, Chung H, Kim S, *ChemPhysChem.,* **2009**, *10, 1466*

17 Bang J, Park J, Lee JH, Won N, Nam J, Lim J, Chang BY, Lee HJ, Chon B, Shin J, Park JB, Choi JH, Cho K, Park SM, Joo T, Kim S, *Chem. Mater.,* **2010**, *22, 233*

18 Dung MX, Mohapatra P, Choi J-K, Kim J-H, Jeong S, Jeong H-D, *Bull. Korean Chem. Soc.,* **2012**, *33, 1491*

19 Sahoo Y, Poddar P, Srikanth H, Lucey DW, Prasad PN, *J. Phys. Chem. B,* **2005**, *109, 15221*

20 Xu S, Klama F, Ueckermann H, Hoogewerff J, Clayden N, Nann T, *Sci. Adv. Mater.*, **2009**, *1, 125*

21 Thuy UTD, Reiss P, Liem NQ, *Appl. Phys. Lett.*, **2010**, *97, 193104*

22 Ryu E, Kim S, Jang E, Jun S, Jang H, Kim B, Kim S-W, *Chem. Mater.*, **2009**, *21, 573*

23 Li L, Protière M, Reiss P, *Chem. Mater.*, **2008,** *20, 2621*

24 Allen PM, Walker BJ, Bawendi MG, *Angew. Chem. Int. Ed.*, **2010**, *49, 760*

25 Peng X, Wickham J, Alivisatos AP, *J. Am. Chem. Soc.*, **1998**, *120, 5343*

26 Pham TT, Tran TKC, Nguyen QL, *Adv. Nat. Sci. Nanosci. Nanotechnol.*, **2011**, *2, 025001*

27 Silva FO, Carvalho MS, Mendonça R, Macedo WAA, Reiss P, Schiavon MA, Balzuweit K, *Nanoscale Res. Lett.*, **2012**, *7, 536*

28 Zhang Y, Clapp A, *Sensors*, **2011**, *11, 11036*

29 Thanh NTK, Green LAW, *Nano Today*, **2010**, *5, 213*

30 Schapotschnikow P, Hommersom B, Vlugt TJH, *J. Phys. Chem. C*, **2009**, *113, 12690*

31 Yong K-T, Ding H, Roy I, Law W-C, Bergey EJ, Maitra A, Prasad PN, *ACS Nano*, **2009**, *3, 502*

32 Tamang S, Beaune G, Poillot C, De Waard M, Texier-Nogues I, Reiss P, *Proc. SPIE*, **2011**, *7909, 79091B*

33 Wang J, Xu J, Goodman MD, Chen Y, Cai M, Shinar J, Zhiqun Lin, *J. Mater. Chem.*, **2008**, *18, 3270*

34 Tsay JM, Doose S, Pinaud F, Weiss S, *J. Phys. Chem. B*, **2005**, *109, 1669*

35 Talapin DV, Rogach AL, Kornowski A, Haase M, Weller H, *Nano Lett.*, **2001**, *1, 207*

CHAPTER 4: SYNTHESIS OF DOPED InP/ZnSe QDs

4.1 Introduction

The intentional introduction of impurities into semiconductor materials is termed doping [1]. Doping is used as a tool for tuning the optoelectronic, mechanical as well as magnetic properties of materials [2,3]. According to Bera *et. al* [4], when dopants are incorporated in the QDs, they create local quantum states that lie within the band gaps. These quantum states alter the band structures of the doped QDs (d-dots) and hence their optical properties (see **Scheme 4.1**). With the incorporation of the impurities into the nanocrystal lattice, the dominant relaxation route may be transferred from the surface states to the impurity states, resulting in improved radiative efficiency for localized impurity–induced transition [5].

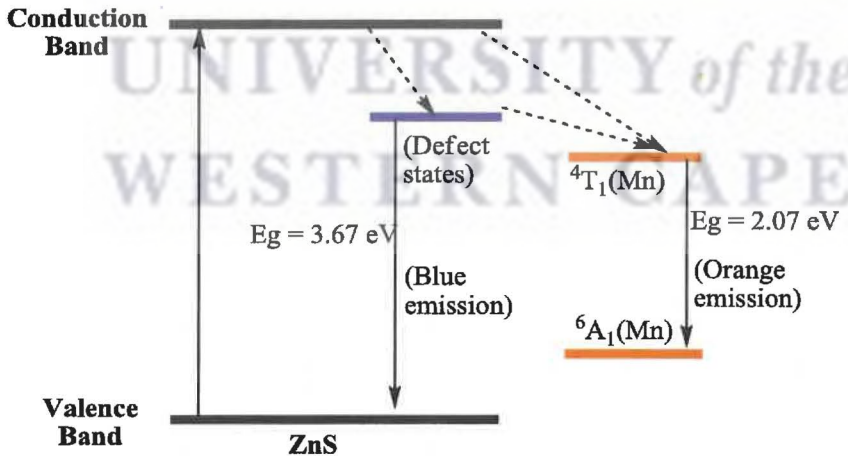

Scheme 4.1 Energy level diagram corresponding to Mn^{2+}-doped ZnS QDs showing the relevant energy levels [6].

Major advances in doping of QDs were first demonstrated by Bhargava *et. al* when they synthesized Mn^{2+}-doped ZnS nanocrystals [7]. Ethylmanganese, prepared from a reaction of manganese chloride and ethylmagnesium chloride, was used as the manganese precursor. A toluene solution of the manganese precursor was added to the precipitation reaction involving diethylzinc and hydrogen sulphide in the presence of methacrylic acid as the surfactant. They reported high photoluminescent efficiencies and luminescent lifetime shortening for nanocrystals in the size range of 2 to 5 nm containing a dopant quantum confined atom. Extensive exploration of this research field has followed after this work. However, a lot of these studies have shown that the incorporation of dopant atoms into the core of the QDs without compromising the quality of the nanocrystals remains a challenging issue [1,8]. The challenges are highlighted in the three models of doping of nanocrystals discussed below.

4.1.1 Nanocrystal doping models

Three models have been documented to explain the doping trends in nanocrystals [9]. The first model, the Turnbull model, assumes that the solubility of the dopant in the nanocrystals is the same as in the bulk material. Thus doping of the small crystallites would be difficult and non-uniform. The second model is the self-purification mechanism in which the dopant atoms are ejected from the internal crystal lattice to the surface is reported to make the doping process challenging [10]. The mechanism is a thermodynamically driven one which assumes that the dopant solubility in the nanocrystals is much lower than in the bulk. The trapped-dopant model is the third model in which the dopant adsorbs onto the QD crystal facet and then is covered by additional QD precursor material is governed by growth kinetics [11].

4.1.2 QD doping methods

Three prominent synthetic methods for the doping of nanocrystals have been reported and involve the nucleation- and growth-doping methods [12] as well as the isocrystalline core/shell synthetic method [13]. These methods will be described here, including the method of doping using single source precursors. A survey of the properties of the doped QDs produced using these methods will also be given.

4.1.2.1 Nucleation-doping method

The nucleation-doping strategy was developed by Peng and co-workers [12]. It is achieved from mixed dopant host precursor solutions during the nucleation stage. Upon cooling, the dopant precursor becomes inactive and the growth of the host continues around the doped nucleus (see **Scheme 4.2**).

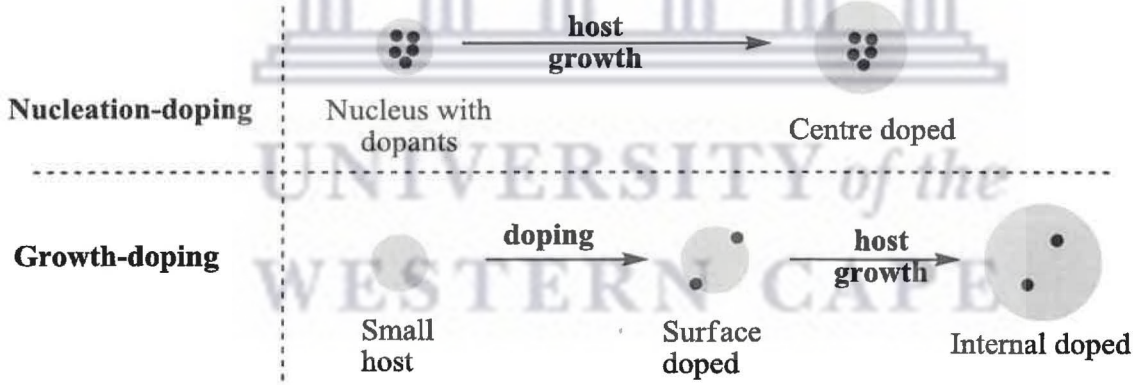

Scheme 4.2 Illustration of nucleation- and growth-doping [12]

Pradhan and Peng [14] have reported synthesis of highly thermally stable (up to 300 °C) Mn:ZnSe d-dots with high photoluminescent quantum yields (40-70 %). Pradhan *et al.* [12] reported that the luminescence of the MnSe:ZnSe d-dots could be tuned from around 575 to 595 nm attributing this red-shift to the growing thickness of the ZnSe shell. The crystal field of each

Mn^{2+} dopant becomes more symmetric in the long range with increasing shell thickness culminating in smaller crystal field splitting of the d-orbitals and hence red-shifted PL. Manganese-doped ZnSe, with a unique small nanocluster MnSe core, a $Zn_{1-x}Mn_xSe$ diffusion region and an outer ZnSe shell have also been reported [15]. The d-dots had tunable wavelength between 565 and 610 nm and high QY (~50 %). Using MnS/ZnS d-dots prepared by the nucleation-doping method, Zheng *et al.* [16] indicated that these systems exhibited photoluminescence enhancement with increasing temperature in the range 140 to 300 K. This enhancement was ascribed to the thermal activation of charge carriers localized at the interface between the MnS core and the ZnS shell. The researchers also reported an increase in the photoluminescence QY from 1.5 to 35 % with increasing shell thickness from 3.1 to 6.0 monolayers (ML). The nucleation-doping method has also been applied in reactions done in the aqueous medium. The first aqueous synthesis of Mn:ZnSe d-dots capped by 3-mercaptopropionic acid was reported in 2009 [17]. These d-dots had maximum emission of 570 nm with a photoluminescence QY of 2.4 %. Mn:ZnSe doped-dots with a diffused Mn(Zn)Se core and a pure ZnSe shell as well as an MPA capping layer have been synthesized by Shao *et al.* [18]. Their QY was improved to 4.8 % while the luminescence peak position was tunable from 572 to 602 nm on increasing the ZnSe shell thickness through prolonged epitaxial growth time. Improved PL QYs of around 35 % have been reported for water-compatible MPA-capped Mn:ZnSe/ZnS doped-core/shell QDs following an increase in the thickness of the ZnS shell [19]. This improvement in the PL QY of the Mn^{2+} $^4T_1 - ^6A_1$ was attributed to the deeper embedding of the Mn^{2+} emission centers inside the doped QDs and way from the surface traps with increase of the ZnS shell. Schneider's group reported the synthesis of bare Mn:ZnSe and core/shell Mn:ZnSe/ZnS d-dots using the nucleation-doping method [20]. Hydrated

$ZnSO_4.7H_2O$ and $Mn(OAc)_2.4H_2O$ were mixed with 3-mercaptopropionic acid and NaHSe at room temperature followed by the growth of the doped core at 100 °C for 24 h. The ZnS shell was deposited following a thermal decomposition of Zn^{2+}/ MPA complexes at 100 °C for 10 h. A 2.5-fold increase in the QY (from 3.5 to 9 %) as well as a 2.24-fold increase in the emission lifetimes of Mn^{2+} ions (from 0.62 to 1.32 ms) were observed after overgrowing the doped core with a ZnS shell. These researchers also used ZnO shell to passivate the surfaces of 1-thioglycerol-capped Mn:ZnSe affording thioglycerol-capped Mn:ZnSe/ZnO culminating in an improvement in QY from 3.5 to 12 % [21].

4.1.2.2 Growth-doping method

In the growth-doping method, small host nuclei are first synthesized at the established reaction conditions. The temperature is then lowered and the dopant precursor solution is injected. After this injection, the temperature is raised to a level where doping takes place without the growth of the host [12]. Xue *et al.* [22] adopted the growth-doping method for the aqueous synthesis of MPA-stabilized Cu-doped ZnSe d-dots. Their QDs exhibited a red-shift in trap emission on doping with copper which shifted from 465 to 495 nm with prolonged reflux. The decay times of the Cu:ZnSe were longer than those of the undoped ZnSe and this was attributed to the participation of surface states in the carrier recombination process. The same type of d-dots has also been synthesized in an organic solvent 1-octadecene using octadecylamine as the surfactant [23]. On the one hand, the decay lifetimes of deep traps were prolonged upon copper-doping, while on the other hand the near-band edge and shallow traps were shortened. Highly luminescent Mn-doped ZnS d-dots have also been synthesized affording nanocrystals with high quantum yields (> 50 %) which were attributed to the fact that the non-emissive surface manganese ions were covered by an overgrown thin layer of ZnS [24]. This aqueous-based

growth-doping method was able to be scaled up to gram levels without loss of nanocrystal quality. Karan *et al.* [25] have reported the synthesis of d-dots of the type ZnE (E = S, Se), $ZnSe_{1-x}S_x$, $Cd_xZn_{1-x}S$ for both Mn- and Cu-dopants and CdS/ZnS (for Mn only) using manganese oxide and copper oxide nanocrystals as dopants. These dopant oxide nanocrystals were synthesized from the irreversible decomposition of their carboxylates in the presence of amines and free acids.

4.1.2.3 Isocrystalline core/shell synthetic method

This is yet another method of introducing dopant ions in QDs. Radovanovic and Gamelin developed an isocrystalline core/shell method that allows for the synthesis of internally doped Co^{2+}:CdS core/shell nanocrystals [13]. In this design, the core part of the nanocrystals consists of Co^{2+}:CdS while the shell consists of pure CdS. Using an inverted micelle coprecipitation method, the doped Co^{2+}:CdS nanocrystals were first synthesized from a room temperature reaction of two inverted micelle solutions, one containing $Cd(NO_3)_2$ and $Co(NO_3)_2$ and the other containing Na_2S. Additional amounts of $Cd(NO_3)_2$ and Na_2S were then alternately added to the nanocrystals affording the isocrystalline core/shell Co^{2+}: CdS. Using electronic absorption studies, they showed that the Co^{2+} ions substituted for the lattice Cd^{2+} ions. The subsequent growth of a pure CdS shell entrapped the surface bound Co^{2+} ions as illustrated in **Scheme 4.3**.

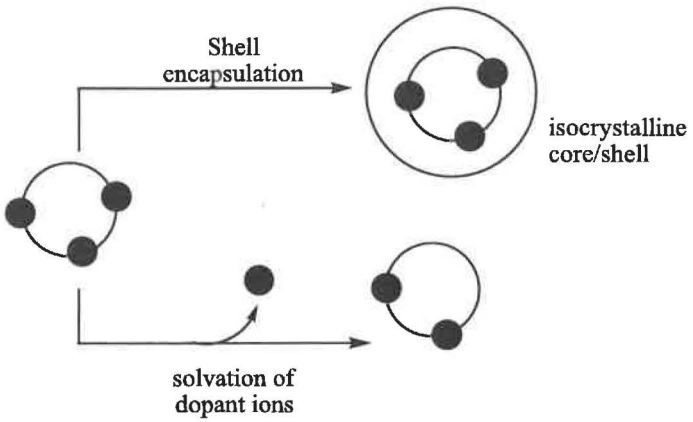

Scheme 4.3 Illustration of the isocrystalline core/shell Co^{2+}:CdS/CdS QDs. Large circles represent the boundaries of the CdS particles and the black dots represent the Co^{2+} dopant ions [13]

4.1.3 Mechanism of doping

The development of various strategies for the doping of semiconductor nanocrystals has advanced the synthetic chemistry aspects of d-dots. However, some limitations still exist in understanding the mechanism of the doping process. Knowledge of the mechanistic aspects of the doping process would confer the ability to precisely control the radial position of the dopants inside the nanocrystal lattice. In their work on Mn-doped CdS/ZnSe, Yang *et al.* [26] reported a three-step radial-position-controlled doping approach involving: i) synthesis of starting host CdS particles, ii) Mn-dopant growth and iii) host-shell growth (**Figure 4.1**). To effect Mn-doping, MnS shells were overgrown on the pure CdS cores. Subsequent host-shell growth was then carried out after removal of unreacted Mn-dopant species.

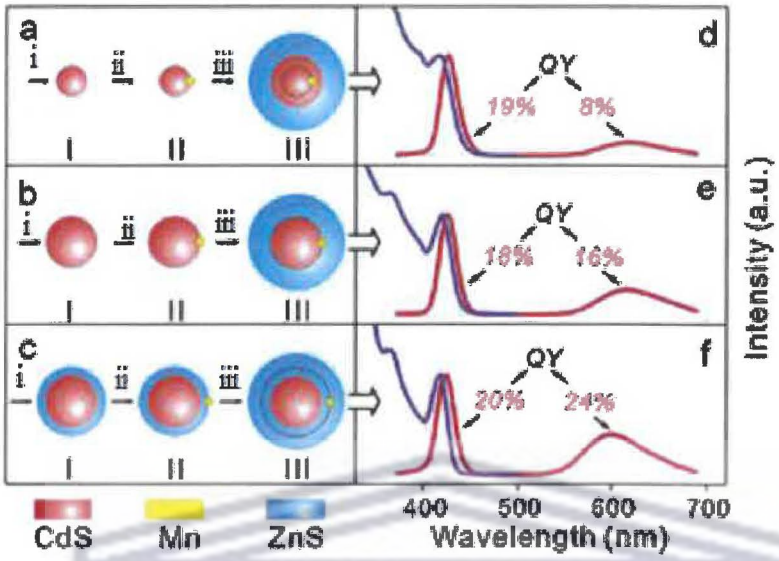

Figure 4.1 Model illustration of Mn-doped CdS/ZnS core/shell NCs with different Mn positions: a) inside the CdS core, b) at the core/shell interface and c) in the ZnS shell. Also shown are the PL (red) and PLE (blue) spectra of the core/shell NCs: d) IIIa, e) IIIb and f) IIIc (reprinted with permission from [26], Copyright 2006, American Chemical Society).

In 2005, Erwin *et al.* [1] showed that the mechanism that controls the doping efficiency was the initial adsorption of impurities on the surface of the QDs. The adsorption process was affected by surface morphology, nanocrystal shape and the surfactants in the growth solution. Chen *et al.* [27] identified four important processes in the doping mechanism which are surface adsorption, lattice incorporation, lattice diffusion and lattice ejection. The first two processes are associated with the growth-doping method while the last two are associated with the nucleation-doping method. In the growth-doping method, the dopant first adsorbs on the surface of the nanocrystals and then is incorporated into the host lattice. In the nucleation-doping method, lattice diffusion allows the dopant to diffuse into the host shell forming a doped interface where both energy transfer and dopant emission occur.

4.2 Results and discussion of synthesis and characterization of doped InP/ZnSe QDs

4.2.1 Synthesis and characterization of Ag-doped InP/ZnSe QDs

Fluorescent and monodisperse Ag:InP/ZnSe nanocrystals were synthesized following the growth-doping procedure using silver palmitate as the Ag precursor. While the nucleation step for the synthesis of small InP host nuclei was attained at 300 °C, their growth was achieved at about 270 °C using 1-octadecene as the non-coordinating solvent. The growth-doping step was effected at 210 °C using Ag-dopant levels of 0, 5 and 10 % with respect to moles of phosphorus in the InP core. At this temperature, only the doping process took place without the growth of the host InP nanocrystals. This doping temperature has also been used successfully in the doping of InP nanocrystals using copper as dopant [28].

4.2.1.1 Optical studies of Ag-doped InP/ZnSe QDs

The optical properties of Ag-doped InP/ZnSe were studied by photoluminescence spectroscopy. It was shown that the introduction of Ag dopant caused a red-shift in the emission spectra of InP/ZnSe nanocrystals. The emission peak positions were 592, 598 and 613 nm for Ag-dopant levels of 0, 5 and 10 %. **Figure 4.2** shows the PL spectra of Ag-InP/ZnSe nanocrystals. A similar red-shift was also reported by Banin and co-workers where they prepared Ag-doped InAs nanocrystals [29]. They reported that Ag^{+} ions, that are substitutional impurities (as opposed to interstitial impurities) in III-V semiconductors owing to their larger ionic radii (129 pm) than that of In^{3+} ions (94 pm), distort the crystal structure of the III-V systems leading to band-tailing and consequently to the red-shifting in the emission peak position. Evident also was the pronounced decrease in PL intensity with increasing Ag dopant levels (see **Figure 4.2**). Georgekutty *et al.*

[30] have reported similar Ag-dopant induced quenching of PL intensity in ZnO nanoparticles. The phenomenon was attributed to a decrease in electron-hole recombination.

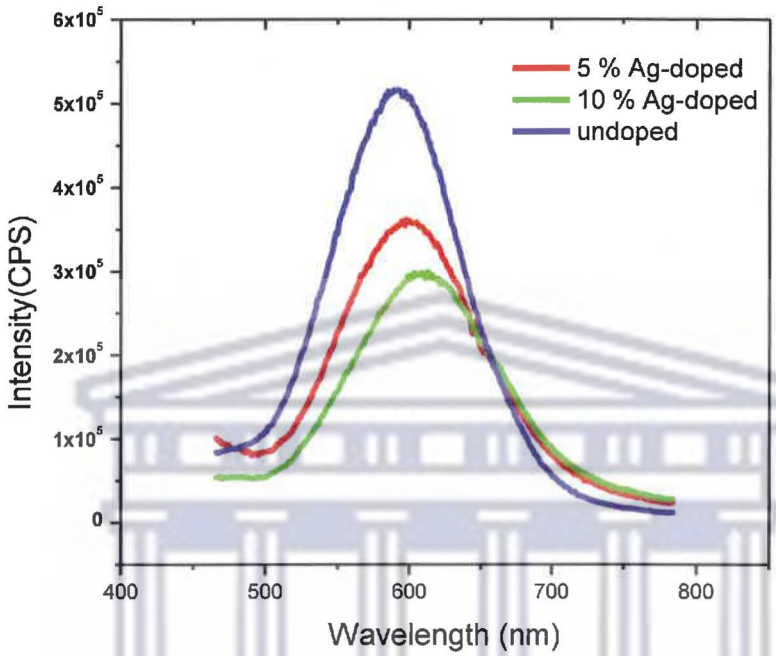

Figure 4.2 PL spectra of Ag-doped InP/ZnSe nanocrystals

4.2.1.2 TEM of Ag-doped InP/ZnSe QDs

Figure 4.3 shows the TEM micrographs of the Ag-doped InP/ZnSe nanocrystals and their respective particle size histograms. The micrographs for both 5 and 10 % Ag-doped InP/ZnSe nanocrystals exhibit lattice fringes indicating the good crystallinity of the nanocrystals. The particle sizes as determined by TEM were 3.26 and 3.73 nm for 5 and 10 % Ag-doped InP/ZnSe nanocrystals. To confirm the incorporation of Ag-dopant ions in the QDs, EDX analysis on the 10 % Ag-doped InP/ZnSe QDs was done. The EDX spectrum showed the presence of the presence of Ag dopant ions (**Figure 4.4**).

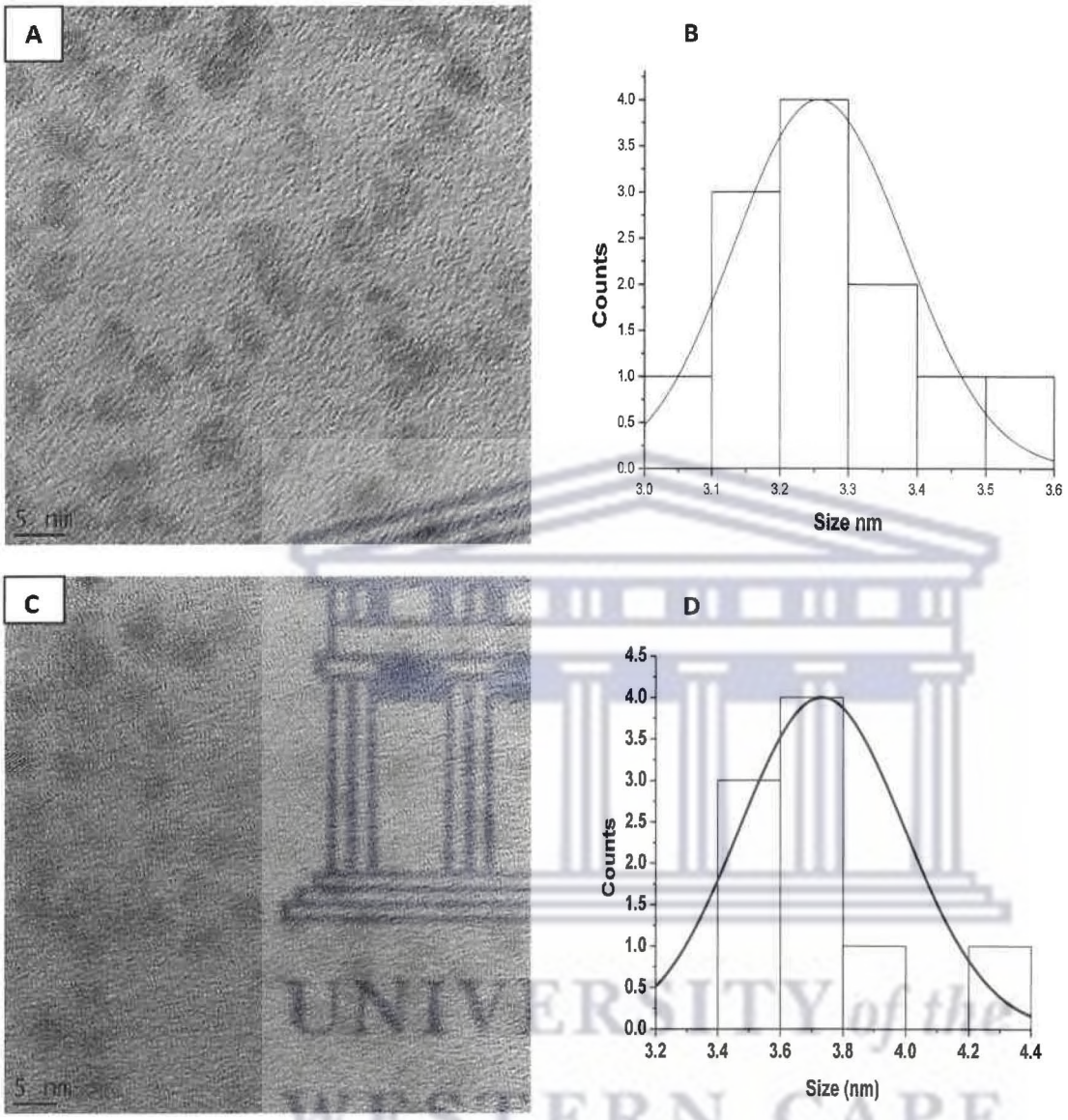

Figure 4.3 (**A**) TEM micrograph of 5 % Ag-doped InP/ZnSe, (**B**) Particle size distribution for the 5 % Ag-doping level, (**C**) TEM micrograph of 10 % Ag-doped InP/ZnSe and (**D**) Particle size distribution for the 10 % Ag-doping level.

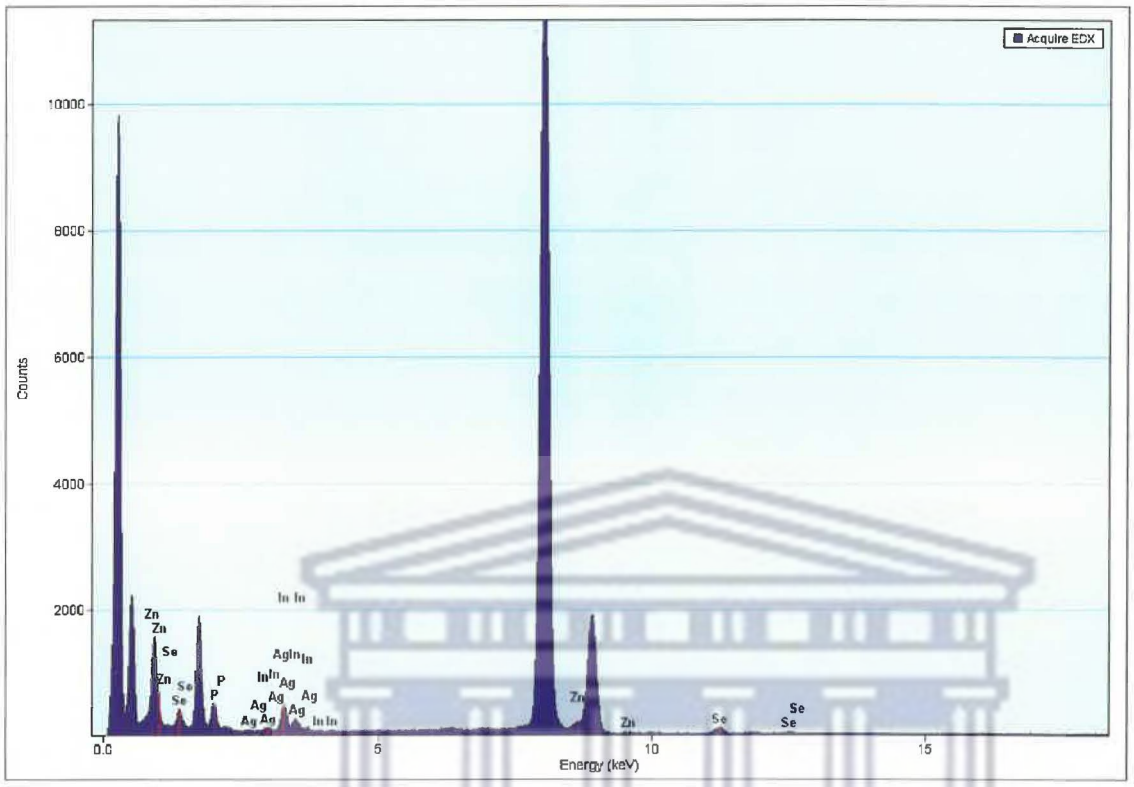

Figure 4.4 EDX spectrum of the 10 % Ag-doped InP/ZnSe nanocrystals

4.2.1.3 XRD of Ag-doped InP/ZnSe QDs

Figure 4.5 shows the XRD pattern for the Ag-doped InP/ZnSe nanocrystals. From the XRD diffractogram, three broad peaks with 2Θ values of 26.28°, 43.61° and 51.62° that correspond to <111>, <220> and <311> reflecting planes respectively proved that the Ag-doped InP/ZnSe nanocrystals maintained the cubic zinc blende structure as displayed by pure InP/ZnSe. Manganese-doped InP nanocrystals have also retained the cubic zinc blend structure [31]. **Figure 4.6** shows the XRD patterns for both undoped and Ag-doped InP/ZnSe nanocrystals. The Ag-dopant ions were incorporated in the InP/ZnSe lattice interstitially and not substitutionally. Incorporation of dopant ions into a crystal lattice via substitution has been reported to cause a

corresponding shift in the 2θ angles [31]. Where such shifts are absent, as in the case of Ag:ZnO, this has been interpreted to signify segregation of dopant ions in the grain boundaries of nanocrystal lattice. There were no characteristic peaks for silver impurity phases such as peaks at 38.2, 44.4, 64.4 and 77.3 corresponding to <111>, <200>, <220> and <311> planes respectively [32].

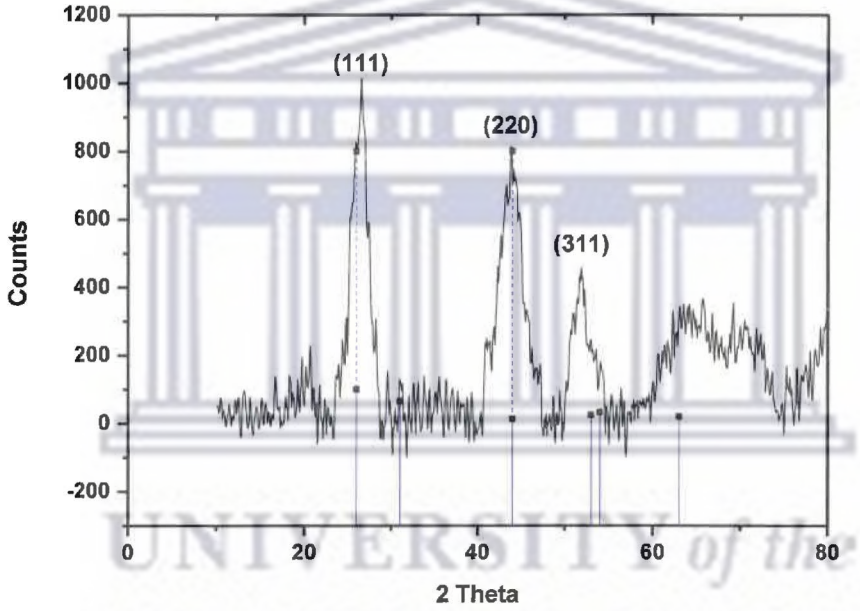

Figure 4.5 XRD pattern for 5 % Ag-doped InP/ZnSe nanocrystals

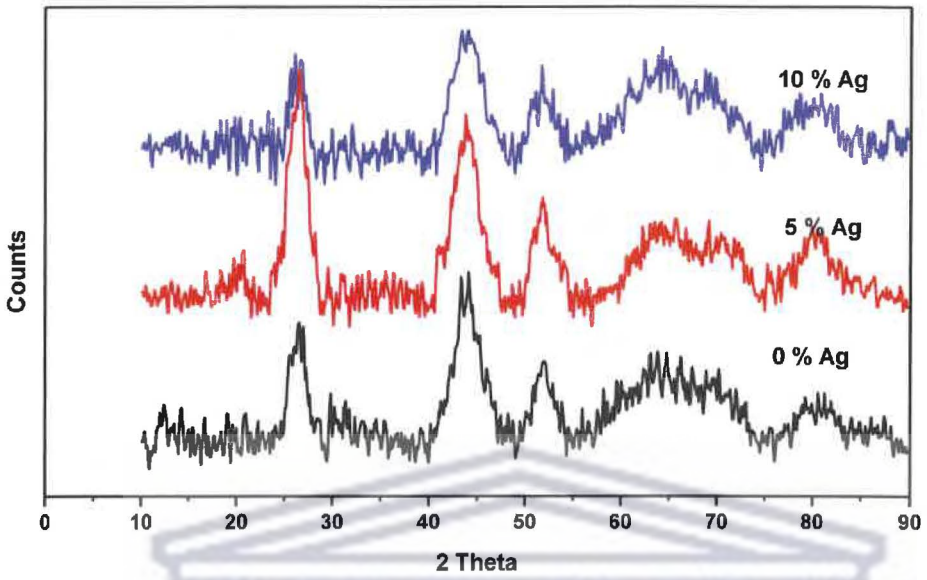

Figure 4.6 XRD diffractograms of 0, 5 and 10 % Ag-doped InP/ZnSe nanocrystals

4.2.2 Synthesis and characterization of Co-doped InP/ZnSe QDs

Co:InP/ZnSe nanocrystals were synthesized following the growth-doping procedure using cobalt(II) palmitate the Co precursor. The reaction conditions were similar to the procedure above for the synthesis Ag:InP/ZnSe nanocrystals. Other doping methods which have been used on cobalt doping of nanocrystals are the nucleation-doping method (for the synthesis of Co^{2+}-doped $Cd_{1-x}Zn_xSe$) [33] and isocrystalline core/shell doping method (for the synthesis of Co^{2+}:ZnO) [34]. For example, in the synthesis of Co^{2+}-doped $Cd_{1-x}Zn_xSe$ using the nucleation-doping method, a cationic solution was prepared in 1-octadecene using zinc oxide, cadmium oxide and cobalt acetate tetrahydrate as precursors. The selenium precursor, tributylphosphine-selenium, was added at the nucleation temperature of 310 °C and reaction was stabilized at 270–300 °C for several hours to allow for alloying to take place affording the doped QDs [33].

4.2.2.1 Optical Studies of Co-doped InP/ZnSe QDs

Figure 4.7 shows the PL spectra of cobalt doped InP/ZnSe nanocrystals. The doping levels used were 15 and 20 mol % cobalt with respect to phosphorus. Doping with cobalt showed that there was no change in the emission position. The FWHM were 111 and 121 nm for the 15 and 20 % dopant levels respectively showing an increase in the size distribution with increase in dopant level. **Figure 4.8** shows a decrease in fluorescence intensity with increase in doping level from 15 to 20 %. The same observation was made by Vatankhah *et al.* [35] when they reported that the quenching point for Co:ZnS nanocrystals was 0.1 % of the dopant with increase in the level of cobalt impurity to 5 % resulting in continued decrease in fluorescence signal. For Co:CdS nanocrystals, the emission intensity decreased for 6 % dopant level and this was attributed to evenly dopant incorporation in the CdS nanocrystals [36]. Peng *et al.* [37] have also reported the suppression of exciton emission with increasing Co dopant levels in ZnO systems. They ascribed this to an increase in the distortion of host lattice and defects as more dopant ions displaced host cations.

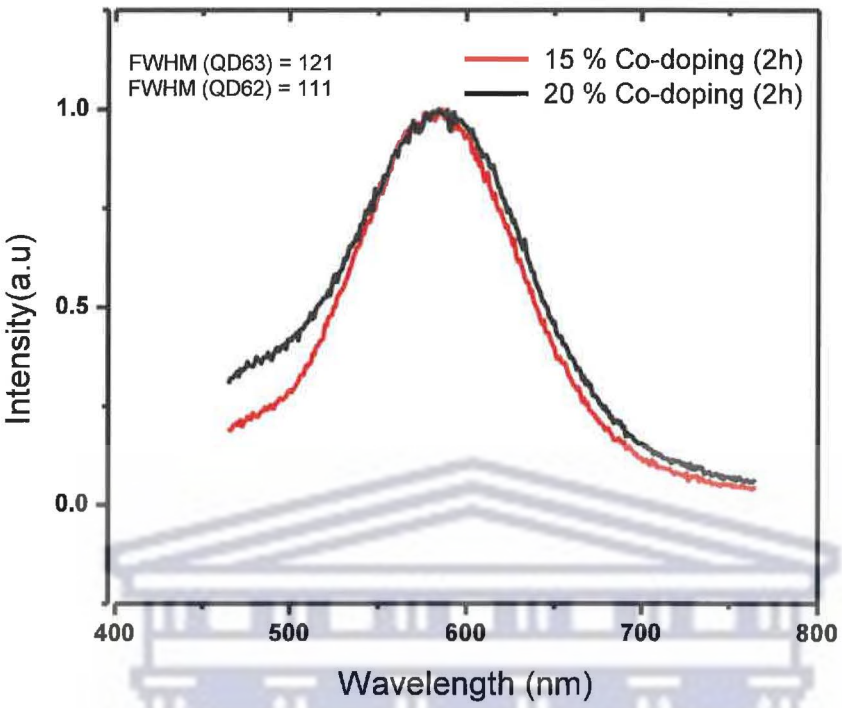

Figure 4.7 Normalized PL spectra of Co-doped InP/ZnSe nanocrystals

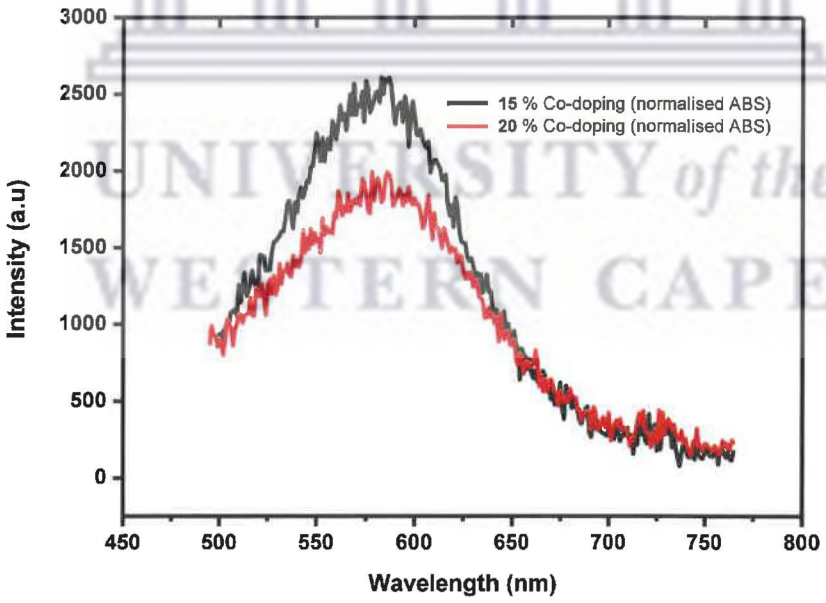

Figure 4.8 Normalized fluorescence intensity values of Co-doped InP/ZnSe nanocrystals

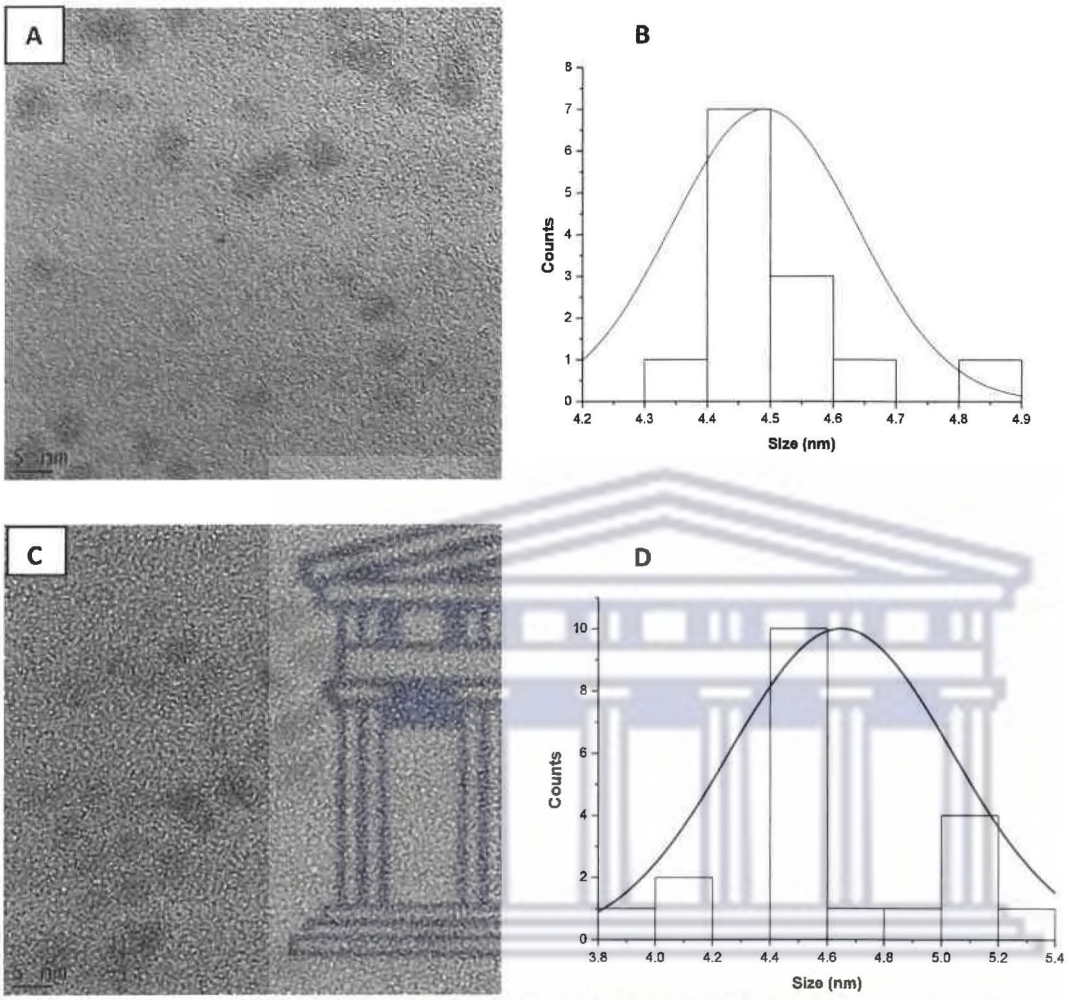

Figure 4.9 (**A**) TEM micrograph of 15 % Co-doped InP/ZnSe, (**B**) Particle size distribution for the 15 % Co-doping level, (**C**) TEM micrograph of 20 % Co-doped InP/ZnSe and (**D**) Particle size distribution for the 20 % Co-doping level.

4.2.2.2 TEM of Co-doped InP/ZnSe QDs

Co:InP/ZnSe nanocrystals were also characterized using HRTEM. **Figures 4.9** (**A**) and (**C**) show the TEM micrographs that also exhibit good crystallinity of the nanocrystals based on the lattice fringes. **Figures 4.9** (**B**) and (**D**) show the particle size distribution histograms for the Co:InP/ZnSe nanocrystals. The particle sizes as calculated from TEM were 4.49 and 4.63 nm for

15 and 20 % doping levels respectively. The elemental composition of the Co-doped InP/ZnSe QDs was confirmed using EDX analysis (**Figure 4.10**).

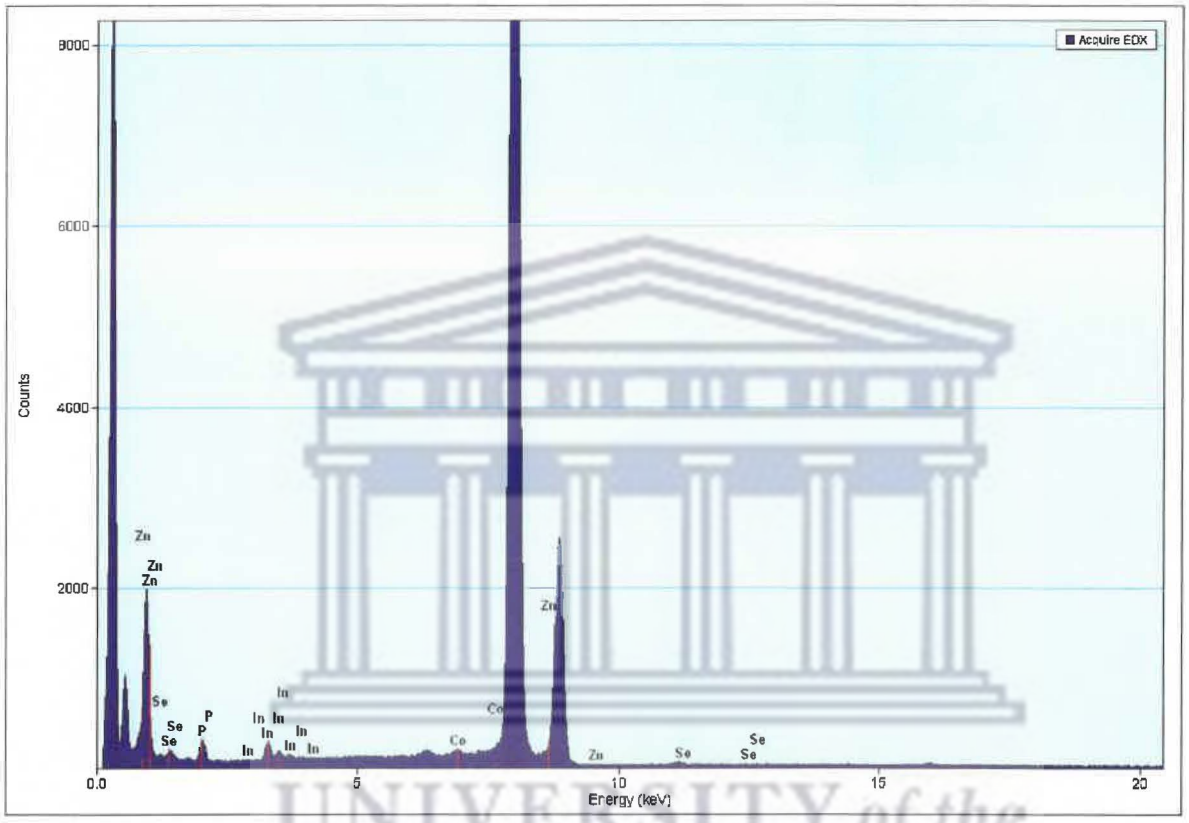

Figure 4.10 EDX spectrum of 20 % Co-doped InP/ZnSe nanocrystals

4.2.2.3 XRD of Co-doped InP/ZnSe QDs

The crystallinity and phase of Co-doped InP/ZnSe nanocrystals were also characterized using XRD as displayed in **Figures 4.11** and **4.12**. Once again, the peak positions indicated the zinc blende crystal structure was retained after doping and that there were no cobalt nanocrystal impurity phases observed [38].

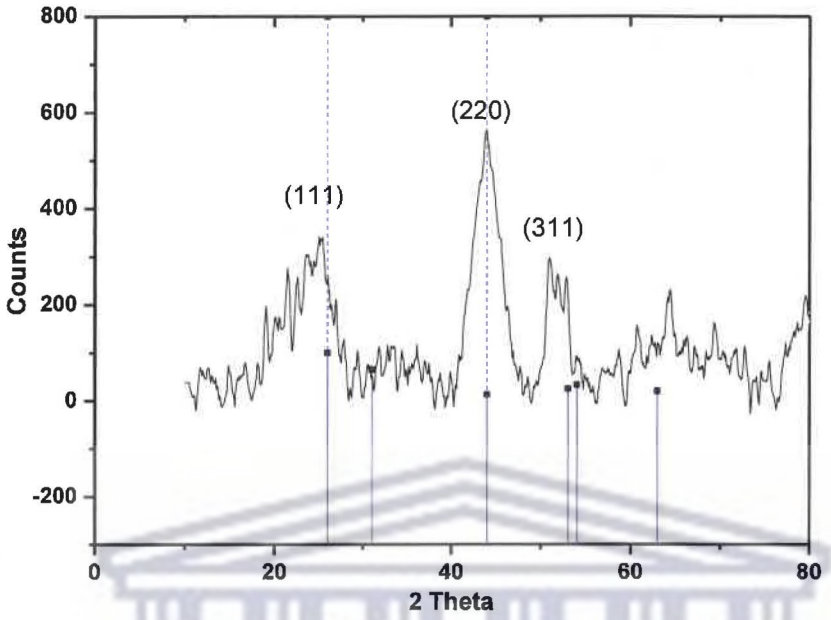

Figure 4.11 XRD pattern for 20 % Co-doped InP/ZnSe nanocrystals

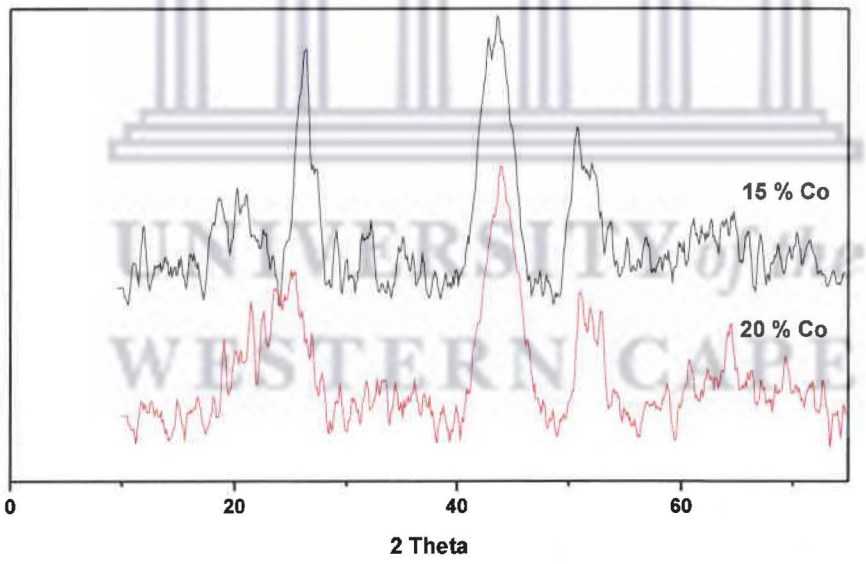

Figure 4.12 XRD diffractograms of 15 (black) and 20 % (red) Co-doped InP/ZnSe nanocrystals

4.2.3 Synthesis and characterization of Fe-doped InP/ZnSe QDs

4.2.3.1 Optical studies of Fe-doped InP/ZnSe QDs

Figure 4.13 shows the normalized fluorescence intensity of Fe:InP/ZnSe nanocrystals. The PL spectra of Fe-doped InP/ZnSe nanocrystals exhibited a blue shift with increase in dopant level from 1 % to 5 %. The emission peaks were 592 and 566 nm for the Fe dopant levels of 1 and 5 % respectively. A similar blue shift was observed by Yang *et al.* [39] when they fabricated Fe:ZnSe QDs. However, these researchers attributed the blue shift to a decrease in reaction rate with the incorporation of the dopant ions which was confirmed by nanoparticle size reduction and hence band gap increase. There was no significant difference in the FWHM for the two levels of dopant FWHM of 104 and 101 nm for Fe dopant levels of 1 and 5 % respectively.

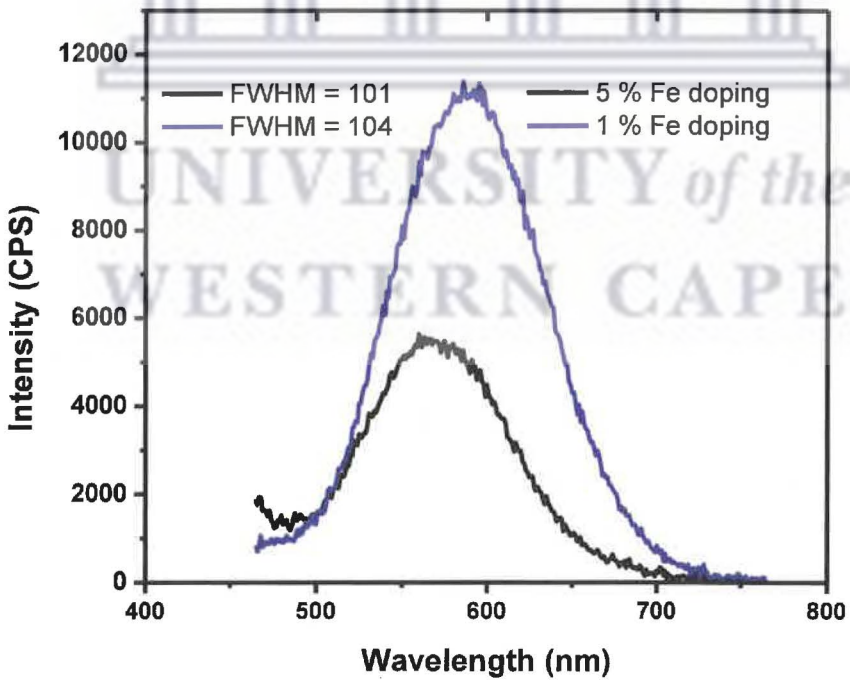

Figure 4.13 Normalized fluorescence intensity values of Fe-doped InP/ZnSe nanocrystals

A decrease in emission intensity was observed with increase in dopant level from 1 to 5 % showing that the iron dopant acted to quench the fluorescence from InP core. Selmani *et al.* [40] ascribed the quenching effect of iron in Fe-doped ZnS to the trapping of electrons by Fe centres culminating in non-radiative recombination of excitons.

4.2.3.1 TEM of Fe-doped InP/ZnSe QDs

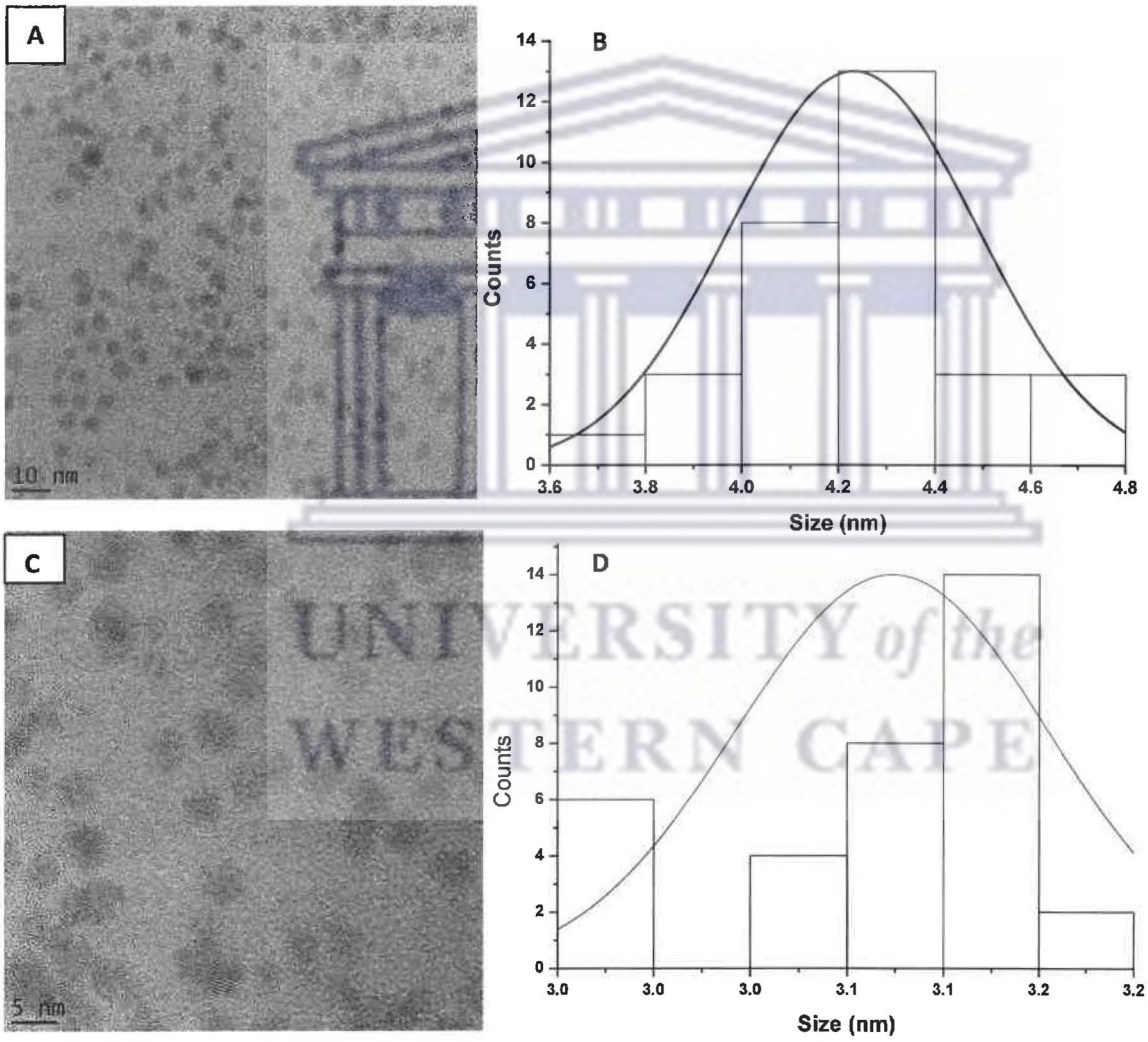

Figure 4.14 (**A**) TEM micrograph of 5 % Fe-doped InP/ZnSe, (**B**) Particle size distribution for the 5 % Fe-doping level, (**C**) TEM micrograph of 1 % Fe-doped InP/ZnSe and (**D**) Particle size distribution for the 1 % Fe-doping level.

Figure 4.14 shows the TEM micrographs particle size distribution histograms of the iron doped InP/ZnSe nanocrystals. The calculated particles sizes are 4.23 and 3.12 nm for the 5 and 1 % dopant levels. The elemental analysis of the 5 % Fe-doped InP/ZnSe QDs using EDX (**Figure 4.15**) confirmed the presence of Fe-dopant in the sample.

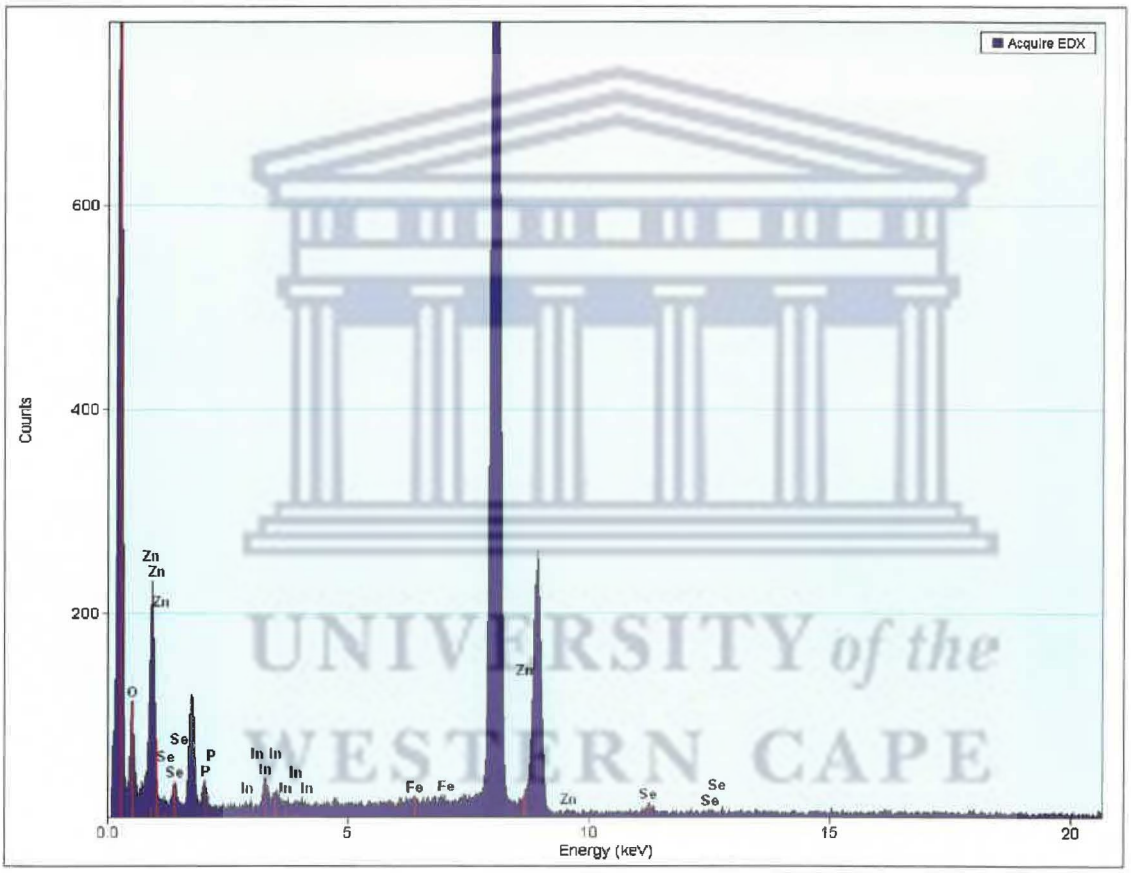

Figure 4.15 EDX spectrum of 5 % Fe-doped InP/ZnSe nanocrystals

4.2.3.2 XRD of Fe-doped InP/ZnSe QDs

Figure 4.16 shows the XRD diffractogram of 1 % Fe-doped InP/ZnSe nanocrystals. The zinc blende structure is maintained. Parra-Palomino *et al.* [41] have reported that for Fe-doped ZnO, the XRD peaks for different concentrations of the dopant and aging times corresponded to the wurtzite structure of the pure ZnO nanocrystals.

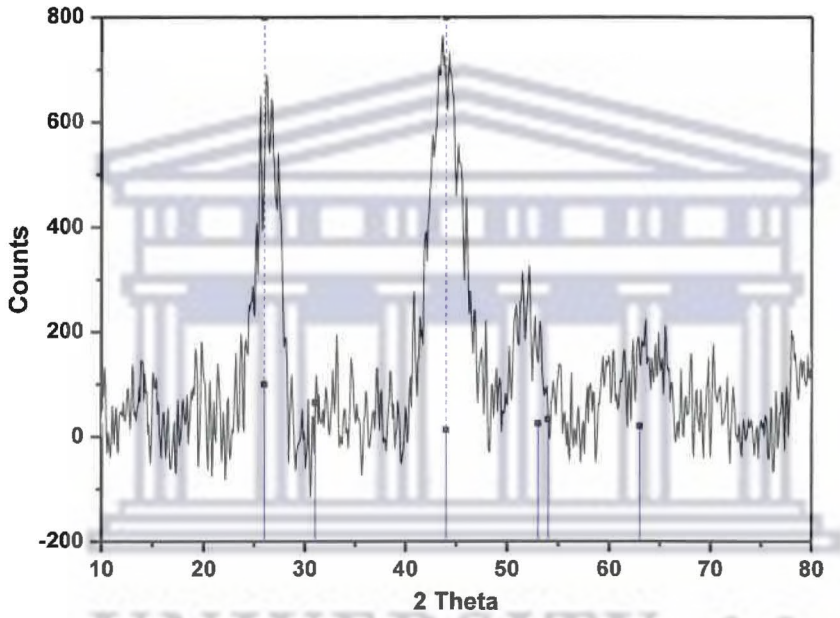

Figure 4.16 XRD pattern for 1 % Fe-doped InP/ZnSe nanocrystals

4.2.4 Ligand exchange reactions using 3-mercaptopropionic acid

The as-prepared transition metal-doped InP/ZnSe nanocrystals were capped with a layer of palmitic acid making them dispersible only in non-polar solvents such as hexane and chloroform. Therefore ligand exchange reactions were imperative in order to render the nanocrystals water-dispersible and hence amenable with bioimaging or biomedical applications. Various ligands have been used for the phase transfer of indium phosphide-based nanocrystals into the aqueous medium. Bharali *et al.* [42] used mercaptoacetic acid for surface modification of InP/ZnS

nanocrystals. Other ligands that have been used with InP-based nanocrystals include thioglycolic acid [43], mercaptosuccinic acid [44], dihydrolipoic acid (DHLA) [45] and 3-mercaptopropionic acid [46].

The ligand 3-mercaptopropionic acid was used as the bifunctional ligand for the modification of doped InP/ZnSe nanocrystals. The thiol and carboxylic acid moieties are used for anchoring to the surface of the nanocrystal and bioconjugation to biological molecules respectively. **Scheme 4.4** provides a schematic representation of the phase transfer process. The optical properties of the aqueous phase-dispersed nanocrystals were studied by photoluminescence spectroscopy.

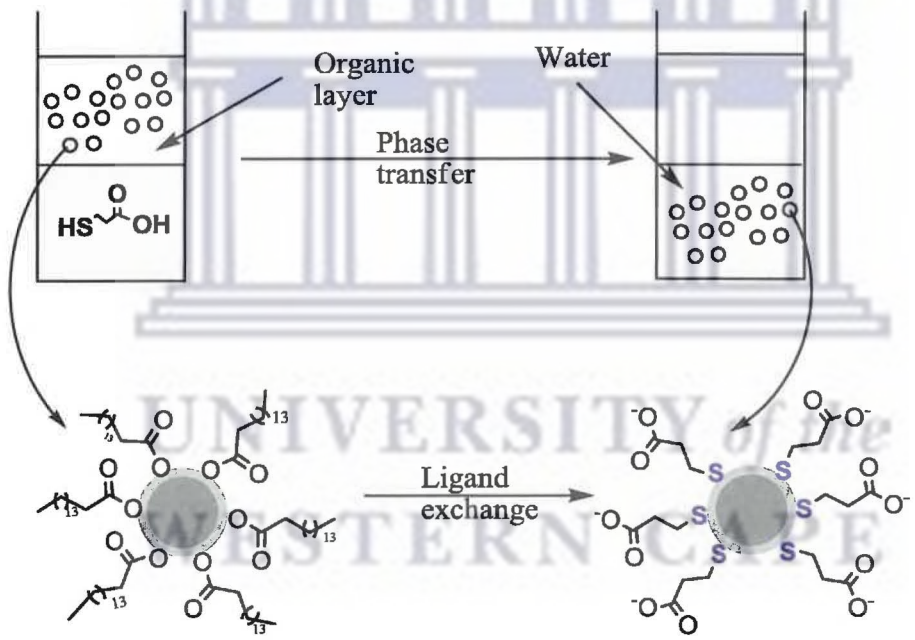

Scheme 4.4 Pictorial representation of the phase transfer process

4.2.4.1 Optical studies of MPA-capped doped-InP/ZnSe QDs

Figures 4.17 and **4.18** show the emission profiles of Co- and Ag-doped InP/ZnSe nanocrystals before and after phase transfer.

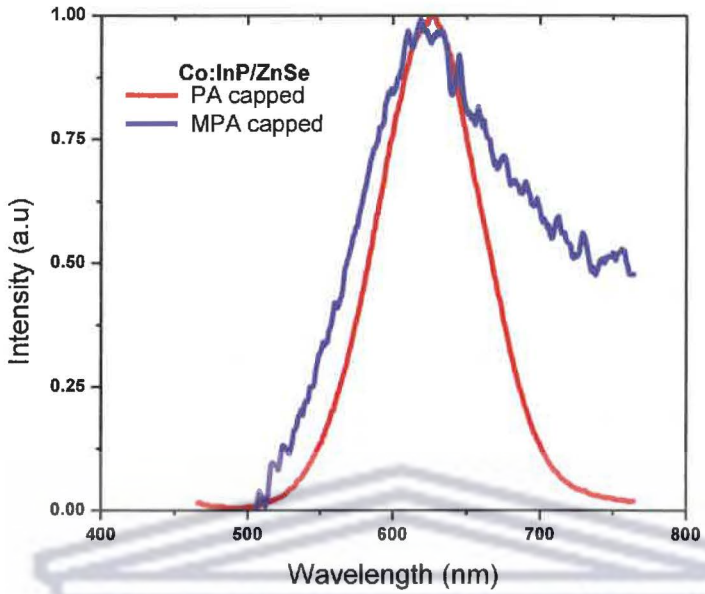

Figure 4.17 Normalized PL spectra of palmitic acid- (red) and MPA-capped (blue) Co:InP/ZnSe nanocrystals

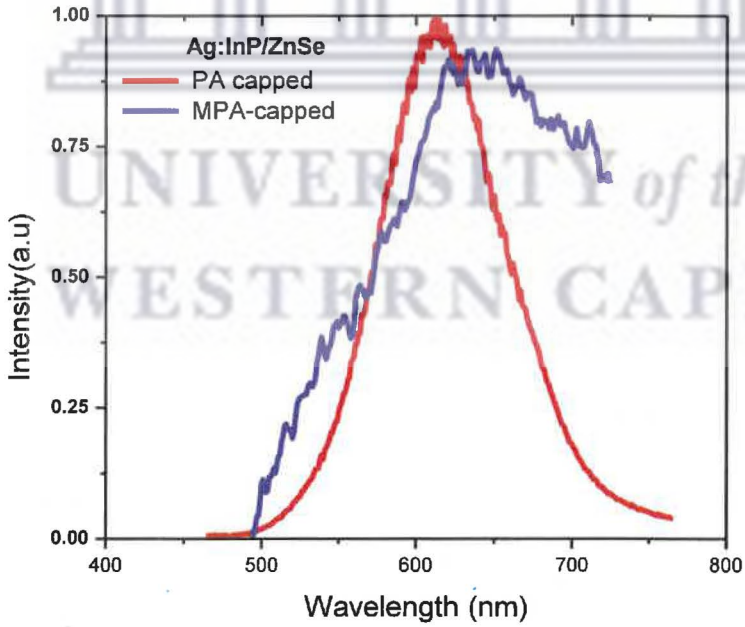

Figure 4.18 Normalized PL spectra of palmitic acid- (red) and MPA-capped (blue) Ag:InP/ZnSe nanocrystals

There was no change in the emission peak position after ligand exchange for these systems. However, a decrease in the photoluminescence intensity was observed in both cases. The quenching of photoluminescence intensity on ligand exchange has been reported in literature [47]. This quenching phenomenon has been attributed to the hole-trapping capacity of thiol groups [48].

4.3 Conclusions

Transition metal (Ag, Fe, and Co) doped InP/ZnSe nanocrystals were successfully synthesized following the growth doping method. In all the experiments, high quality nanocrystals were obtained as exhibited by their TEM micrographs. All the doped nanocrystals exhibited a d fluorescence quenching effect which was attributed to a decrease in electron-hole recombination with increasing dopant levels.

Ligand exchange reactions were successfully carried out as exemplified by phase transfer of Co- and Fe-doped InP/ZnSe nanocrystals. As a result of the displacement of the native palmitic acid capping layer by 3-mercaptopropionic acid, a decrease in PL intensity was observed which was ascribed to the hole-trapping ability of thiol groups.

4.4 References

1 Erwin SC, Zu L, Haftel MI, Efros AL, Kennedy TA, Norris DJ, *Nature,* **2005**, *436, 91*

2 Stowell CA, Wiacek RJ, Saunders AE, Korgel BA, *Nano Lett.*, **2003**, *3, 1441*

3 Lommens P, Loncke F, Smet PF, Callens F, Poelman D, Vrielinck H, Hens Z, *Chem. Mater.*, **2007**, *19,* 5576

4 Bera D, Qian L, Tseng T-K, Holloway PH, *Materials* **2010**, *3, 2260*

5 Bhargava RN, *J. Lumin.*, **1996**, *70, 85594.*

6 Begum R, Chattopadhyay A, *Langmuir,* **2011**, *27, 6433*

7 Bhargava RN, Gallagher D, Hong X, Nurmikko A, *Phys. Rev. Lett.*, **1994**, *72, 416*

8 Dalpian GM, Chelikowsky JR, *Phys. Rev. Lett.*, **2006**, *96, 226802*

9 Norris DJ, Efros AL, Erwin SC, *Science,* **2008**, *319, 1776*

10 Deng Z, Tong L, Flores M, Lin S, Cheng J-X, Yan H, Liu Y, *J. Am. Chem. Soc.*, **2011**, *133, 5389*

11 Oo WMH, McCluskey MD, Huso J, Morrison JL, Bergman L, Engelhard MH, Saraf LV, *J. Appl. Phys.*, **2010**, *108, 064301*

12 Pradhan N, Goorskey D, Thessing J, Peng X, *J. Am. Chem. Soc.*, **2005**, *127, 17586*

13 Radovanovic PV, Gamelin DR, *J. Am. Chem. Soc.*, **2001**, *123, 12207*

14 Pradhan N, Peng X, *J. Am. Chem. Soc.*, **2007**, *129, 3339*

15 Gan C, Xiao M, Battaglia D, Pradhan N, Peng X, *Appl. Phys. Lett.*, **2007**, *91, 201103*

16 Zheng J, Yuan X, Ikezawa M, Jing P, Liu X, Zheng Z, Kong X, Zhao J, Masumoto Y, *J. Phys. Chem. C,* **2009**, *113, 16969*

17 Wang C, Gao X, Ma Q, Su X, *J. Mater. Chem.*, **2009**, *19, 7016*

18 Shao P, Zhang Q, Li Y, Wang H, *J. Mater. Chem.*, **2011**, *21, 151*

19 Fang Z, Wu P, Zhong X, Yang Y-J, *Nanotechnology,* **2010**, *21, 305604*

20 Aboulaich A, Geszke M, Balan L, Ghanbaja J, Medjahdi G, Schneider R, *Inorg. Chem.*, **2010**, *49, 10940*

21 Aboulaich A, Balan L, Ghanbaja J, Medjahdi G, Merlin C, Schneider R, *Chem. Mater.*, **2011**, *23, 3706*

22 Xue G, Chao W, Lu N, Xingguang S, *J. Lumin.*, **2011**, *131, 1300*

23 Gul S, Cooper JK, Corrado C, Vollbrecht B, Bridges F, Guo J, Zhang JZ, *J. Phys. Chem. C*, **2011**, *115, 20864*

24 Srivastava BB, Jana S, Karan NS, Paria S, Jana NR, Sarma DD, Pradhan N, *J. Phys. Chem. Lett.*, **2010**, *1, 1454*

25 Karan NS, Sarma DD, Kadam RM, Pradhan N, *J. Phys. Chem. Lett.*, **2010**, *1, 2863*

26 Yang Y, Chen O, Angerhofer A, Cao YC, *J. Am. Chem. Soc.*, **2006**, *128, 12428*

27 Chen D,Viswanatha R, Ong GL, Xie R, Balasubramaninan M, Peng X, *J. Am. Chem. Soc.*, **2009**, *131, 9333*

28 Xie R, Peng X, *J. Am. Chem. Soc.*, **2009**, *131, 10645*

29 Mocatta D, Cohen G, Schattner J, Millo O, Rabani E, Uri Banin U, *Science*, **2011**, *332, 77*

30 Georgekutty R, Seery MK, Pillai SC, *J. Phys. Chem. C*, **2008**, *112, 13563*

31 Sahoo Y, Poddar P, Srikanth H, Lucey DW, Prasad PN, *J. Phys. Chem. B*, **2005**, *109, 15221*

32 Khan MAM, Kumar S, Ahamed M, Alrokayan SA, AlSalhi MS, *Nanoscale Res. Lett.*, **2011**, *6, 434*

33 Santangelo SA, Hinds EA, Vlaskin VA, Archer PI, Gamelin DR, *J. Am. Chem. Soc.* **2007**, *129, 3973*

34 Radovanovic PV, Norberg NS, McNally KE, Gamelin DR, *J. Am. Chem. Soc.* **2002**, *124, 15192*

35 Vatankhah C, Yuosefi MH, Khosravi AA, Savarian M, *Eur. Phys. J. Appl. Phys.* **2009**, *48, 20601*

36 Saravanan L, Pandurangan A, Jayavel R, *J. Nanopart. Res.*, **2011**, *13, 1621*

37 Peng YZ, Liew T, Song WD, An CW, Teo KL, Chong TC, *J. Supercond.*, **2005**, *18, 97*

38 Bao Y, Pakhomov AB, Krishnan KM, *J. Appl. Phys.*, **2005**, *97, 10J317*

39 Yang L, Zhu J, Xiao D, *RSC Adv.*, **2012**, *2,8179*

40 Selmani S, Abdullah H, Shaari S, Abd-Shukor R, *Funct. Mater. Lett.*, **2011**. *4, 101*

41 Parra-Palomino A, Perales–Perez O, Singha R, Tomar M, Hwang J, Voyles PM, *J. Appl. Phys.*, **2008**, *103, 07D121*

42 Bharali DJ, Lucey DW, Jayakumar H, Pudavar HE, Prasad PN, *J. Am. Chem. Soc.* **2005**, *127, 11364*

43 Li C, Ando M, Enomoto H, Murase N, *J. Phys. Chem. C,* **2008**, *112, 20190*

44 Yong K-T, Ding H, Roy I, Law W-C, Bergey EJ, Maitra A, Prasad PN, *ACS Nano,* **2009**, *3, 502*

45 Hussain S, Won N, Nam J, Bang J, Chung H, Kim S, *ChemPhysChem.*, **2009**, *10, 1466*

46 Chibli H, Carlini L, Park S, Dimitrijevic NM, Nadeau JL, *Nanoscale,* **2011**,*3, 2552*

47 de Mello Donega C, *Chem. Soc. Rev.*, **2011**, *40, 1512*

48 Bullen C, Mulvaney P, *Langmuir,* **2006**, *22, 3007*

CHAPTER 5: CYTOTOXICITY AND CELLULAR INTERNALIZATION STUDIES

5.1 Cytotoxicity Studies

5.1.1 Introduction

The application of QDs in biological systems requires not only water compatibility, but also low levels of cytotoxicity [1]. QDs affect cell proliferation and viability in variable ways in different cell types [2]. These variations have been attributed to both physicochemical properties and the environmental conditions of the QDs (**Section 1.10**). *In vitro* toxicity assays used to determine cytotoxicity or viability make use of colorimetric or fluorescent dyes to assess cell metabolism (e.g. MTT assay) or cell membrane integrity (e.g. trypan blue) [3]. The MTT assay measures the mitochondrial activity of live cells through the enzymatic reduction (succinate dehydrogenase) of a yellow tetrazolium salt, 3-(4,5-dimethylthiazol-2-yl)2,5-diphenyltetrazolium bromide (MTT), to a purple colored formazan crystal [4].

5.1.2 Cytotoxicity studies of MPA-capped InP/ZnSe QDs

The cytotoxicity of the InP/ZnSe nanocrystals was evaluated using the MTT assay. *In vitro* cytotoxicity studies were carried out in order to compare the cytotoxicity of indium– and cadmium–based QDs. To this end, both InP/ZnSe and CdTe/ZnS QDs were synthesized and capped with 3-mercaptopropionic acid (**Sections 2.3.3.4** and **2.3.4.1**). **Figure 5.1** shows the

normalized PL spectra of the MPA-capped InP/ZnSe and CdTe/ZnS QDs. The emission peak positions were 553 and 629 nm respectively for CdTe/ZnS and InP/ZnSe QDs respectively.

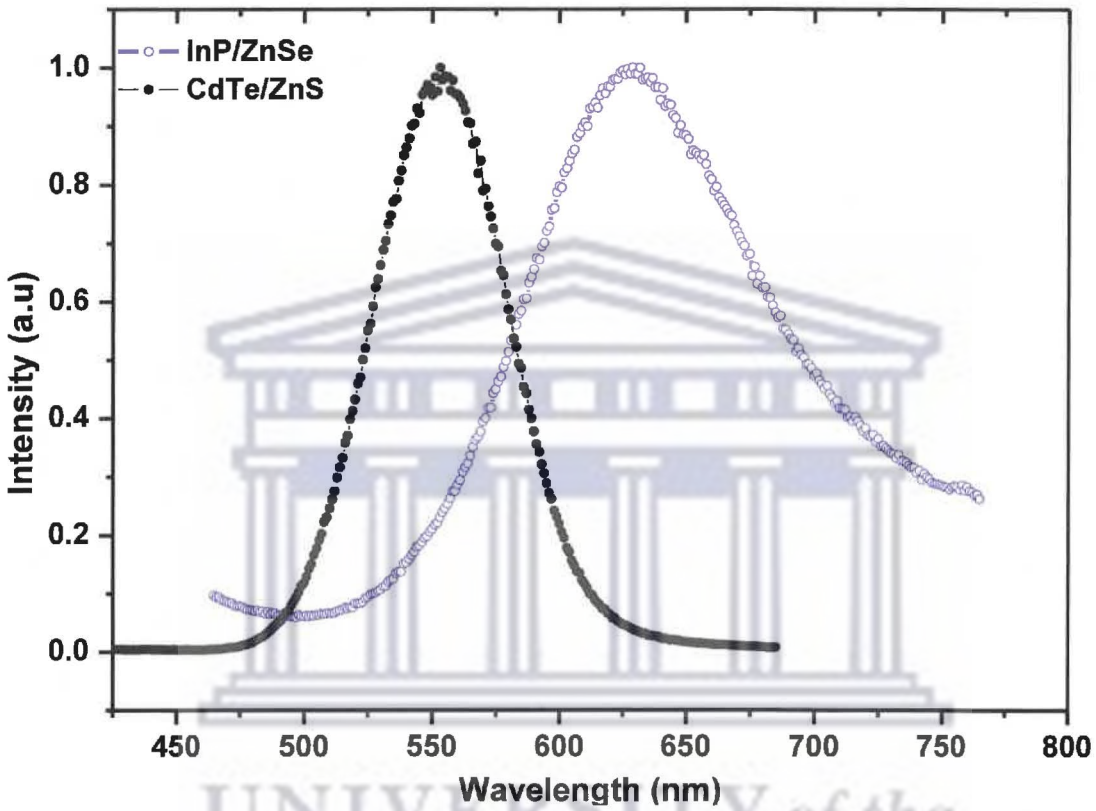

Figure 5.1 Normalized PL spectra of MPA-capped InP/ZnSe and CdTe/ZnS NCs

Having the same carboxylic acid terminated ligand surface layer ensured that any differences in cell viability would be attributed to the composition of the individual QDs. Erogbogbo *et al.* [5] adopted a similar approach when they compared the cytotoxicity of Si QDs with cadmium-based QDs CdTe and CdHgTe. Caco-2 cells were treated for 24 h with different concentrations of

both InP/ZnSe and CdTe/ZnS nanocrystals – from 0 to 500 µg/mL in order to compare the effects of indium- and cadmium based nanocrystals.

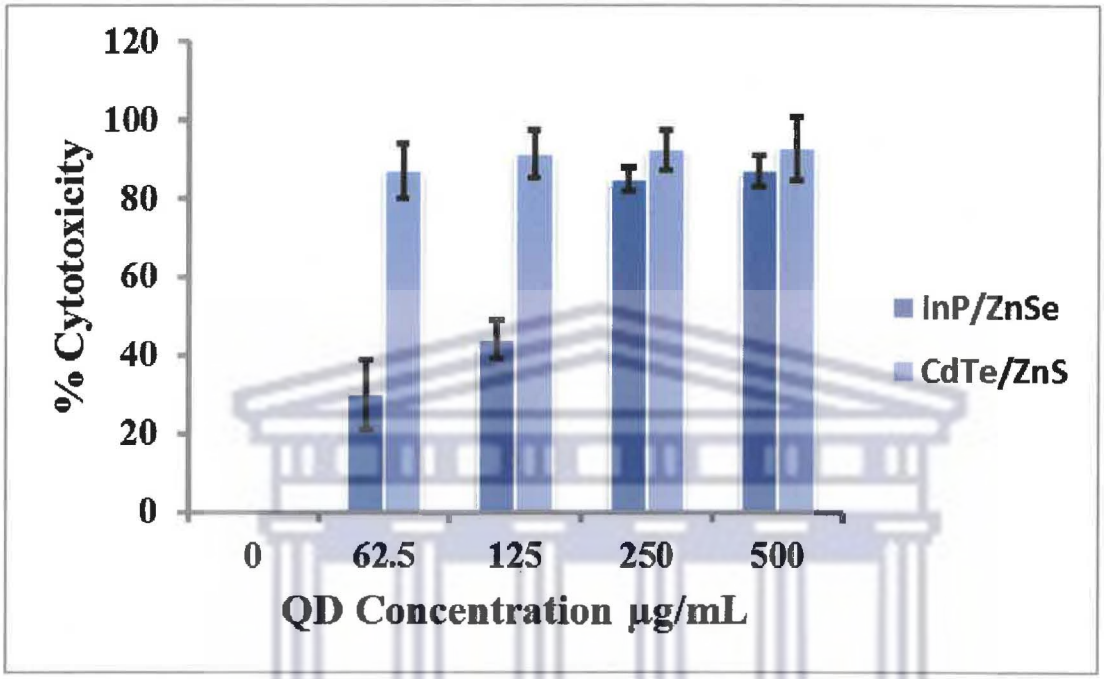

Figure 5.2 Cytotoxicity of MPA-capped InP/ZnSe and CdTe/ZnS using MTT assay

Figure 5.2 shows the cytotoxicity of both the indium- and cadmium-based QDs. The results showed that at a concentration of 125 µg/mL of InP/ZnSe QDs, less than 50 % of cell death had occurred while more than 80 % of cell death had occurred for an even lower concentration (62.5 µg/mL) of CdTe/ZnS QDs.

The data showed that indium-based QDs are less toxic compared to cadmium-based ones. Prasad's group also reported that cadmium-based QDs (CdTe and CdHgTe) were also more toxic than Si QDs with inhibitory particle concentrations (IC_{50}) corresponding to 50 % viability which were <25 µg/mL for the two cadmium-based QDs and >500 µg/mL for Si QDs [5].

5.2 Cellular internalization of TAT-InP/ZnSe QDs

5.2.1 Introduction

As discussed in **Section 1.9.1.2** of **Chapter 1**, active targeting is one of the numerous modes used for delivering QDs into cells. The use of cell penetrating peptides (CPPs) or protein transduction domains (PTDs) dates back to 1988 when Frankel and Pabo reported that transcription transactivating (TAT) protein from HIV-1 entered cells and translocated into the nucleus [6]. The CPPs are short cationic peptides of less than 30 amino acids derived either from proteins or chimeric sequences [7]. TAT is the most commonly used CPP for the delivery of a varied range of cargos into cells owing to its outstanding delivery efficiency and reduced cytotoxicity [8]. Therefore, internalization of TAT peptide–conjugated InP/ZnSe QDs into Caco-2 cells was studied using fluorescence microscopy.

5.2.2 Results and discussion of TAT bioconjugation to InP/ZnSe QDs and cellular studies

5.2.2.1 TAT peptide bioconjugation to InP/ZnSe QDs

The TAT peptide used in this work was expressed and purified at the Biotechnology Department, University of the Western Cape. The bioconjugation of MPA-capped InP/ZnSe QDs to TAT peptide through a covalent bond was achieved via the EDC coupling mechanism (**Section 2.3.4.2**). The cleaved TAT peptide had a free amine functional group that reacted with carboxylic

acid groups on QD surface forming an amide bond. The mechanism for the coupling reaction is described in **Section 1.8.2.1** of **Chapter 1**.

5.2.2.2 Cellular internalization of TAT-InP/ZnSe and fluorescence imaging

Caco-2 cells were treated as described in **Section 2.3.4.4**. **Figure 5.3** illustrates fluorescence microscope images of the treated and untreated Caco-2 cells. The untreated cells (**Figures 5.3 A**, **B** and **C**) were imaged as negative controls and they showed no fluorescence signal. **Figures 5.3 D**, **E** and **F** show strong fluorescence signal indicating cellular internalization of the TAT-InP/ZnSe QD bioconjugates. However, no signal was observed in the case of Caco-2 cells treated with unconjugated InP/ZnSe QDs (**Figures G**, **H** and **I**). The result demonstrated the efficiency of TAT peptide in delivering InP/ZnSe QDs inside Caco-2 cells.

Yong *et al.* [9] have also reported a similar labeling pattern using anticlaudin 4 and antiprostate stem cell antigen conjugated InP/ZnS QDs to label pancreatic cancer cell line (MiaPaCa). They observed robust fluorescence signals from MiaPaCa cells treated with antibody-InP/ZnS bioconjugates, while the cells treated with the unconjugated QDs showed little or no signal. Bharali *et al.* [10] have also used folate-decorated InP/ZnS QDs to demonstrate targeted receptor-mediated delivery of the QDs into the cancer cell line KB that overexpresses folate receptors. Various mechanisms have been proposed for the delivery of cargo-carrying TAT into cells. Early reports on TAT delivery mechanism claimed that the process was independent to endocytosis [11]. Kaplan *et al.* [12] later reported that TAT-mediated delivery of cargo into cells occurred via macropinocytosis. Ruan *et al.* [8] reported that TAT-conjugated QDs were bound to

the inner surface vesicles and trapped in intracellular organelles and therefore could not enter the cell nucleus to any substantial degree.

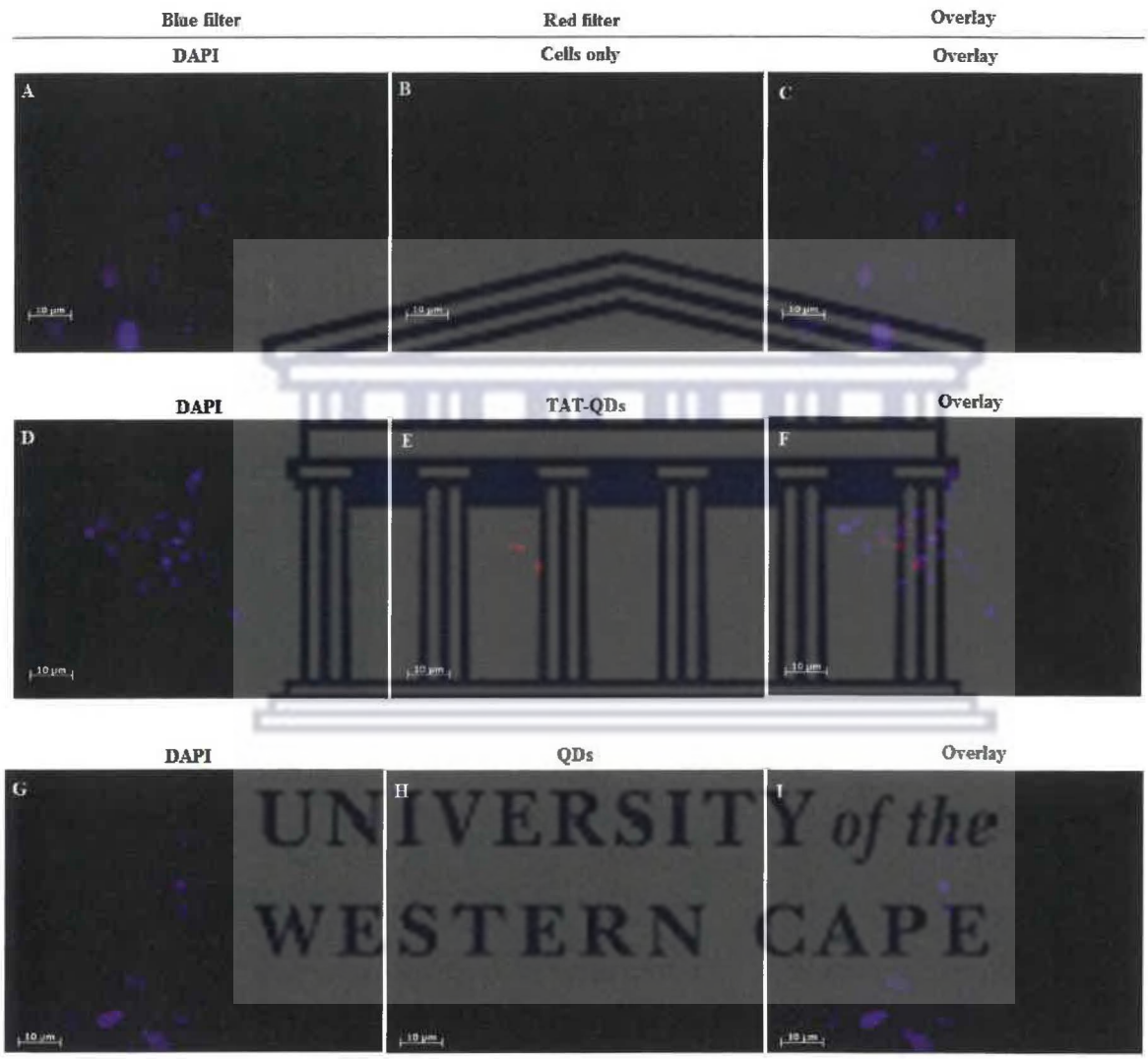

Figure 5.3 Fluorescence microscopy images of InP/ZnSe QD-treated and untreated Caco-2 cells. Images A–C represent untreated cells used as negative controls. Images D–E and G–I represent cells treated with TAT-conjugated and unconjugated InP/ZnSe QDs

5.3 Conclusions

Cytotoxicity studies of MPA-capped InP/ZnSe and CdTe/ZnS QDs were successfully carried out using the MTT assay. It was demonstrated that InP/ZnSe were less toxic compared to CdTe/ZnS QDs.

The cellular internalization study showed that the TAT-conjugated InP/ZnSe QDs were internalized by Caco-2 cells. The result proved that the as-prepared InP/ZnSe still retained their fluorescence properties even in the biological milieu.

5.4 References

1 Kuo T-R, Lee C-F, Lin S-J, Dong C-Y, Chen C-C, Tan H-Y, *Chem. Res. Toxicol.*, **2011**, *24, 253*

2 Male KB, Lachance B, Hrapovic S, Sunahara G, Luong JHT, *Anal. Chem.*, **2008**, *80, 5487*

3 Monteiro-Riviere NA, Inman AO, Zhang LW, *Toxicol. Appl. Pharm.*, **2009**, *234, 222*

4 Gu Y-P, Cui R, Zhang Z-L, Xie Z-X, Pang D-W, *J. Am. Chem. Soc.*, **2012**, *134, 79*

5 Erogbogbo F, Yong K-T, Roy I, Hu R, Law W-C, Zhao W, Ding H, Wu F, Kumar R, Swihart MT, Prasad PN, *ACS Nano*, **2011**, *5, 413*

6 Frankel AD, Carl O. Pabo CO, *Cells*, **1988**, *55, 1189*

7 Brasseur R, Divita G, *Biochim. Biophys. Acta*, **2010**, *1798, 2177*

8 Ruan G, Agrawal A, Marcus AI, Nie S, *J. Am. Chem. Soc.*, **2007**, *129, 14759*

9 Yong K-T, Ding H, Roy I, Law W-C, Bergey EJ, Maitra A, Prasad PN, *ACS Nano*, **2009**, *3, 502*

10 Bharali DJ, Lucey DW, Jayakumar H, Pudavar HE, Prasad PN, *J. Am. Chem. Soc.* **2005**, *127, 11364*

11 Gupta B, Levchenko TS, Torchilin VP, *Adv. Drug Delivery Rev.*, **2005**, *57, 637*

12 Kaplan IM, Wadia J, Dowdy SF, *J. Control. Release*, **2005**, *102, 247*

CHAPTER 6: GENERAL CONCLUSIONS AND FUTURE WORK

6.1 General conclusions

The InP/ZnSe QDs were successfully synthesized using the one-pot hot injection method. Literature abounds with group III-V QDs of the type InP/ZnS. The reason for our choice of ZnSe for the shell layer was based on the lower lattice mismatch between InP and ZnSe of 3.5 % in comparison to 7.6 % between the InP and ZnS. Such a lower lattice mismatch would allow for better epitaxial growth of the shell over the InP core thus reducing surface traps responsible for reduced quantum efficiencies. To this end, a 1.4 times reduction in surface related emission was demonstrated (**Section 3.2.1.1**).

Polyethylene glycol was for the first time successfully used as a non-coordinating solvent in the synthesis of InP/ZnSe QDs. Highly luminescent QDs were obtained with a maximum emission wavelength of 605 nm. However, a very large FWHM (114 nm) was obtained indicating a very large size distribution (**Section 3.2.2.1**). Lattice fringes of the as-prepared QDs were continuous indicating that the ZnSe shell was grown epitaxially.

When secondary injection of precursors was applied in the fabrication of the InP/ZnSe QDs, a red shift in the maximum emission wavelength was observed (**Section 3.2.3**). However, an increase in the initial concentration of zinc carboxylate caused a blue shift and this was attributed

to the slowing down of the crystal growth rate by zinc carboxylate. As discussed in **Section 3.2.3.1**, this effect of zinc carboxylate has been reported in the fabrication of InP/ZnS.

Starting with high moles of precursors (**Section 3.2.4**) resulted in a very significant improvement of the emission profiles of the QDs. Maximum emission wavelengths greater than 630 nm were obtained. The effect of reaction time on the PL was also investigated under the same conditions of high moles of precursors. The results showed that the improved emission profiles were attributable to the higher initial concentrations of the precursors and not the longer growth times. As discussed in **Section 3.2.4.1**, the phosphorus precursor is depleted at the InP nucleation step and any further extension of the reaction time does not lead to further spectral evolution. The PL FWHM values obtained were around 120 nm, again showing the large size distribution of the as-prepared QDs. The average size of the InP/ZnSe QDs was about 4.65 ± 0.40 nm.

Furthermore, Ag-, Co- and Fe-doped InP/ZnSe QDs were successfully synthesized for the first time using the growth-doping method. For Ag-InP/ZnSe QDs, the obtained maximum emission peaks were 592, 598 and 613 nm for Ag-dopant levels of 0, 5 and 10 % respectively. Positively, a red shift was observed and attributed to Ag dopant ions being substitutional impurities. Increase in cobalt dopant ions from 15 to 20 % with respect to phosphorus did not change the emission peak position of 585 nm. As for iron-doped InP/ZnSe QDs, a large blue shift (from 592 to 566 nm) was observed with increase in dopant ions from 1 to 5 % with respect to phosphorus. The blue shift is attributed to decrease in reaction rate with iron dopant incorporation. In all the three types of doped-InP/ZnSe QDs, a quenching effect was observed with increasing dopant levels and this was attributed to a decrease in electron-hole recombination with increasing dopant

levels. Structural characterization of the doped-InP/ZnSe QDs was carried out using HRTEM and XRD techniques. The HRTEM micrographs showed that the as-prepared doped-InP/ZnSe QDs were crystalline. XRD data showed that the systems retained their crystallinity after the doping process.

The surface chemistry of both the doped and undoped InP/ZnSe QDs was successfully modified using MPA ligand. As cytotoxicity is of great concern in biological applications of QDs, *in vitro* cytotoxicity study using MTT assay showed that less than 50 % of Caco-2 cell death occurred at MPA-capped InP/ZnSe QD concentration of 125 µg/mL, while more than 80 % of cell death occurred for a lower MPA-capped CdTe/ZnS QD concentration of 62.5 µg/mL. The result showed that indium phosphide-based QDs were less toxic than CdTe/ZnS QDs. The terminal carboxylic acid groups of the MPA-capped InP/ZnSe QDs were subsequently used to effectively couple the QDs to TAT for cellular internalization studies. Fluorescence imaging of QD-treated Caco-2 cells proved that the as-prepared InP/ZnSe QDs retained their optical properties in the biological environment, widening the chances of their use both *in vitro* and *in vivo* diagnostic and therapeutic studies.

6.2 Future work

As the InP/ZnSe QDs are a promising replacement of cadmium-based QDs that have very narrow PL FWHM, future work in the fabrication of indium-based QDs should be focused on controlling the size distribution of the QDs. This has a great bearing on biological studies as

nanoparticle size has been reported as one of several nanomaterial environmental factors that affect toxicity (**Section 1.10**).

InP/ZnSe QDs were synthesized using the one-pot hot injection method. One major limitation of this procedure is that after the nucleation step, when all phosphorus precursors are depleted, extended reaction times do not lead to significant emission spectral evolution. Procedures allowing for continuous supply of the phosphorus [1] should be extended to InP-based QD synthesis. Coupled with the use of the ZnSe shell, this would yield core/shell InP/ZnSe QDs with longer emission wavelengths better epitaxial growth of the shell.

In this study, monodentate MPA ligand was used for surface modification of the QDs. The use of bidentate ligands when making the hydrophobic as-prepared QDs water compatible should also be investigated with indium-based QDs. These bidentate ligands offer greater stability due to the chelating effect and have been successfully used on cadmium-based QDs (**Section 1.8.1.1**).such ligands include DHLA ligand and its polyethylene glycol (PEG) modified derivatives. PEGylation of the QDs has been reported to enhance their circulation time as well as reduced non-specific deposition *in vivo* [2]. This is critical if the InP-based QDs are to be applied in animal studies.

With regards to transition metal-doped QDs, future work on these systems should be extended to characterization using techniques such as STEM-EELS or STEM-EDS modes that would reveal core/shell structure. Ligand-field electronic absorption spectroscopy would also be an important tool to use to probe dopant ions in the doped systems [3].

The applications of the InP/ZnSe QDs are currently being extended to molecular beacon designs in our Biolabels Unit. The molecular beacons (MBs) are stem-loop hairpin shaped oligonucleotide probes that are decorated with a fluorescent and quenching moiety on the opposite ends of the probe [4]. The loop portion of the MB is an anti-sense targeting domain that hybridizes to the target sequence from specific biomarkers [5]. The InP/ZnSe QDs are being employed as the fluorescent moieties while gold nanoparticles are incorporated in the design as the quenching moieties. The overall direction of this project is to be able to carry out multiplexed detection of breast cancer biomarkers in patient tissues.

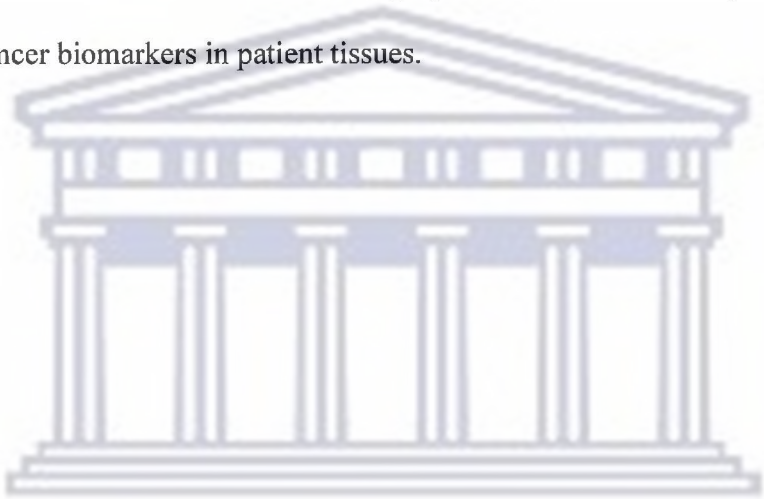

6.3 References

1 Li L, Protière M, Reiss P, *Chem. Mater.*, **2008,** *20, 2621*

2 Ballou B, Lagerholm BC, Ernst LA, Bruchez MP, Waggoner AS, *Bioconjugate Chem.*, **2004**, *15, 79*

3 Radovanovic PV, Norberg NS, McNally KE, Gamelin DR, *J. Am. Chem. Soc.*, **2002**, *124, 15192*

4 Kim Y, Sohn D, Tan W, *Int. J. Clin. Exp. Pathol.*, **2008**, *1, 105*

5 Tyagi S, Kramer FR, *Nature Biotechnol.*, **1996**, *14, 303*